

# Crystallization and Degradation Studies in Organic & Perovskite Solar Materials

DISSERTATION

zur Erlangung des Grades

“Doktor der Naturwissenschaften”

am Fachbereich Chemie, Pharmazie und Geowissenschaften  
der Johannes Gutenberg-Universität in Mainz



MAX-PLANCK-GESELLSCHAFT

vorgelegt von

Dan Li

geboren in Henan province, China

Mainz, 2016



---

Die vorliegende Arbeit wurde in der Zeit von Oktober 2012 bis Februar 2016 unter der Betreuung von [REDACTED] und [REDACTED] am Max-Planck-Institut für Polymerforschung in Mainz durchgeführt.

Tag der Mündlichen Prüfung: 23.06. 2016

Dekan: [REDACTED]

1. Berichterstatter: [REDACTED]
2. Berichterstatter: [REDACTED]





---

*Dedicated to my family*



---

# Zusammenfassung

Organische Solarzellen gelten als vielversprechende Alternativen zu den herkömmlichen Silizium-Solarzellen, hauptsächlich da sie durch lösungsbasierte Dünnschichttechnologie hergestellt werden. Diese Technologie ermöglicht eine kostengünstige und großflächige Produktion von flexiblen organischen Solarzellen durch das Rolle-zu-Rolle-Verfahren. In umfangreichen wissenschaftlichen Studien werden neue organische Materialien zur Lichtabsorption synthetisiert und neue Herstellungsverfahren untersucht, die die Leistung der Solarzellen weiter verbessern. Um die organischen Solarzellen effizient zu nutzen, ist wichtig, die Stabilität und Abbaumechanismus der organischen Materialien zu verstehen.

Der erste Teil der Arbeit konzentriert sich auf den photooxidativen Abbau von [6,6]-Phenyl-C<sub>61</sub>-Buttersäuremethylester (PCBM). PCBM wird in vielen bulk heterojunction Solarzellen als Elektronenakzeptor genutzt. Darüber hinaus ist PCBM ideal um in Perowskit- Photovoltaik hysteretische Effekte an den Grenzflächen zu minimieren. Die kurze Lebensdauer und geringe Stabilität von PCBM haltigen Solarzellen stellt jedoch ein Hindernis für deren Vermarktung dar. Die Messungen in meiner Arbeit zeigen, dass die Photooxidation in Gegenwart von Sauerstoff eine wichtige Rolle beim Abbau von PCBM spielt, der zu einem Ausfall der Geräte führen.

Seit 2009 zählen auch Perowskit Solarzellen zu den vielversprechenden lösungsbasierten Technologien. Vor kurzem überschritten Methylammoniumbleihalogenid (CH<sub>3</sub>NH<sub>3</sub>PbX<sub>3</sub>) basierte Perowskit Solarzellen eine Leistungsumwandlungseffizienz von 20%. Zur gleichen Zeit, ziehen Kristallisation und Stabilitätsprobleme immer mehr Aufmerksamkeit auf sich. Insbesondere Wassermoleküle (hohe feuchte Umgebung) spielen in der Zersetzung von Perowskit-Filme eine wichtige Rolle. Der Abbaumechanismus von CH<sub>3</sub>NH<sub>3</sub>PbX<sub>3</sub> in einer Umgebung mit hoher Feuchtigkeit wird weiterhin untersucht.

Der zweite Teil der Arbeit befasst sich mit den Kristallisations- und Abbauprozessen von CH<sub>3</sub>NH<sub>3</sub>PbI<sub>3</sub> Filmen. Hier beobachtete ich das Filmwachstum und den Kristallisationsprozess von Perowskit unter Einsatzumgebung mit in-situ Rasterkraftmikroskopie. Darüber hinaus untersuchte ich die Morphologie-Entwicklung von Perowskit-Filmen in feuchter Umgebung durch in-situ Rasterkraftmikroskopie und in-situ-Röntgendiffraktometrie, um den lokalen Morphologie-, sowie den Kristallstruktur-Änderungen im Detail folgen zu können. Basierend auf diesen Messungen konnte ich feststellen, dass die durch Feuchtigkeit induzierten Morphologie-Änderungen nicht umkehrbar sind, da die in Feuchtigkeit entstandenen

---

Korngrenzen in trockener Atmosphäre nicht verschwanden. Die zusätzlichen Korngrenzen könnten der Grund für die Verstärkung der JV-Hysterese sein, die Leguy et al in ihrer Studie festgestellt hatten (*Chem. Mater.* **2015**, 27, 3397-3407). Diese Interpretation ist konsistent mit dem Befund, daß eine Abnahme der Kristallgröße zu einer zunehmende Hysterese führt. Zusätzlich könnte ich durch meine Ergebnisse das Abbau-Modell von Leguy und Mitarbeitern verfeinern (*Chem. Mater.* **2015**, 27, 3397-3407).

Alle oben genannten Studien geben uns ein besseres Verständnis für die Abbauprozesse von organischen und Perowskit-Materialien in schädlichen Umgebungen. Eine zusätzliche Einkapselung oder Passivierungsschicht auf organischer und Perowskit- Materialien ist daher nötig, um die aktiven Schichten vor einer schädlichen Atmosphäre zu schützen, was für die Gerätestabilität und elektrischen Parameter sehr vorteilhaft ist.

---

## Abstract

Organic solar cells are considered as promising alternatives to replace traditional silicon solar cells, which is mainly due to the possibility of solution-processed thin-film technology. This technology allows low-cost but large-scale production of flexible organic solar cells using roll-to-roll processes. Extensive academic research has been carried out to synthesize more new light-absorption organic materials and new preparation procedures to improve device performance. In order to fully utilize the organic solar cells, it is very important to understand the stability and degradation mechanism of the organic materials.

The first part of the thesis focuses on the photo-oxidative degradation of [6, 6]-phenyl-C<sub>61</sub>-butyric acid methyl ester (PCBM) material. As electron acceptor material, PCBM has been widely utilized in bulk-heterojunction photovoltaics. Additionally, PCBM also can be an ideal material in perovskite photovoltaics to minimize hysteretic effects at interfaces. However, the short lifetime and poor stability of PCBM-containing photovoltaic devices may present an obstacle for their commercialization. In my thesis, the measurements show that photo-oxidation in the presence of oxygen plays a significant role in degradation of PCBM which will lead to a failure of devices.

Additionally, perovskite solar cells are booming up since 2009 as promising technology which allows solution processing. The recently reported record power conversion efficiency in methylammonium lead halide (CH<sub>3</sub>NH<sub>3</sub>PbX<sub>3</sub>) based perovskite solar cells has exceeded 20%. At the same time, the crystallization and stability issues are attracting more and more attentions. In particular, the water molecules (high humid environment) play a role in the degradation of perovskite films. However, the degradation mechanism under high humid environment is currently still under investigation.

The second part of the thesis deals with the crystallization and degradation processes of CH<sub>3</sub>NH<sub>3</sub>PbI<sub>3</sub> films. Here, I studied the film growth and crystallization process of perovskite under inert environment using in-situ scanning force microscopy. Furthermore, I investigated the morphology evolutions of perovskite films upon humid environments by in-situ scanning force microscopy and in-situ X-ray diffraction pattern, which allow locally tracing the morphology and crystal structure changes in detail. Based on the measurements, I could conclude that the humidity-induced morphology was not reversible and humidity-induced grain boundaries did not disappear at dry atmosphere. The presence of these grain boundaries is most likely the reason for an increase in JV hysteresis that was measured by Leguy et al. This interpretation is

---

consistent with the finding that a decrease in crystal size leads to an increasing hysteresis. In the end, I was able to refine the degradation model posted recently by Leguy and co-workers (*Chem. Mater.* **2015**, 27, 3397-3407).

All the above studies give us a better understanding of the degradation processes of organic/perovskite materials under detrimental environments. Therefore, a sufficient encapsulation or passivation layer on top of organic/perovskite materials is able to keep the active layers away from detrimental atmospheres, which can be very beneficial for device stability and electrical parameters.

---

# Contents

<b>Chapter 1 Introduction .....</b>	<b>1</b>
1.1 Device architecture and working mechanism.....	2
1.2 Degradation of organic solar cells.....	5
1.3 Perovskite solar cells.....	11
1.3.1 Crystallization issue in perovskite films.....	15
1.3.2 Stability issue in perovskite films .....	17
1.4 Motivation.....	19
<b>Chapter 2 Experimental methods.....</b>	<b>21</b>
2.1 Scanning Probe Microscopy.....	21
2.1.1 Working principle .....	21
2.1.2 Imaging modes .....	22
2.1.3 EnviroScope Scanning Force Microscopy .....	24
2.2 UV-vis absorption spectroscopy.....	26
2.3 X-ray diffraction.....	28
2.4 Matrix-assisted laser desorption/ionization time-of-flight mass spectrometry (MALDI-TOF MS).....	33
2.5 X-ray photoelectron spectroscopy (XPS).....	36
2.6 Experimental setup.....	39
2.6.1 Substrates preparation.....	39
2.6.2 Spin coating technique .....	39
2.6.3 SFM cantilever cleaning.....	39
2.6.4 In-situ SFM measurements.....	39
2.6.5 UV-vis absorption spectroscopy .....	40

---

2.6.6	In-situ SFM measurements under humidity.....	40
2.6.7	X-ray diffraction measurements.....	41
2.6.8	X-ray photoelectron spectroscopy (XPS).....	42
2.6.9	MALDI-TOF MS measurements .....	42
<b>Chapter 3 Thermal crystallization and decomposition of CH<sub>3</sub>NH<sub>3</sub>PbI<sub>3</sub> films .....</b>		<b>45</b>
3.1	Introduction .....	45
3.2	Experimental section .....	46
3.3	Results and discussion.....	47
3.3.1	Under N <sub>2</sub> atmosphere.....	47
3.3.2	Thermal annealing vs solvent vapor annealing.....	55
3.4	Summary and conclusion .....	59
<b>Chapter 4 Humidity-induced degradation of CH<sub>3</sub>NH<sub>3</sub>PbI<sub>3</sub> perovskite films .....</b>		<b>61</b>
4.1	Introduction .....	61
4.2	Experimental section .....	62
4.3	Results and discussion.....	62
4.3.1	CH <sub>3</sub> NH <sub>3</sub> PbI <sub>3</sub> films at low humidity (0%, 20% and 50%) .....	62
4.3.2	CH <sub>3</sub> NH <sub>3</sub> PbI <sub>3</sub> film at 80% humidity.....	66
4.4	Summary and conclusion .....	76
<b>Chapter 5 Photo-oxidation of PCBM films .....</b>		<b>77</b>
5.1	Introduction .....	77
5.2	Experimental section .....	80
5.2.1	Film preparation .....	80
5.2.2	Degradation procedures of PCBM films .....	80
5.3	Results and discussion .....	81
5.3.1	Positive-ion mode MALDI-TOF MS .....	83



---

5.3.2	Negative-ion mode MALDI-TOF MS .....	84
5.4	Summary and conclusion .....	87
<b>Chapter 6 Concluding remarks and Outlook .....</b>		<b>91</b>
<b>Bibliography.....</b>		<b>93</b>
<b>Acknowledgement .....</b>		<b>109</b>
<b>Curriculum Vitae .....</b>		<b>111</b>



# Chapter 1

## Introduction

The global demand for energy resources is increasing as consequence of the fast development of global economy. Up to now, the traditional energy supplies (e.g. fossil fuels) are still playing important roles in electric energy generation but they are non-renewable. In addition, the depletion of traditional energy supplies (e.g. fossil fuels) releases greenhouse gas carbon dioxide (CO<sub>2</sub>) and toxic gases such as nitrogen dioxide (NO<sub>2</sub>) and sulphur dioxide (SO<sub>2</sub>), which cause serious environmental problems like global warming and air pollution. Therefore, renewable and environmentally friendly energy sources have attracted significant attention. Among various kinds of renewable energy sources, such as geothermal, solar energy, hydropower, wind power and wave power, solar energy is the largest energy resource on the earth. In the 2012 World Energy Assessment, the United Nations Development Programme (UNDP) found that the annual potential of solar energy was 1575-49387 exajoule (EJ). The global energy consumption in 2012 was 559.8 EJ, which means that solar energy has a great potential to meet the energy demands from the whole world [1, 2].

The solar technology for harvesting the sun energy is based on the photovoltaic effect which was first discovered by a French physicist Alexandre-Edmond Becquerel in 1839 [3, 4]. The photovoltaic effect is a physical and chemical phenomenon which creates voltage or electric current in a material when exposed to sun light. The first solar panel was created by a New Yorker inventor Charles Fritts that was based on a thin layer of gold onto selenium wafer obtaining a power conversion efficiency  $\eta$  of 1% [5]. The power conversion efficiency  $\eta$  of a solar cell is defined as the ratio of energy output to energy input from the sun,  $\eta = P_{\text{out}}/P_{\text{in}}$  (P: power). The first practical silicon

photovoltaic cell was developed by Daryl Chapin, Calvin Fuller and Gerald Pearson at Bell Labs in 1954 [6]. The power conversion efficiency of this silicon solar cell reached 6% by converting sunlight energy into electricity. But these silicon solar cells were produced by hand and their price was around \$ 1000 per watt. They were mostly applied in power satellites and the cost was too high for household applications. The development of photovoltaic cells was continued with the aim for consumer applications with lower price and higher power conversion efficiency. The primary task to reduce the price of photovoltaic cells is to replace the expensive materials with

cheap ones in the production process while still keep the same power conversion efficiency. In 1977, electrically conducting organic polymers were synthesized by Hideki Shirakawa, Edwin J. Louis, Alan G. Macdiarmid, Chwan K. Chiang and Alan J. Heeger [7]. These conducting polymers have the potential advantages of low cost compared to silicon materials, and they also can be processed using thin film technology. The development of organic solar cells is attracting great attentions due to their promising properties for flexible, light-weight and roll-to-roll fabrication [8, 9]. The photovoltaic cells made from polymer-fullerene systems currently dominate in the current research field of organic solar cell, and the device performance has exceeded 10% [10-12]. However, the fundamental disadvantage of organic solar cells is their degradation when exposed to ambient environments (i.e. oxygen, irradiation, moisture) compared to inorganic solar cells [13-21]. The degradation of organic solar cells leads to practical problems in outdoor applications. The degradation mechanisms in organic solar cells have been investigated under different detrimental environments by using a combination of different characterization technologies [22, 23].

## 1.1 Device architecture and working mechanism

Usually, the device structure of an organic solar cell consists of the active layer sandwiched between two electrodes (anode and cathode). Sometimes the electron/hole transporting layers are also applied between active layer and electrode to ensure selective charge transport. The device architecture of organic solar cell is shown in Figure 1.1. In organic solar cells, the absorption of photons by organic material (also called active layer) creates excitons which are electron-hole bounded pairs, while free charge carriers are generated in inorganic solar cells. The excitons have very short lifetime and the diffusion length in the active layer before recombination is only in the order of about 10 nm [24]. Therefore, the photo-generated excitons have to be separated into free charge carriers before recombination occurs.

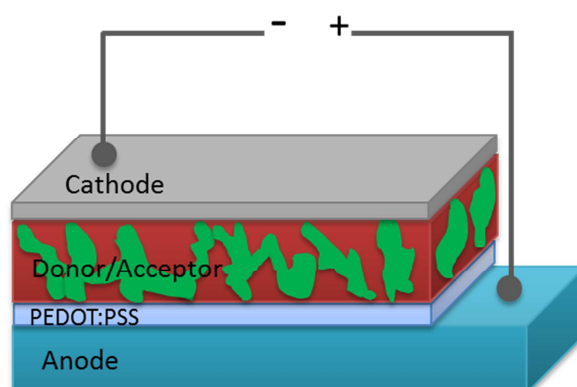


**Figure 1.1:** Schematic of an organic solar cell with bulk-heterojunction structure, which includes different layers, anode, hole transporting layer (i.e. poly(3,4-ethylenedioxy thiophene) polystyrene sulfonate, PEDOT:PSS), donor/acceptor formed active layer and cathode.

The structure of active layer in organic solar cells underwent three architectures. The simplest organic photovoltaic cell was based on single layer structure which was made by David Kearns and Melvin Calvin in 1958 [25]. The photo-generated excitons are separated into free charge carriers at the interface between active layer and the electrode. However, the separation efficiency of excitons into free charges is very low in single layer-structured solar cells. To overcome this problem, C. W. Tang introduced a bi-layer structured solar cell in 1986, where the electron donor and acceptor materials were put together by forming a double layer heterojunction [26]. Here, the excitons first diffuse to the donor-acceptor interface and are then be separated into free charge carriers. Only the excitons which have a distance of within diffusion length from donor-acceptor interface can be separated into free charge carriers. The rest of excitons recombine and are lost. Therefore, the power conversion efficiency of bi-layer solar cell was only about 1% under AM 2.0 solar simulated illuminations [26]. The breakthrough came in 1995 when Yu et al. fabricated a solar cell with interpenetrating phase separated donor-acceptor network, where the donor and acceptor materials were mixed by forming a nanoscale bulk heterojunction [27]. This donor-acceptor mixed bulk heterojunction achieves large donor-acceptor interfaces throughout the whole active layer, which efficiently separate more excitons into free charge carriers. Currently, most of the organic solar cells are fabricated based on bulk-heterojunction structure (Figure 1.1). The conversion mechanism from sunlight to electric power in an organic solar cell contains four basic steps (Figure 1.2).

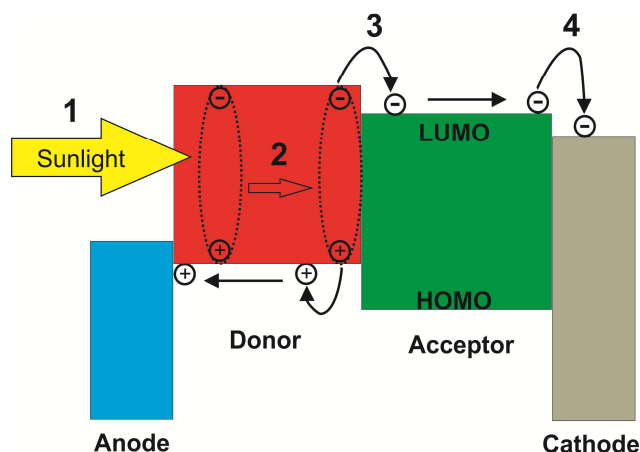


**Figure 1.2:** Schematic of sunlight energy-electricity conversion mechanism in the bulk-heterojunction organic solar cell.

Step 1: The bulk-heterojunction structured solar cell consists of a nanoscale blend of donor and acceptor materials, which is called as active layer. The sunlight is absorbed by the active layer. The absorption efficiency of an active layer is dependent on the film thickness, the lowest unoccupied molecular orbital (LUMO) and the highest occupied molecular orbital (HOMO) levels of donor material. Excitons are generated afterwards which contains an electron promoted to the LUMO level and a positive charge carrier “hole” in HOMO level. The electron-hole pair is still bounded by the electrostatic Coulomb force.

Step 2: Since the diffusion length of an exciton is only in the order of about 10 nm, it has to diffuse to the donor/acceptor interface before it recombines either non-radiative with a surface-trap site or becomes temporarily trapped [24, 28, 29].

Step 3: The energy difference between two LUMO levels of donor and acceptor materials is always higher than the binding energy of an exciton (0.3 – 1.0 electron volts, eV). So the excitons are dissociated into free charge carriers (electrons and holes) at the interfaces of donor and acceptor materials.

Step 4: Finally, the electrons and holes are being transported towards the corresponding electrodes via the donor-acceptor interpenetrating network. Once the electrons and holes reach electrodes, they will be collected and connected with external circuit to supply electricity.

Each of the above steps is quite important to realize high power conversion efficiency of an organic solar cell. In step 1, an important parameter for the sunlight absorption is the optical bandgap ( $E_g$ ) of light-absorbing material. The optical bandgap is defined as the difference between HOMO and LUMO levels. When the photo energy is equal to or larger than the bandgap of light-absorbing material, the photo will be absorbed and

electron and hole are generated. The relationship between optical bandgap  $E_g$  and the absorbed photo wavelength  $\lambda$  is defined as equation of  $E_g = h\frac{c}{\lambda}$ . Here,  $h$  is the Planck constant and  $c$  is the light speed in vacuum. Therefore, the material with lower bandgap has larger absorption wavelength, which indicates wider sunlight absorption spectrum. For example, the absorbing material with an optical bandgap of around 1.1 eV is able to harvest up to 77% of the photo flux reaching the earth. However, most of absorbing materials have optical bandgaps of around 2.0 eV, so they only can absorb 30% of the photo flux reaching the earth. Therefore, lots of researches have been carried out to optimize the optical bandgap by altering LUMO and HOMO levels of absorbing materials [30-32].

In addition, the microstructure of the active layer is also critical for the exciton diffusion, free charge transport in step 2-4 in Figure 1.2, which plays a vital role in determining high power conversion efficiency. The microstructure of the active layer can be modified by processing conditions such as choice of solvent, thermal or vapor annealing. For example, Shaheen et al. prepared the active layer containing poly[2-methyl,5-(3',7'-dimethyloctyloxy)-1,4-phenylenevinylene] (MDMO-PPV) and [6,6]-phenyl-C<sub>61</sub> butyric acid methyl ester (PCBM) blends using either organic solvent toluene or chlorobenzene. The results showed that the blend films cast from chlorobenzene had smoother surface than those cast from toluene [33]. The device based on chlorobenzene-cast films had a power conversion efficiency of 2.5% under AM 1.5 relative to the 0.9% efficiency of the toluene-cast device. The results indicated that the casting solvent had an effect on the organization of MDMO-PPV polymer chains. The blend films cast from chlorobenzene increased the interactions between polymer chains which led to better hole conduction [33].

## 1.2 Degradation of organic solar cells

In the polymer-based photovoltaic devices, [6,6]-phenyl-C<sub>61</sub>-butyric acid methyl ester (PCBM) is one of the best performing and most commonly used fullerene derivative [12, 13, 34, 35]. PCBM is an electron acceptor material and is usually used together with electron donor materials such as poly(3-hexylthiophene-2,5-diyl) (P3HT). The chemical structures of P3HT and PCBM are shown in Figure 1.3. The power conversion efficiency of polymer-fullerene based solar cell has exceeded 10% not only for tandem cells [12] but also for single junction cells [10, 11]. However, PCBM-based polymer solar cells were reported exhibiting short lifetime and instability compared with inorganic solar cells when exposed to ambient atmosphere or long-term illumination

[13, 14, 36, 37]. This drawback causes serious problems for practical applications for PCBM-based photovoltaic cells.

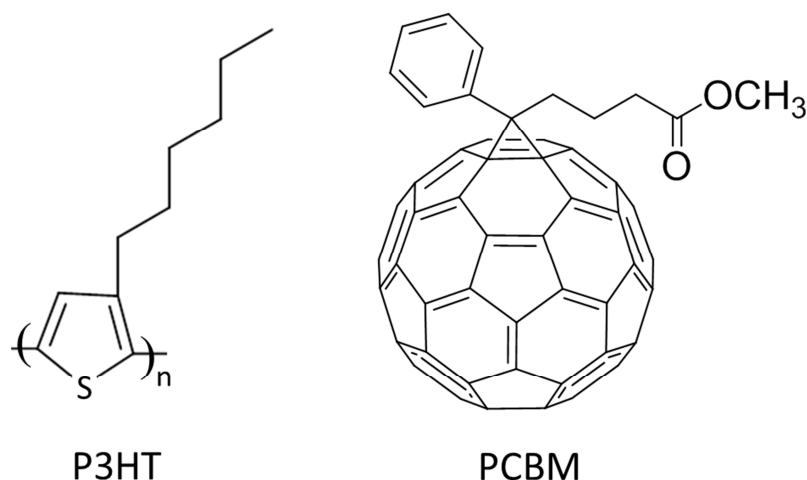


**Figure 1.3:** Chemical structures of electron donor (P3HT) and acceptor (PCBM) materials, respectively.

Previous studies showed that various degradation processes occurred inside a polymer-fullerene organic solar cell, roughly divided into physical degradation and chemical degradation (Figure 1.4) [36]. Here, **physical degradation** mainly refers to the morphology stability of the active layer and the interface degradation between electrode and active layer. In the paper by Schaffer et al. [38], the authors performed in-situ micro grazing incidence small angle X-ray scattering (in-situ  $\mu$ GISAXS) and current-voltage tracking measurements on P3HT:PCBM based solar cell to measure the morphological changes and electric characteristics under illumination, respectively. The morphological degradation was observed, where the active layer domains drifted apart from each other with smaller domains vanishing whereas larger ones growing. This drift caused a reduction of the overall area of the active layer in the corresponding solar cell, which converted less light into electric power. Consequently, the output current of the whole solar cells decreased accordingly [38]. It was concluded that the morphological degradation of active layer was an important pathway which caused efficiency degradation in polymer solar cells. Therefore, the morphology quality of active layer should be well controlled and fully considered during the design and fabrication process of polymer solar cells.



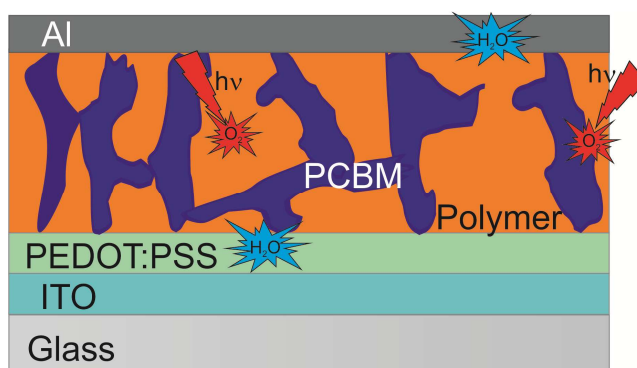


**Figure 1.4:** Cross section view of the bulk-heterojunction organic solar cell with a configuration of glass-ITO/PEDOT:PSS/polymer-PCBM/Al. Many degradation pathways take place inside a solar cell resulting in a decrease in power conversion efficiency. (Adapted from reference [36]).

The **chemical degradation** of organic solar cells describes the interactions between active layer and external environmental factors, such as oxygen, water and irradiation. The reactions between molecular oxygen/water and active layer are an important source of degradation. As indicated in Figure 1.4, there are various diffusion pathways of oxygen and water into the active layer, hole-transporting layer (PEDOT:PSS) which may cause solar cells degradation. Furthermore, the interaction between oxygen and the active layer can be activated and accelerated by the presence of light illumination.

### Water induced degradation

Poly(3,4-ethylenedioxythiophene) polystyrene sulfonate (PEDOT:PSS) is a conductive polymer which is always used as hole transport layer in the organic solar cells. Kawano et al. [39] investigated the degradation pathways of organic solar cells and concluded that the hole transporting layer PEDOT:PSS was the degradation source under air exposure. In their experiments, the photovoltaic performance characteristics, short circuit current density  $J_{sc}$ , open circuit voltage  $V_{oc}$ , fill factor FF and power conversion efficiency, were measured as a function of exposure time at different ambient conditions (in the dark and under white light irradiation, under air, dry oxygen and humid nitrogen atmospheres). It was found that the degradation under air exposure was light independent, which was due to the water absorption by the PEDOT:PSS layer [39]. In addition, the hole mobility of the solar cell did not change under air exposure. It was concluded that the absorption of water in PEDOT:PSS layer caused the formation of some insulating domains at the PEDOT:PSS and active layer interface, leading to an increase in the injection barrier but without affect the intrinsic charge carrier (i.e. hole mobility). The increased injection barrier hindered efficient charge

collection at electrodes which induced a loss of short circuit current density  $J_{sc}$  and device power conversion efficiency. This study recommended the importance of developing an alternative hole transporting layer which should be water (humidity) insensitive.

Norrman et al. [40] studied the water-induced degradation of polymer solar cells based on the configuration of aluminum (Al)/polymer:PCBM/PEDOT:PSS/indium tin oxide (ITO) (polymer=P3HT or MEH-PPV, poly[2-methoxy-5-(2'-ethylhexyloxy)-1,4-phenylenevinylene]). The results showed that water molecules diffused rapidly through the Al cathode into the whole device structure leading to homogeneous degradation in all interfacial layers [40]. The short circuit current density  $J_{sc}$  was recorded as a function of exposure time at different humidity atmospheres (25% and 90%) under illumination (Figure 1.5). The results showed that devices exposed to 90% humidity and 42 °C exhibited a faster decay in short circuit current density  $J_{sc}$  compared to the solar cells stored in 25% humidity and 72 °C. Additionally, this report further suggested that the presence of oxygen and illumination under simulated sunlight accelerated the degradation process induced by water [40].

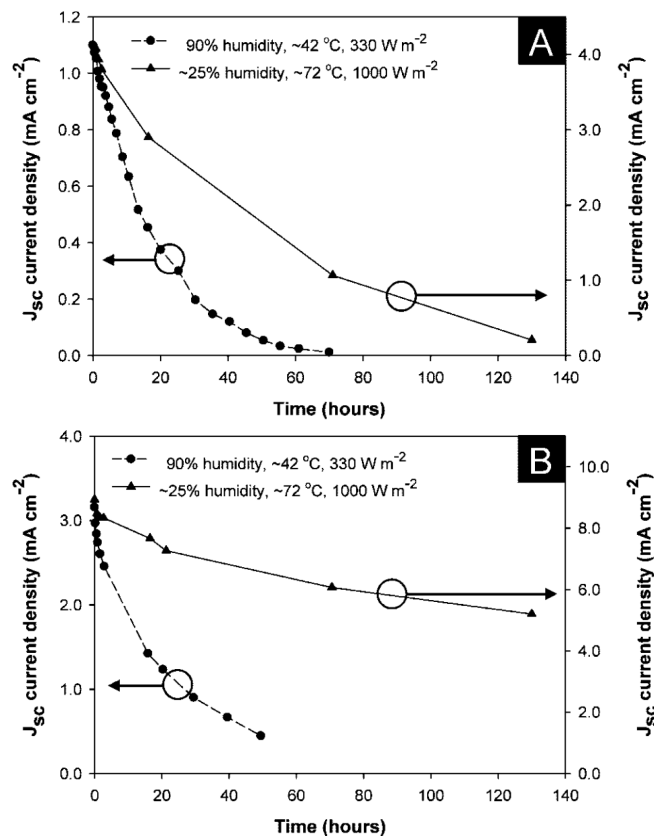


**Figure 1.5:** The short circuit current density  $J_{sc}$  as a function of exposure time at different humidity environments, 25% and 90% [40].

## Photo-degradation of active layer

In organic solar cells, the active layer usually consists of a polymer and fullerene blend which absorbs sunlight. Here, the conducting materials are polythiophenes which act as electron donor in the active layer. Among them, poly(3-hexylthiophene) (P3HT) is the most studied polymer electron donor material for organic solar cells. However, P3HT is susceptible to photo-degradation resulting in a short lifetime of the whole devices. The oxygen plays a vital role in degrading the active layer which reduces the power conversion efficiency of the whole solar cell. Remarkably, most photo-degradation processes take place with the presence of oxygen, which can be called as photo-oxidation. In 2010, Hintz et al. proposed a two-step photo-oxidation mechanism of P3HT thin layer by using in-situ UV-vis absorption spectroscopy and X-ray photoelectron spectroscopy [41]. First, P3HT was attacked at the alkyl chains resulting in the formation of reactive peroxide species. Second, these peroxide species subsequently caused the oxidation of sulfur and concomitantly the destruction of thiophene ring, leading to a loss of UV-vis absorption. The rate of photo-oxidation under AM 1.5 conditions was at least one order of magnitude faster than the degradation of P3HT by ozone [41]. The destruction of polymer molecules could ultimately result in the evaporation of the materials, which caused a decrease in film thickness [42]. As a result of this photo-oxidation, fragmentation of the polymers took place which ultimately resulted in the evaporation of the material [42]. This would result in a decrease of film thickness. In addition, the photo-oxidation of P3HT material induced fragments and oxides which generated by partial molecular scission, which increased the resistance of organic film and decreased device performance [43].

Another important class of materials in the active layer is fullerenes and its derivatives, which are the commonly used as electron acceptor materials in organic solar cells. In 1985, the first fullerene molecule  $C_{60}$  was discovered and prepared by Richard Smalley, Robert Curl, James Heath, Sean O'Brien and Harold Kroto [44]. Fullerenes exhibit unique properties and have been widely applied in material science, electronics and nanotechnology. However,  $C_{60}$  cannot be widely used in solution-processed organic solar cell because of the solubility problem [45]. Therefore, one or multiple addends are required to be introduced into the  $C_{60}$  fullerene leading to  $C_{60}$  derivatives. The  $C_{60}$  derivatives have better solubility while mostly maintaining the excellent electronic properties. Additionally, the number and type of addends also can further tune the electron affinity of fullerene derivatives, which plays an important role in device performance of the solar cells. [6,6]-phenyl- $C_{61}$ -butyric acid methyl ester (PCBM) is one of the popular fullerene derivatives that was firstly synthesized by Fred Wudl's group in 1995 [46]. The fullerene derivative PCBM has been widely used in organic solar cells.

Thus it is particularly important to gain insight into degradation mechanisms of PCBM under water/moisture, oxygen and irradiation conditions.

When blending with different polymers in organic solar cells, PCBM has shown both stabilizing and destabilizing effects under photo-oxidation conditions [47]. On the one hand, fullerenes are considered as good free radical scavengers protecting biological samples from reactive oxygen species [48-51]. Hoke *et al.* [52] demonstrated the effects of electron affinities of fullerenes on the oxygen-based photo-bleaching rate of polymers in polymer: fullerene blends. It indicated polymers blended with fullerene with smaller electron affinities degraded faster. Thus the development of polymers and fullerenes with larger electron affinities may result in more stable photovoltaic cells [52].

Chambon *et al.* investigated the degradation mechanism of poly[2-methoxy-5-(3',7'-dimethyloctyloxy)-1,4-phenylene vinylene] (MDMO-PPV) polymer and PCBM using a combination of infra-red (IR) spectra and UV-vis spectra [22]. According to their experiments, the degradation of MDMO-PPV firstly involved a radical oxidation at the ether functions and secondly at the double bonds. The photo-oxidation of PCBM revealed the oxidation of its C<sub>60</sub> moiety. The photo-oxidation experiment on MDMO-PPV/PCBM blends revealed that degradation occurred on both MDMO-PPV and PCBM components. Additionally, the presence of PCBM in blends decreased the degradation rate of MDMO-PPV by a factor of ten. In MDMO-PPV:PCBM blends, it was concluded that PCBM could protect MDMO-PPV polymer due to its ability as radical scavenger [22].

PCBM may also accelerate the degradation process of polymers because PCBM is capable of inducing active oxygen species [53-55]. Due to its high intersystem crossing (ISC) yield (> 50% in solution), PCBM has the ability to generate singlet oxygen in the presence of oxygen [53-55]. In the solid state [56], the ISC yield is much less, but depends on the degree of crystallinity. PCBM still has the potential to induce singlet oxygen which caused significant degradation.

Similar to the discussion about conducting donor polymers, the photo-induced chemical changes of PCBM films under oxygen atmosphere have been investigated by using a combination of different techniques [22, 23]. The studies showed a strong interaction between oxygen and C<sub>60</sub> moiety in fullerene molecule. By means of matrix-assisted laser desorption/ionization time-of-flight mass spectrometer (MALDI-TOF MS), PCBM thin films showed a stepwise uptake of up to eight oxygen atoms in each fullerene moiety under illumination at ambient conditions [23], leading to gradual lowering of the LUMO level in fullerene.

Bao et al. reported the effects of ambient atmosphere on PCBM films by controlling in-situ the exposure of oxygen and water vapor [57]. Then the chemical and electronic structures were probed by using photoelectron spectroscopy. The measurements revealed that the degradation under oxygen was reversible by thermal treatment in vacuum afterwards, which indicated a weak interaction between oxygen and PCBM molecules. Furthermore, PCBM molecules were reported to show a light-induced dimerization [58-61] and oligomerization [62, 63] under inert atmosphere, which could initiate a possible device degradation mechanism of organic solar cells during photo-illumination process.

### 1.3 Perovskite solar cells

Perovskite solar cell is a new emerging photovoltaic technology which consists of perovskite structured materials as light-absorbing layer. Perovskite was named after the Russian mineralogist Lev Aleksevich von Perovski. It includes a class of compounds which have the same crystal structure known as perovskite structure with a general formula of  $ABX_3$ . The general crystal structure of perovskite materials is shown in Figure 1.6. Organic or inorganic cation A occupies the cuboctahedral holes formed by the 12 nearest-neighboring halide ions. Metal cations B and halides X occupy the grey and purple positions in the crystal structure, respectively. Perovskite solar cells are mostly based on the three-dimensional organic-inorganic hybrid perovskite materials by replacing cation A and B with methylammonium cations ( $CH_3NH_3^+$ ) lead cations ( $Pb^{2+}$ ), respectively.

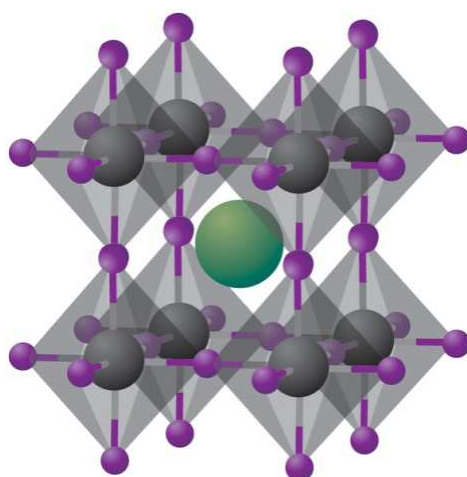


**Figure 1.6:** Crystal structure of cubic metal halide perovskite with a general chemical formula of  $ABX_3$  [64].

Methylammonium lead halide perovskite materials  $\text{CH}_3\text{NH}_3\text{PbX}_3$  ( $X=\text{I}, \text{Br}$  or  $\text{Cl}$ ) especially methylammonium lead iodide  $\text{CH}_3\text{NH}_3\text{PbI}_3$ , is the most commonly used material in perovskite solar cells due to its interesting optical and electronic properties.  $\text{CH}_3\text{NH}_3\text{PbI}_3$  material has a direct bandgap of 1.55 eV which corresponds to an absorption onset at 800 nm [65]. This property makes  $\text{CH}_3\text{NH}_3\text{PbI}_3$  material a good sunlight absorber over the whole visible range. The photo-generated excitons have a weak binding energy of about 0.03 eV, which implies that most of excitons can rapidly dissociate into free charge carriers (electrons and holes) at room temperature [66]. The electrons and holes exhibit high carrier mobility and their recombination occurs at a timescale of hundreds of nanoseconds, leading to long carrier-diffusion lengths ( $> 1 \mu\text{m}$ ) [64, 66-68].

Although perovskite has been discovered decades ago and the unique properties were known before, it attracted little attention until 2009 when two organolead halide perovskites ( $\text{CH}_3\text{NH}_3\text{PbBr}_3$  and  $\text{CH}_3\text{NH}_3\text{PbI}_3$ ) were applied in liquid dye-sensitized solar cells [69]. Recently, the certified power conversion efficiency of perovskite solar cell has exceeded 20% (Figure 1.7) [70].

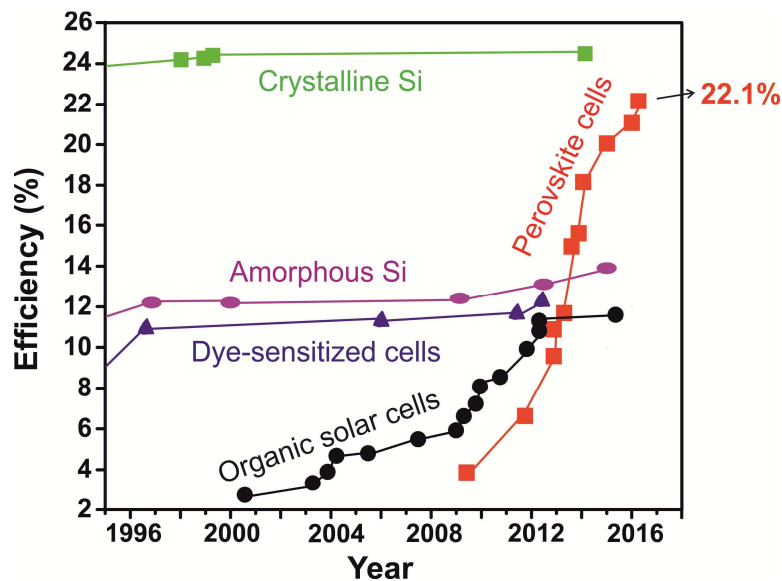


**Figure 1.7:** Best research-cell efficiencies of crystalline/amorphous silicon solar cells, dye-sensitized solar cells, organic solar cells and perovskite solar cells in recent years. (Adapted from National Renewable Energy Laboratory, NRLE).

In 2009, Miyasaka et al. applied  $\text{CH}_3\text{NH}_3\text{PbBr}_3$  and  $\text{CH}_3\text{NH}_3\text{PbI}_3$  perovskite materials into liquid dye-sensitized solar cells which could efficiently sensitize titanium dioxide ( $\text{TiO}_2$ ) for visible light conversion [69]. The corresponding solar cells produced power conversion efficiencies of 3.1% and 3.8% for  $\text{CH}_3\text{NH}_3\text{PbBr}_3$  and  $\text{CH}_3\text{NH}_3\text{PbI}_3$ , respectively [69]. However, the perovskite compounds easily dissolved in the liquid

electrolyte and led to stability problem of the solar cells. The successful solution for instability problem was to replace the liquid electrolyte with a solid hole transporting materials (HTM), such as 2,2'-7,7'-tetrakis-(N,N-di-p-methoxyphenylamine)-9,9'-spirobifluorene (spiro-OMeTAD) [71-73]. The mesoporous TiO<sub>2</sub> structure was usually used as a scaffold for the methylammonium perovskite materials (Figure 1.8a) [69, 71]. In 2012, a solid-state mesoscopic heterojunction solar cell based on CH<sub>3</sub>NH<sub>3</sub>PbI<sub>3</sub> perovskite was produced by using solution processed method with a power conversion efficiency of 9.7% [71]. By replacing the mesoporous TiO<sub>2</sub> layer with aluminium oxide (Al<sub>2</sub>O<sub>3</sub>) as a scaffold, the power conversion efficiency was increased to 10.9% in a single-junction device [72].

Although the perovskite solar cells have reached significant efficiencies by using mesoporous structure [71, 72, 74], the fabrication of mesoporous structure requires high temperature above 450 °C. The latter increases the production time and cost. Furthermore, it has been reported that methylammonium-based perovskite materials exhibit long charge carrier diffusion lengths [68, 75]. The studies also indicate that perovskite materials show excellent ambipolar charge transport property, which means that perovskite material itself can transport both electrons and holes between the electrodes [75]. The mesoporous TiO<sub>2</sub> layer has been proven to be not necessary for high efficiency perovskite solar cells and a planar structure is feasible. In 2013, Jeng et al. reported the first successful planar perovskite solar cells based on CH<sub>3</sub>NH<sub>3</sub>PbI<sub>3</sub> perovskite/fullerene with an efficiency of 4% [76]. Recently, the efficiency of planar-heterojunction perovskite solar cells has exceeded 19% through suitable interface engineering [73]. All the results indicated that planar-structure based perovskite solar cells could reach comparative device performance as the mesoporous structure devices.

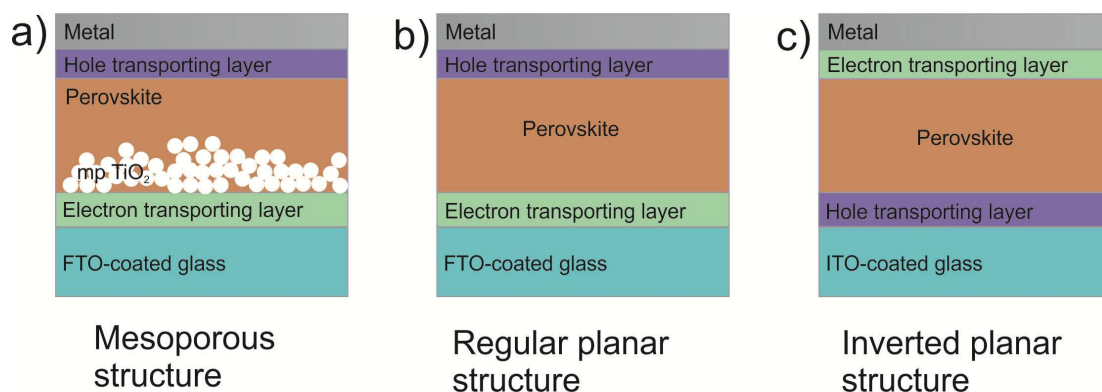


**Figure 1.8:** The typical structure evolution of perovskite solar cells, a) mesoporous structure, b) regular planar structure and c) inverted planar structure.



The planar-heterojunction perovskite solar cells include regular planar structure and inverted planar structure as shown in Figure 1.8b and 1.8c, respectively. The regular planar perovskite solar cell requires above 450 °C treatment to obtain high-quality condensed TiO<sub>2</sub> compact layer, which increases the production cost and limits the development of perovskite solar cells. The inverted planar perovskite solar cells are derived from organic solar cells. Indium tin oxide (ITO) is a transparent conducting substrate which has the potential to provide low-cost, flexible solar cells. The traditional hole transporting layer poly(3,4-ethylenedioxythiophene) polystyrene sulfonate (PEDOT:PSS) and electron transporting layer PCBM fullerene derivate which were used in organic solar cells were directly implemented in inverted planar perovskite solar cells. In the beginning, the inverted planar perovskite solar cell had an efficiency of 3.9% [76]. By optimizing the processing conditions, the efficiencies of inverted planar perovskite solar cells have increased significantly [77-80]. Recently, Heo et al. reported a high quality perovskite film based on PEDOT:PSS with an additive of HI, which achieved an efficiency of 18.1% [81].

Due to the commercial applications of solar cell technologies, easy and low-temperature processing approaches are necessary for fabricating perovskite solar cells. The commonly used solution-processed method is shown in Figure 1.9. Here, the precursor materials lead chloride (PbCl<sub>2</sub>) and methylammonium iodide (CH<sub>3</sub>NH<sub>3</sub>I) are mixed into an organic solvent (i.e. N,N-dimethylformamide, DMF) with a certain molar ratio. Then the mixed precursor solution is dropped onto a pre-cleaned PEDOT:PSS coated-substrate and doing spin-coating afterwards. The organic solvent will evaporate during spin-coating and the precursor film is formed. After thermal annealing treatment at a certain temperature for a certain time, CH<sub>3</sub>NH<sub>3</sub>PbI<sub>3</sub> perovskite film is obtained. The preparation of inverted planar perovskite solar cells requires low-temperature condition below 150 °C. In my thesis, I will focus on the inverted planar structure of CH<sub>3</sub>NH<sub>3</sub>PbI<sub>3</sub> perovskite solar cells. In particular I investigated the crystallization process and stability of CH<sub>3</sub>NH<sub>3</sub>PbI<sub>3</sub> films dependent on temperature and humidity. Both aspects will be further discussed in the following parts.



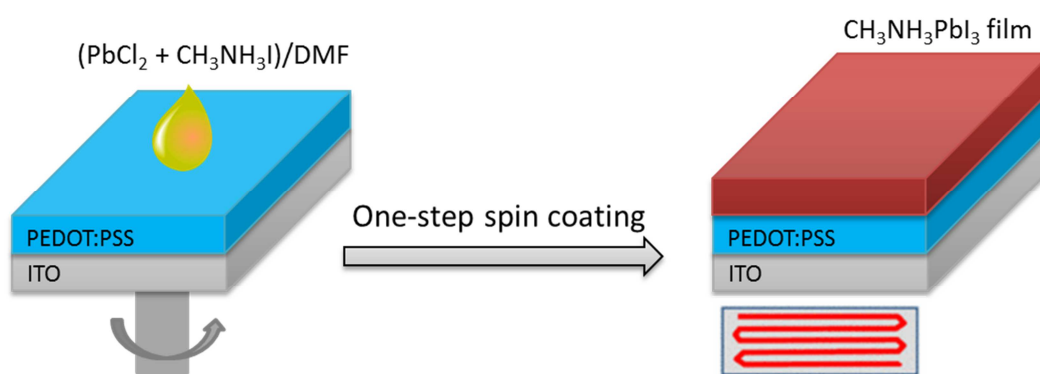


**Figure 1.9:** Schematic of perovskite film prepared by spin-coating method from pre-mixed precursor solution of lead chloride ( $\text{PbCl}_2$ ) and methylammonium iodide ( $\text{CH}_3\text{NH}_3\text{I}$ ).  $\text{CH}_3\text{NH}_3\text{PbI}_3$  perovskite film is obtained after thermal annealing treatment.

### 1.3.1 Crystallization issue in perovskite films

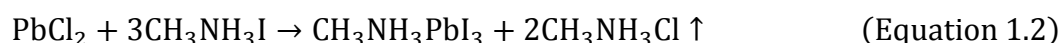
Low-temperature solution-processing method offers the potentials for fabricating perovskite solar cell in a large scale. One critical factor for solution-processed method is the morphology quality of perovskite films which is highly related to its power conversion efficiency [82-87]. However, solution-processed perovskite films tend to have pinholes, poor surface coverage, resulting in current leakage due to the shunting pathways via direct contact of electron transporting layer and hole transporting layer [87, 88]. The film morphology should be carefully controlled by varying the processing conditions, such as the use of mixed solvent [89, 90], sequential deposition method [91], annealing protocol [82, 83, 85, 92] and annealing atmospheres (i.e. in air, vacuum, moisture) [79, 86, 93-95].

To improve the morphology quality of perovskite films, several approaches have been applied to control film crystallization process. In the beginning,  $\text{CH}_3\text{NH}_3\text{PbI}_3$ -based perovskite solar cells were recommended to be fabricated in a controlled environment with a humidity level of  $< 1\%$  [91]. Since the  $\text{CH}_3\text{NH}_3^+$  is water soluble and the  $\text{CH}_3\text{NH}_3\text{I}$  solvation could be the first step of  $\text{CH}_3\text{NH}_3\text{PbI}_3$  degradation [96]. The excess water can induce the corruption of perovskite crystal structure. But afterwards, the mild moisture was proved to have a positive effect on the formation of perovskite films. In 2014, You et al. reported one moisture-assisted grain growth method which allows preparing the  $\text{CH}_3\text{NH}_3\text{PbI}_3$  perovskite film in a humid environment [79]. When the perovskite precursor films were annealed in ambient air with humidity of  $35\% \pm 5\%$ , the perovskite film had increased individual crystal size, less pin-holes and increased grain size. This method produced perovskite solar cells with a maximum power conversion efficiency of 17.1% and a fill factor of 80% [79]. Moisture might partially

dissolve the reactant species and then improve the reconstruction process during film formation [97].

Xie et al. proposed another vacuum-assisted thermal annealing method to control the composition and morphology of  $\text{CH}_3\text{NH}_3\text{PbI}_3$  films by removing the  $\text{CH}_3\text{NH}_3\text{Cl}$  byproduct during their formation [86]. A pure, pore-free planar  $\text{CH}_3\text{NH}_3\text{PbI}_3$  film was produced with high power conversion efficiency of 14.5% in the corresponding solar cell. This approach demonstrates that the removal of  $\text{CH}_3\text{NH}_3\text{Cl}$  significantly improves device stability and reproducibility [86]. The introduction of additives, such as 1,8-diodooctane (DIO) and 1-chloronaphthalene (CN) into perovskite precursor solutions produced perovskite films with more smooth and homogenous morphology which have fewer pin-holes and better surface coverage [98, 99]. These results indicated that additives play an important role in the crystallization process of perovskite films.

In spite of the positive effects of the above methods on film quality, there is still lack of fundamental understanding on the film crystallization mechanism to achieve higher efficiency. Additionally, one-step deposition method is considered as a promising approach for fabricating low-cost perovskite solar cell with high efficiency. But it is still lack of well control over perovskite film growth which leads to poor film quality and low surface coverage. Therefore, it is extremely important to have a better understanding on the film crystallization process in order to optimize perovskite thin films.  $\text{CH}_3\text{NH}_3\text{I}$  and  $\text{PbCl}_2$  or  $\text{PbI}_2$  mixture are the most commonly used precursor materials in the deposition fabrication method. After spin-coated onto substrate, the precursor film requires thermal annealing treatment at a certain temperature for a certain time to form perovskite crystals. One category is via the reaction between  $\text{PbI}_2$  and  $\text{CH}_3\text{NH}_3\text{I}$  with a molar ratio of 1:1 which leads to the formation of  $\text{CH}_3\text{NH}_3\text{PbI}_3$  (Equation 1.1). The other one is by means of the reaction between  $\text{PbCl}_2$  and  $\text{CH}_3\text{NH}_3\text{I}$  precursor materials with a molar ratio of 1:3 (Equation 1.2). Especially for ( $\text{PbCl}_2+\text{CH}_3\text{NH}_3\text{PbI}_3$ ) based method, several studies showed that the precursor materials couldn't directly transform into perovskite crystals, but through a serial of intermediate organometal mixed halide phases together with the release of byproducts [82, 100, 101].



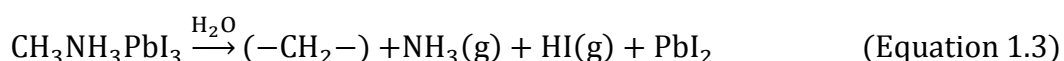
Tan et al. [84] and Moore et al. [102] used in-situ X-ray scattering method to study the phase transformation process of perovskite films. It shows that three distinct structures appeared during thermal annealing process: precursor,  $\text{CH}_3\text{NH}_3\text{PbI}_3$  perovskite crystals and decomposed products. But the reaction pathways are more

complex than expected. Wang et al. [144] proposed a multistep reaction using in-situ X-ray diffraction which was to probe the crystal structure evolutions. Some intermediate phases appeared during thermal annealing process, such as  $\text{PbI}_2$ ,  $\text{CH}_3\text{NH}_3$ ,  $\text{HCl}$ ,  $\text{CH}_3\text{NH}_3\text{PbCl}_3$ . The film morphology evolution is associated with the chemical reaction and crystallization process, which is still under debate.

### 1.3.2 Stability issue in perovskite films

For practical applications, a reliable and stable device performance is highly required. However, the present studies have shown that the stability of  $\text{CH}_3\text{NH}_3\text{PbI}_3$  based perovskite solar cells is still a critical issue. The main problem is that  $\text{CH}_3\text{NH}_3\text{PbI}_3$  perovskite material is not stable under high humid environment, because  $\text{CH}_3\text{NH}_3^+$  can easily diffuse from perovskite materials and dissolve into a polar solvent such as water. When exposed  $\text{CH}_3\text{NH}_3\text{PbI}_3$  perovskite films to detrimental environments such as humid environment, the dark brown  $\text{CH}_3\text{NH}_3\text{PbI}_3$  films underwent decomposition into lead iodide ( $\text{PbI}_2$ ) or other byproducts [103-107].

Niu et al. studied the stability of  $\text{CH}_3\text{NH}_3\text{PbI}_3$  perovskite films when exposed them at humid environment by using UV-vis spectra and X-ray diffraction measurements [105]. In the report, they suggested that  $\text{CH}_3\text{NH}_3\text{PbI}_3$  films would decompose into methylammonium iodide ( $\text{CH}_3\text{NH}_3\text{I}$ ) solution and  $\text{PbI}_2$  solid in the presence of  $\text{H}_2\text{O}$ . A post-modification method using aluminum oxide ( $\text{Al}_2\text{O}_3$ ) could protect perovskite films from degradation by moisture and sunlight [105]. Another similar decomposition mechanism of  $\text{CH}_3\text{NH}_3\text{PbI}_3$  perovskite was proposed by Frost et al. in the presence of water [108]. Here, water molecule is required to initiate the decomposition process. An excess of water molecules are necessary to dissolve the decomposed byproducts  $\text{HI}$  and  $\text{CH}_3\text{NH}_2$ . In the presence of enough water, the  $\text{CH}_3\text{NH}_3\text{PbI}_3$  perovskite entirely degraded into  $\text{PbI}_2$  species [108]. Li et al. studied the degradation of  $\text{CH}_3\text{NH}_3\text{PbI}_3$  perovskite films when exposed to oxygen, atmospheric air and water by using X-ray photoelectron spectroscopy and X-ray diffraction [109]. The results showed that  $\text{CH}_3\text{NH}_3\text{PbI}_3$  was not sensitive to oxygen, and further confirmed that  $\text{H}_2\text{O}$  played an important role in the degradation process of  $\text{CH}_3\text{NH}_3\text{PbI}_3$  film, which might induce the decomposition as the following equation:



Yang et al. [103] and Christians et al. [104] proposed another different degradation pathways with the formation of a pale yellow hydrated intermediate phase  $(\text{CH}_3\text{NH}_3)_4\text{PbI}_6 \cdot 2\text{H}_2\text{O}$  in high humid environment. This hydrated phase was not stable under dry gas or storing in vacuum, which could rapidly dehydrated and regenerated

the characteristic dark brown color of  $\text{CH}_3\text{NH}_3\text{PbI}_3$  film. This phenomenon was accompanied by a partial recovery of perovskite absorbance which indicated partially reversibility of the hydrated phase  $(\text{CH}_3\text{NH}_3)_4\text{PbI}_6 \cdot 2\text{H}_2\text{O}$  [103, 104]. In addition, the detailed investigation on  $(\text{CH}_3\text{NH}_3)_4\text{PbI}_6 \cdot 2\text{H}_2\text{O}$  crystal structure and the reversible conversion process between  $\text{CH}_3\text{NH}_3\text{PbI}_3$  and  $(\text{CH}_3\text{NH}_3)_4\text{PbI}_6 \cdot 2\text{H}_2\text{O}$  has been reported previously [110].

Recently, Leguy et al. [111] introduced a degradation model of  $\text{CH}_3\text{NH}_3\text{PbI}_3$  upon exposure of the compound to humidity. First, a monohydrate phase  $\text{CH}_3\text{NH}_3\text{PbI}_3 \cdot \text{H}_2\text{O}$  at an early humidity induced-degradation stage was observed, which was fully reversible back to  $\text{CH}_3\text{NH}_3\text{PbI}_3$  upon subsequent drying in gas (Figure 1.10). Second, a dihydrate phase  $(\text{CH}_3\text{NH}_3)_4\text{PbI}_6 \cdot 2\text{H}_2\text{O}$  formed upon longer exposure time. Leguy et al. found that the hydration process was isotropic and homogeneous throughout the film [111]. Based on time-resolved ellipsometry, X-ray diffraction and JV measurements, Leguy et al. proposed a microscopic degradation mechanism. The hydration of the  $\text{CH}_3\text{NH}_3\text{PbI}_3$  led to a separation of grains which resulted in electrical isolation and increased charge recombination at the grain interface. Interestingly, the JV behavior recovered almost to its original state upon subsequent drying of the film. However, Leguy et al. noticed that the JV curve did not totally recover to its original shape. The difference between two JV curves before and after moisture exposure might be associated with perovskite crystal size. In another context, Kim and Park reported that a decrease in crystal size led to an increasing hysteresis [112].

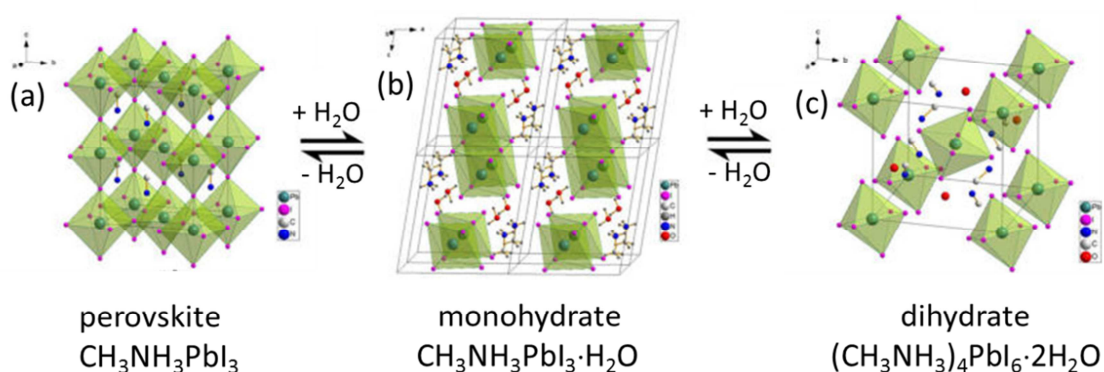


**Figure 1.10:** Crystal structures of  $\text{CH}_3\text{NH}_3\text{PbI}_3$  in its cubic phase (a), monohydrate phase  $\text{CH}_3\text{NH}_3\text{PbI}_3 \cdot \text{H}_2\text{O}$  (b) and dihydrate phase  $(\text{CH}_3\text{NH}_3)_4\text{PbI}_6 \cdot 2\text{H}_2\text{O}$  (c) [111].

## 1.4 Motivation

Scanning force microscopy (SFM) is an ideal technique to probe the film morphology at a nanometer scale. Compared with scanning tunneling microscopy, which could only be used on conducting samples, the invention of SFM extended the applications on non-conducting samples. The application of SFM technique allows investigating sample in various environments, such as in air and liquid. Furthermore, when combined with a hermetically sealed sample chamber, the SFM allows performing experiments under high vacuum, a purged gas. Thus the morphology evolution can be observed as a function of environmental changes while scanning. In combination with a heating stage the reactions or crystallization process as a function of heating temperature and time can be studied on a nanometer scale.

The SFM provides information about the morphology evolution of film sample, while the application of X-ray diffraction technique enables us to probe crystalline structure. Each crystalline solid has its own characteristic X-ray powder pattern, which can be used as a “fingerprint” for its identification. Furthermore, in-situ X-ray diffraction technique provides time-resolved analysis of the crystalline films under controlled environments. The detailed observation of X-ray diffraction pattern in the reflection intensities and reflection positions reveals the information on the crystalline solid, their growth or decomposition products [113].

In the present work, I focus my studies on the crystallization and degradation processes of perovskite films under a controlled environment. The in-situ SFM, ex- and in-situ X-ray diffraction techniques are performed to track changes in film morphology and the crystalline structure. In addition to SFM and X-ray diffraction techniques, the UV-vis spectra, matrix-assisted laser desorption/ionization time-of-flight mass spectrometry (MALDI-TOF MS) and X-ray photoelectron spectroscopy (XPS) also have been used to obtain specific chemical information on the degradation products of organic solar cell material and elemental composition of perovskite film surface. The working principle and detailed description of the above approaches will be presented in **Chapter 2: Experimental Methods**, which also consists of the detailed experimental procedures.

The device performance is highly dependent on the perovskite film morphology. High-quality perovskite film with smooth surface, large grain size and full surface coverage is required for high power conversion efficiency of perovskite solar cells [82, 83, 86, 114-116]. Several key factors such as the deposition method, additives and film treatment can influence the film quality and should be optimized to control morphology. Besides,

the crystallization process also plays a vital role in understanding the film growth mechanism during thermal annealing treatment. In my work I performed in-situ SFM measurements under controlled environments to track the morphology evolution of  $\text{CH}_3\text{NH}_3\text{PbI}_3$  perovskite films during thermal annealing process (**Chapter 3: Thermal crystallization and decomposition of  $\text{CH}_3\text{NH}_3\text{PbI}_3$  films**). Combined together with ex-situ X-ray diffraction technique, these measurements allowed us to observe the crystalline structure changes during the in-situ heating process.

The  $\text{CH}_3\text{NH}_3\text{PbI}_3$  perovskite films are very sensitive to high humid environment which will induce a decomposition of the perovskite film. Several degradation pathways have been observed under high humid environment [103, 105, 108, 111]. The degradation of  $\text{CH}_3\text{NH}_3\text{PbI}_3$  perovskite films could lead to a decline in device performance and an increase in the JV hysteresis [111]. In my work, the  $\text{CH}_3\text{NH}_3\text{PbI}_3$  perovskite films were exposed to different humid environments (0%, 20%, 50% and 80%) in the dark at room temperature (**Chapter 4: Humidity-induced degradation of  $\text{CH}_3\text{NH}_3\text{PbI}_3$  perovskite films**). In-situ SFM and in-situ X-ray diffraction measurements were performed to track the changes in film morphology and crystal structure during the humidity-induced degradation process. In this way, I was able to refine the degradation model proposed recently by Leguy and co-workers [111].

As a popular fullerene derivative, [6,6]-phenyl- $\text{C}_{61}$ -butyric acid methyl ester (PCBM) has been widely used as electron acceptor material in polymer solar cells [117]. Additionally, PCBM also acts as an ideal material in perovskite solar cells which can minimize the hysteretic effects at interfaces and increase power conversion efficiency [118, 119]. The photo-oxidation of PCBM film is one of the problems for the stability of solar cell devices. Sengupta observed an increase in the thickness of PCBM films at lower illumination dose at oxygen atmosphere, and a decrease at higher illumination dose [120]. The reason for this phenomenon could be that PCBM underwent series of chemical changes during photo-oxidation process. In **Chapter 5: Photo-oxidation of PCBM films**, MALDI-TOF experiments were carried out to compare the reference PCBM film and photo-oxidized PCBM films. The results gave us direct information of chemical structure changes of PCBM materials during photo-oxidation process.

# Chapter 2

## Experimental methods

Here, I will present the fundamental working principles of scanning probe microscopy (SPM), UV-vis absorption spectroscopy, X-ray diffraction pattern (XRD), matrix-assisted laser desorption/ionization time-of-flight (MALDI-TOF) and X-ray photoelectron spectroscopy (XPS). In addition, I will also explain how these methods were applied and how the experiments were carried out.

### 2.1 Scanning Probe Microscopy

In SPM, a small sharp probe is used to detect the local properties of sample surface or interface. By scanning forth and back, the detected properties are collected and represented as an image. In 1981, Scanning Tunneling Microscopy (STM) was invented by Gerd Binnig and Heinrich Rohrer who earned the Nobel Prize in Physics in 1986. The disadvantage of STM is that this technique can be used only for conducting samples since the tunneling current between the probe and sample is measured in STM experiments. The limitation of STM led to the invention of Scanning Force Microscopy (SFM) in 1986 by Gerd Binnig, Calvin Quate and Christoph Gerbe [121]. In SFM, a sharp probe is used to scan over the sample surface and the forces between the tip and sample are measured accordingly. The process of gathering surface information is like to feel or touch a surface with a mechanical probe.

#### 2.1.1 Working principle

Typically, the probe in SFM technique is one tip mounted at the end of a cantilever holder which is usually made from silicon or silicon nitride (Figure 2.1). The tip can be very sharp even down to a single atom and it moves precisely forth and back across the sample surface. The forces between tip and sample such as van der Waals force, electrostatic force can lead to a deflection of the cantilever according to Hooke's law (Equation 2.1). Here  $F$  is the force between tip and sample,  $k$  is spring constant of the cantilever and  $x$  is the deflection changes of cantilevers relative to its equilibrium position without tip-sample interaction.

$$F = -kx \quad \text{(Equation 2.1)}$$



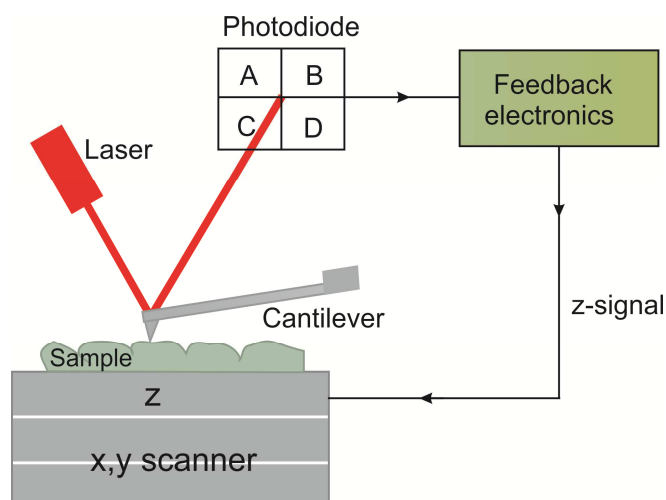


**Figure 2.1:** Schematics of scanning force microscopy operated by using beam deflection detection system.

SFM consists of two main modules as shown in Figure 2.1. The first module is the piezoelectric scanner which moves the sample in x, y and z directions. The second module is the detection system, which includes laser, cantilever, photodiode, feedback electronics control. As the tip is scanning over the sample surface, the deflection changes of cantilever are detected using the laser beam from backside of cantilever into a position-sensitive photodetector. The photo-detector consists of four side-by-side photodiodes (Figure 2.1). Any small changes on cantilever deflection will lead to a subsequent change in the position of laser beam on photo-detector. The difference between the four photodiode signals indicates the position of the laser beam on the detector and reveals the deflection of the cantilever. For instance, the difference in signal between A, B and C, D stated as  $(A+B)-(C+D)$  gives vertical deflection (in volts or amps). The difference of signal  $(B+D)-(A+C)$  gives the lateral deflection. The changes in cantilever deflection can be converted to force at a pN scale using Hooke's equation. When tip is scanning on the sample surface at a constant position, it can be easily damaged due to the topography features of sample. Therefore, a feedback electronics control is necessary to physically move the tip closer or further away from surface in z axis. In this case, a constant force between tip and sample surface is maintained.

### 2.1.2 Imaging modes

The SFM can be operated in static and dynamic modes which depend on tip-sample force interactions. In SFM, the measured quantity is the force between tip and sample. Typically, the forces are coulombic and van der Waals interactions. In Figure 2.2, a



schematic of the force between tip and sample is presented. There are three regimes which can be distinguished. In regime (1), when the tip is far away from sample surface, there is no interaction between tip and sample. So the force between tip and sample can be negligible. In regime (2), as the tip is gradually brought close to sample surface, the atoms of the tip and sample attract each other. An attractive force is formed between tip and sample. As the tip is further approaching to sample surface, the attractive force between tip and sample increases. In regime (3), when there is very small distance (a few angstroms Å), a strong repulsive force between tip and sample becomes dominant. Its origin comes from exchange interactions due to the overlap of electronic orbitals of tip and sample atoms. In this case, the tip and sample surface are usually considered to be in “contact”.

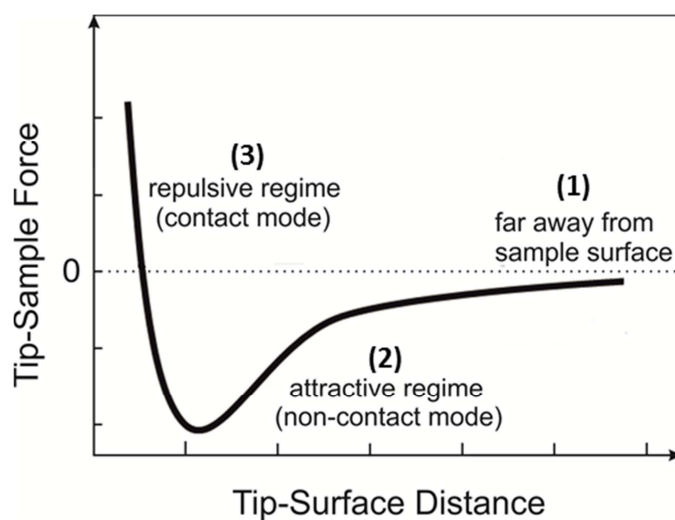


**Figure 2.2:** Force between tip and sample as function of tip-to-sample distance.

In order to measure topography, different imaging modes have been developed, which are usually divided into contact mode, tapping mode and non-contact mode. The contact mode is also called as static operation mode. In contact mode, the tip is scanning on the sample surface in such a way that the force between tip and sample is kept constant. The z piezo moves the tip up and down to keep the deflection of cantilever constant. The positions of z piezo are recorded as sample topography. However, contact mode imaging is always in contact with sample surface, which can damage both tip and sample surface. This mode is even worse for soft sample which are easily distorted or damaged or even removed from substrates.

The **intermittent contact mode** also referred to “Tapping Mode<sup>TM</sup>” can be a better option for soft samples such as polymers and biological materials. In intermittent contact mode, the cantilever is excited to oscillate by an additional piezoelectric element which is attached to the cantilever holder. The tip is vibrated with amplitude

of 1-100 nm at a frequency close to its resonant frequency [122]. When the tip is brought to sample surface, the resonance frequency of the cantilever will change due to the force between tip and the sample surface. An attractive force between tip and sample surface induces a lower resonance frequency of the cantilever, and a repulsive force leads to increased resonance frequency.

In order to keep the oscillation amplitude constant, the z-piezo varies the distance between tip and sample by lifting the tip away from the sample surface. By recording the z-piezo signal as a function of tip position, an image on the height features of the sample is obtained. In addition, the phase shift signals also can be recorded as an image, named as phase image. The phase shift of a oscillating tip is strongly dependent on the tip-sample interactions, thus phase image is useful to distinguish the material properties (i.e. adhesion, viscosity or plasticity) of analyzed samples [123]. The intermittent contact mode SFM has some advantages and is a very widely applied technique. The short-time interactions between the tip and sample surface within minimal shear are less damaged to sample surface compared to the direct tip-sample force in contact mode SFM. This technique is much gentler and can be used to measure soft samples without damaging analyzed sample and tip.

### **2.1.3 EnviroScope Scanning Force Microscopy**

In this case, the SFM works under a controlled environmental atmosphere with a hermetically sealed sample chamber (Figure 2.3). The sample chamber can be connected with dry air, nitrogen (N<sub>2</sub>), argon (Ar) gas resources *etc.*, which allows observing sample evolution under a certain environments. EnviroScope SFM can also be applied to control the humidity of sample chamber at a range of 0-100% humidity level. The humidity control setup was used to obtain a certain humidity level (Figure 2.3a). Here, the dry N<sub>2</sub> gas was used and separated into two pathways. In one pathway, the dry N<sub>2</sub> was bubbled through a water solution obtaining the water vapor gas. The other pathway was through a dry silica gel getting a dry N<sub>2</sub>. One clean tube was used to connect the mixed humid gas and the inlet of EnviroScope SFM chamber. Another clean tube was used on the outlet of EnviroScope SFM which was immersed into water bath. The precise humidity level could be controlled by adjusting the relative flow speed of saturated water vapor and the carrier gas dry N<sub>2</sub>. Except for the inlet and outlet, the EnvironScope SFM chamber was well sealed and very little amount of humid gas could leak out of the chamber. Therefore, the humidity level of the EnvironScope SFM chamber was very stable and reliable during measurement. In addition, an in-house made humidity sensor (SHT15, humidity accuracy  $\pm 2.0\%$ ) is

located inside the sample chamber which is close to sample in order to continually detect the precise relative humidity inside.

The EnviroScope SFM is also suitable for heating samples in-situ combined with a high temperature heater stage, allowing a local observation of sample reactions/revolution at different temperatures. The high temperature heating stage with a Lakeshore Model 331 temperature controller varies sample temperature from room temperature up to 185 °C in ambient environment, and from ambient up to 275 °C in vacuum (to 300 °C nominal at the sample).

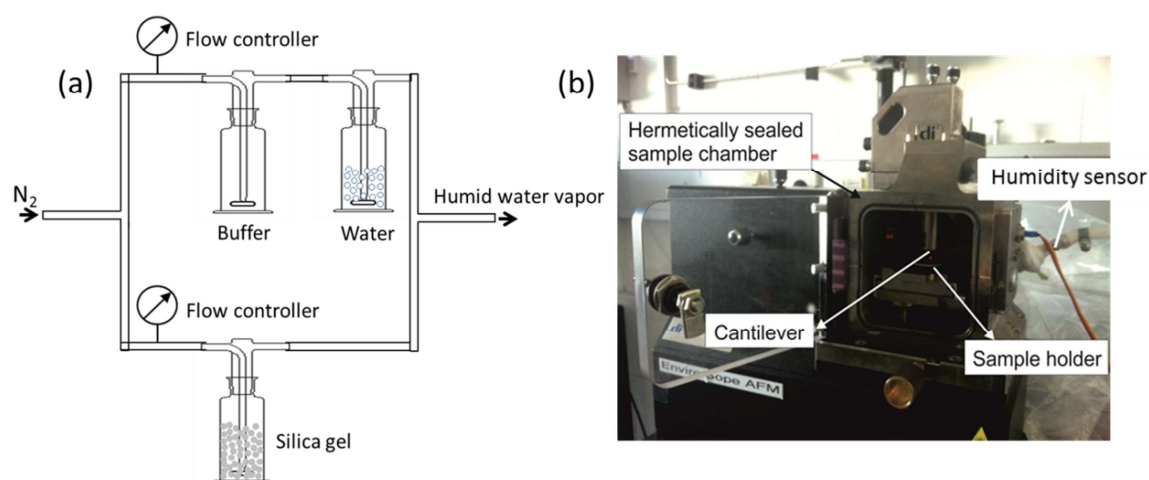


**Figure 2.3:** (a) Schematic of humidity control setup, and (b) experimental setup of EnviroScope SFM device which allows performing measurements under different atmospheres.

### SFM on CH<sub>3</sub>NH<sub>3</sub>PbI<sub>3</sub> perovskite materials

SFM has been proven to be an effective characterization tool to study the morphology as well as other physical properties of perovskite film [94, 124, 125]. Especially in intermittent mode, SFM does not require any sample treatment which may change the physical information of detected samples.

SFM technique has been widely applied on the characterization of CH<sub>3</sub>NH<sub>3</sub>PbX<sub>3</sub> perovskite films. Typically, the CH<sub>3</sub>NH<sub>3</sub>PbX<sub>3</sub> films are spin-coated from a precursor solution including CH<sub>3</sub>NH<sub>3</sub>I and lead source PbX<sub>2</sub> (X=Cl, Br, I) and then performed thermal annealing. The concentration of precursor, the lead source and mixed molar ratio of CH<sub>3</sub>NH<sub>3</sub>I and PbX<sub>2</sub> play an important role in the film topography and the corresponding device performance [85, 125-126]. In addition, the annealing atmosphere during film preparation also affects the film topography. Raga et al. studied the influence of annealing atmosphere on the planar perovskite solar cells [94].

It indicated that the perovskite film prepared under air annealing showed larger perovskite crystal grains which exhibited higher device efficiency [94].

Furthermore, the degradation of perovskite films has been investigated under different detrimental environments (i.e. humidity, light), which is still one of the practical problems for their commercialization [103, 104, 111, 127,]. The degradation of perovskite film could induce the decomposition of big perovskite crystal into small crystals, which led to a declining device performance [103-107]. SFM technique is a powerful tool to study the morphology degradation of perovskite films, allowing ex-situ and in-situ observation.

## 2.2 UV-vis absorption spectroscopy

Ultraviolet and visible (UV-vis) absorption spectroscopy refers to an absorption spectroscopy or reflectance spectroscopy in the spectrum range of ultraviolet (200-400 nm) and visible (400-700 nm). The fundamental principle behind UV-vis absorption spectroscopy is based on the theory that different molecules absorb ultraviolet and visible lights at different wavelengths. When molecules consisting of  $\pi$  electrons or  $n$  electrons absorb ultraviolet or visible lights, the corresponding electrons are excited from a Highest Occupied Molecular Orbital (HOMO) to Lowest Unoccupied Molecular Orbital (LUMO). The electronic excitation between energy levels is related to the molecular orbitals in a molecule.

One example of electronic excitation in a conjugated molecule is described in Figure 2.4. Here,  $\pi$  orbitals are the occupied molecular orbitals with lowest energy,  $\pi^*$  orbitals are called as the highest energy state. The energy difference between the LUMO and HOMO orbitals in the ground state is the HOMO-LUMO bandgap of a conjugated molecule. The relationship between the energy  $E$  of a photo and the wavelength of the light  $\lambda$  is shown in Figure 2.4, where  $h$  is the Planck's constant with a value of  $6.626 \times 10^{-34}$  J·s,  $c$  is the speed of light with a value of  $2.998 \times 10^8$  m/s.

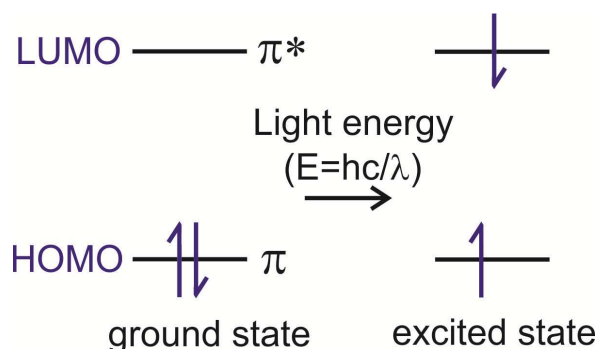


**Figure 2.4:** Electronic transition in a  $\pi$ - $\pi$  conjugated molecule.

A UV-vis absorption spectroscopy records the region of absorption wavelength, and the absorption degree at each wavelength. The UV-visible absorption spectrum is presented as a graph of absorption versus light wavelength. The wavelength at which has the maximum absorption is defined as  $\lambda_{\max}$ .

For the  $\text{CH}_3\text{NH}_3\text{PbI}_3$  perovskite materials used in photovoltaic devices, the absorption spectrum covers in the UV-visible region, which exhibits a broad absorption across from 400 nm to 800 nm (Figure 2.5). The onset at around 780 nm corresponds to the material's optical band gap ( $E_g$ ) of 1.58 eV [128]. When the  $\text{CH}_3\text{NH}_3\text{PbI}_3$  perovskite film undergoes degradation under detrimental environments, UV-visible absorption spectroscopy can be used to measure the loss of film absorption due to degradation. Yang et al. investigated the degradation rate and mechanism under controlled humid environments [103].

$\tau_{1/2}$  was used to determine the degradation rate of  $\text{CH}_3\text{NH}_3\text{PbI}_3$  film which was defined as the point at which the normalized absorbance was halfway between its initial and final values. The data showed  $\tau_{1/2} \approx 4$  hours for a relative humidity of 98%, while  $\tau_{1/2} \approx 34$  hours for 80% humidity. The results implied that higher humidity led to faster degradation process [103]. Additionally, Christian et al. studied the degradation of perovskite film under humid environment [104]. They observed the absorption decay across the entire visible spectrum which indicated that  $\text{CH}_3\text{NH}_3\text{PbI}_3$  perovskite film was degraded through an intermediate phase. From their results it can be concluded that UV-visible absorption spectroscopy is an effective technique to study the degradation mechanism of  $\text{CH}_3\text{NH}_3\text{PbI}_3$  perovskite film.

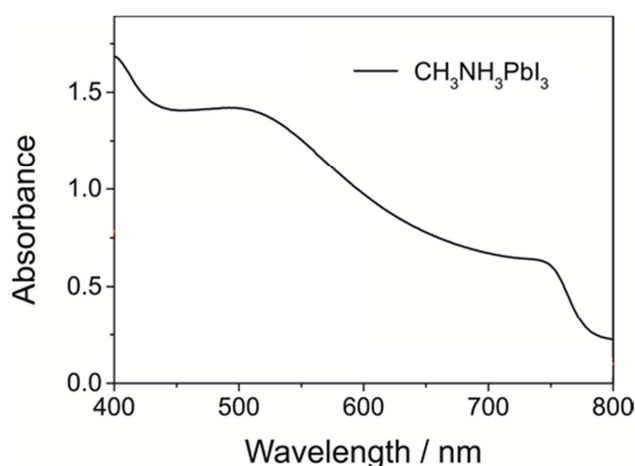


**Figure 2.5:** UV-visible absorption spectra of a pristine  $\text{CH}_3\text{NH}_3\text{PbI}_3$  perovskite film (black solid line) with absorption onset at around 780 nm.

## 2.3 X-ray diffraction

In general, X-rays are defined as electromagnetic waves when the corresponding energies range from 100 eV to 10 MeV. The wavelengths of X-rays are usually in the range 10 to  $10^{-3}$  nm. Photo energies above 5-10 eV (with wavelength below 0.2-0.1 nm) are called hard X-rays [129]. X-rays with lower photo energies are called soft X-rays. The wavelength of X-rays is around the same size as an atom. Crystals consist of regular arrays of atoms. Thus the X-rays can be applied to probe crystalline structure at atomic level.

In X-ray diffraction technique, X-rays are usually generated from one X-ray tube. Afterwards X-rays are filtered and concentrated into a monochromatic beam and then focused on the analyzed crystals. The incoming X-ray beam (coming from upper left in Figure 2.6) interacts with electrons in atoms and produces constructive interference by producing diffracted X-rays, which satisfies Bragg' Law:

$$2d\sin\theta = n\lambda \quad (\text{Equation 2.2})$$

Here,  $d$  is the spacing between diffracting planes,  $\theta$  is the incident angle,  $\lambda$  is the wavelength of the X-ray beam and  $n$  is the integer determined by the order of diffraction. The X-ray diffraction pattern is obtained by measuring the intensity of scattered waves as a function of diffraction peaks. The position of observed diffraction peak, which is recorded as the detector angle  $2\theta$ , is related to the planes of atoms. Each diffraction peak indicates a family of lattice planes. The intensity of the diffraction peaks is determined by the atoms arrangement in the whole crystal structure. The strong intensity known as Bragg angle is obtained in the X-ray diffraction pattern when the scattered wave satisfies Bragg's Law. When the size of detected particles is in nanometer scale, their average size can be calculated by using Scherrer equation:  $\tau = \frac{K\lambda}{\beta\cos\theta}$ . Here,  $\tau$  is the average size of detected particles.  $K$  is a dimensionless shape factor and its typical value is about 0.9.  $\lambda$  is the X-ray wavelength.  $\beta$  is the line broadening that come from line broadening at half the maximum intensity (FWHM) subtracting the instrumental line broadening.  $\theta$  is the Bragg angle.

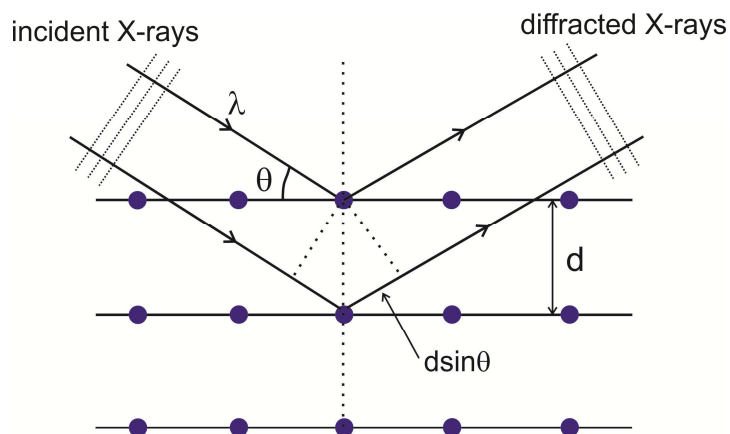


**Figure 2.6:** Illustration for the derivation of Bragg's Law.

Up to now, the Bragg's Law is one of the most important laws used for interpreting X-ray diffraction pattern. This law relates the wavelength of electromagnetic radiation to the diffraction angle and the lattice spacing through a range of  $2\theta$  angles. Furthermore, X-ray diffraction has become a unique non-destructive analytical technique to characterize crystalline materials. X-ray diffraction measurements are usually carried out on a diffractometer using Cu-K $\alpha$  radiation ( $\lambda=1.54 \text{ \AA}$ ). The peak position, intensity, width and even shape in X-ray diffraction pattern data are directly related to crystalline structure of the material. Every crystal has its own unique characters and the X-ray diffraction pattern can be used as "fingerprint" to identify them. Once the crystalline material is identified, X-ray diffraction data can be used to determine its structure, i.e. atomic spacing and angle, how the atoms pack in a crystalline material.

X-ray diffraction can be applied not only in powder samples but also in crystalline film samples. Typically, the structure characterization of crystalline film sample is carried out by using X-ray powder diffraction. The used instrument for powder measurements is called powder diffractometer which is usually used in Bragg-Brentano geometry (Figure 2.7). Here, the X-ray beam hit the sample surface with an incident angle of  $\theta$ . The irradiated area is dependent on the incident angle  $\theta$  and X-ray beam divergence. The diffracted rays from the irradiated area leave the sample surface at a diffracted angle of  $2\theta$ , which is defined as the angle between incident X-ray beam and the detector. Afterwards, the irradiated rays reach the detector which records the intensity of received X-rays. The Bragg-Brentano geometry is ideal for absorbing materials i.e. metals, thin films and texture analysis. The incident angle  $\theta$  is always half of the detector angle  $2\theta$ . The diffractometers in Bragg-Brentano geometry are commonly operated in reflection configuration, which can be divided into Bragg-Brentano  $\theta$ - $\theta$  configuration and  $\theta$ - $2\theta$  configuration. In the  $\theta$ - $\theta$  configuration, the detected sample is fixed while the X-ray source and detector are rotated around it at a

speed of  $-\theta^\circ/\text{min}$  and  $\theta^\circ/\text{min}$ , respectively. Here, the angle between X-ray source and detector is always  $2\theta$ . In the  $\theta$ - $2\theta$  configuration, the X-ray source is fixed while the sample and X-ray detector are rotated at a speed of  $\theta^\circ/\text{min}$  and  $2\theta^\circ/\text{min}$ , respectively.

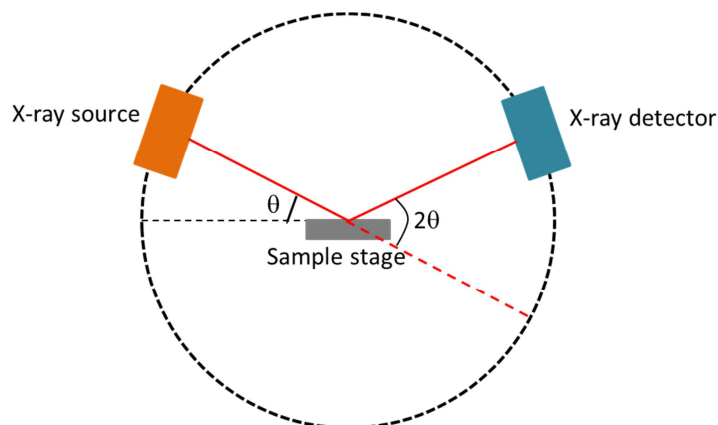


**Figure 2.7:** A conventional powder diffractometer in Bragg-Brentano geometry.

However, the X-ray diffraction measurements in conventional diffractometer using Bragg-Brentano geometry are usually carried out on point detectors, also called as zero-dimensional (0D) detector. Normally, the point detector only can observe a diffraction intensity each time at a single angle of  $2\theta$ . The diffraction intensity measurements at each  $2\theta$  position contribute one data point on the sample diffraction pattern. The measurement by using point detector is very slow and only the crystallites which are oriented properly in the sample can be detected and contribute to the observed diffraction pattern [130]. When the sample is moved and loaded in another orientation, the diffraction peak maybe cannot be measured any more. To some extent, the X-ray diffraction measurements using point detector is an inefficient measurement technique.

Area detector or two-dimensional (2D) detector is introduced afterwards which contains a two-dimensional array of detection elements. These detection elements are called as pixels. The 2D detector can be used to simultaneously measure the two-dimensional distribution of many diffracted X-rays. Thereby it will save the measuring time in the experiment. One of the widely used 2D X-ray detectors is called as image plate detector. In my thesis, the Mar 345 image plate detector was used (Figure 2.8a) and the working principle of image plate is shown in Figure 2.8b. Here, the image plate has a photo-stimulable phosphor, usually  $\text{BaF}(\text{Br},\text{I}):\text{Eu}^{2+}$  which can store X-rays in in a broad energy range (5 keV to 100 keV) by exciting electrons from valence band into conduction band. When simulated by red laser from a diode laser scanner with a wavelength of about 630 nm, the electrons will return to the ground state while emitting luminescence (390 nm). The emitted photos of 390 nm are counted by a



photomultiplier and their quantity is proportional to the amount of absorbed X-ray photos. After scanning the strong visible light will be switched on to erase any residual X-ray signals on the image plate. Image plate detectors are very sensitive and even very low levels of X-ray photos can be detected.

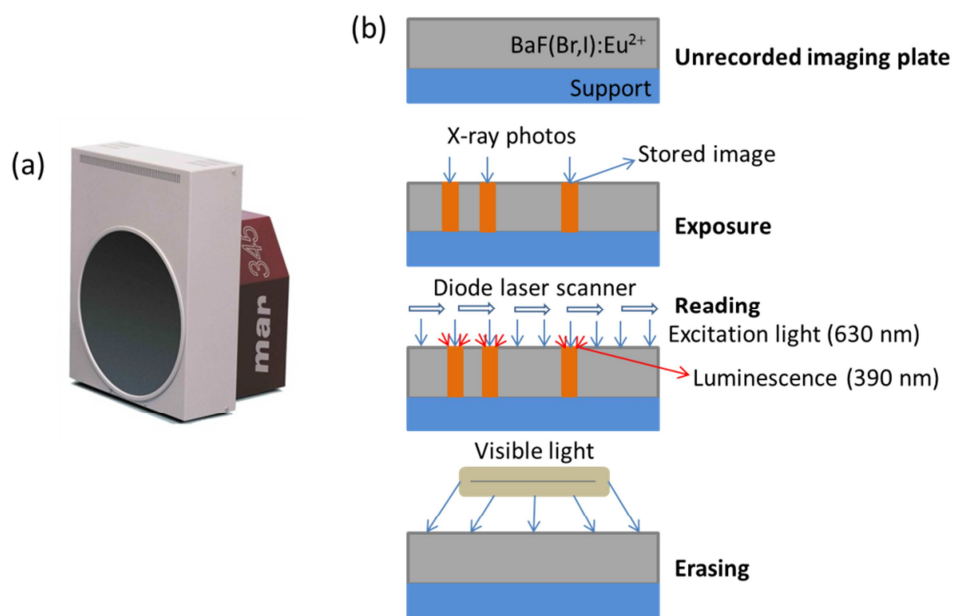


**Figure 2.8:** (a) Mar 345 image plate detector (from [www.marxperts.com](http://www.marxperts.com)). (b) The working principle of image plate detector in X-ray diffraction measurements.

The Mar345 image plate detector is an excellent detector because of its short data read-out time (down to 34 s for a 180 mm diameter scan) and good data quality (Figure 2.9). The Mar345 plate detector has a huge active area of 345 mm diameter which is read out by driving a reading head over a spinning plate yielding spiral raw data. Here, the diffracted X-ray photos are recorded simultaneously in a two-dimensional range. The sample-detector distance is variable and shorter distance can increase the recorded data quality. The diameter of image plate is 345 mm which has better resolution than smaller diameters (i.e. 180 mm, 240 mm or 300 mm). When the observed reflections are close to each other, a pixel size of 150  $\mu\text{m}$  is used for better resolution. The total time which includes read-out time and erasing time is around 86 seconds.

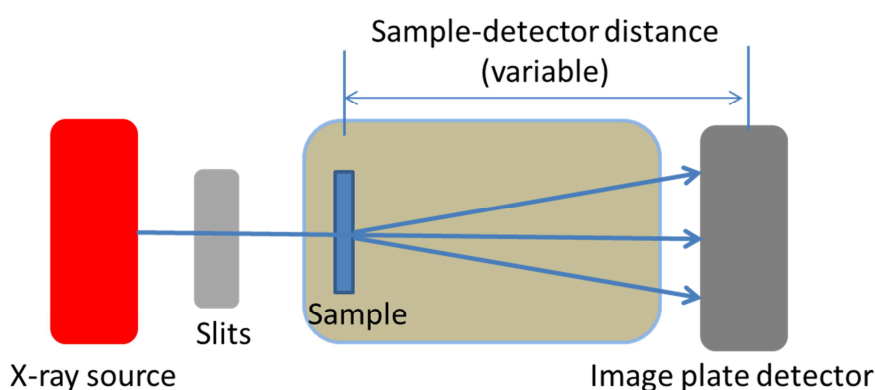


**Figure 2.9:** Sketch of X-ray diffraction measurements using image plate detectors.

The crystallites have preferred orientations in the solid films and a two-dimensional diffraction pattern measurement have the potential for consistent crystallinity measurements (Figure 2.10). The two-dimensional X-ray diffraction pattern consists of scattering intensity distribution as a function of two orthogonal angles. One is the Bragg angle  $2\theta$  and the other is the azimuthal angle about the incident X-ray beam which is denoted by  $\gamma$ . The two-dimensional diffraction pattern (Figure 2.10a) can be analyzed or by data reduction to the intensity distribution along  $2\theta$  or  $\gamma$ . For example, the  $\gamma$ -integration method can reduce a two-dimensional diffraction pattern into a diffraction profile which is the diffraction intensity as a function of diffraction angles  $2\theta$  (Figure 2.10b). As shown in Figure 2.10b, the  $\text{CH}_3\text{NH}_3\text{PbI}_3$  perovskite film exhibits reflections with  $2\theta$  angles of  $14.38^\circ$ ,  $20.27^\circ$ ,  $23.80^\circ$  and  $24.77^\circ$ , which are assigned to the (110), (200), (211) and (202) planes of the tetragonal perovskite structure. The reflection intensities of tetragonal perovskite structure show some difference because the intensity of the Bragg reflections falls off with the increasing of Bragg angle  $2\theta$ . Therefore, the (110) reflection has stronger intensity than (220) reflection, which indicates (110) plane is the dominant crystal plane. Furthermore, X-ray diffraction patterns can be performed in-situ which allows real time study of the evolution of diffraction patterns. The big advantage of in-situ X-ray diffraction is its ability to directly observe the reactions or phase transitions.

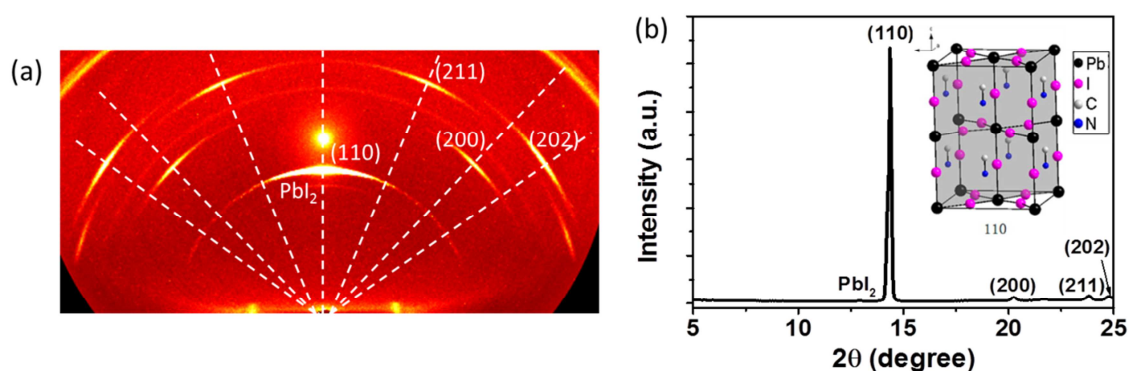


**Figure 2.10:** (a) Two-dimensional X-ray diffraction of  $\text{CH}_3\text{NH}_3\text{PbI}_3$  perovskite film onto PEDOT:PSS coated indium tin oxide (ITO) substrate, the dashed lines through reflections indicates perovskite crystallites. (b) The diffraction profile integrated over the area under the dashed lines, inset: (110) crystallographic planes (in gray) for tetragonal  $\text{CH}_3\text{NH}_3\text{PbI}_3$  structure [131].

## 2.4 Matrix-assisted laser desorption/ionization time-of-flight mass spectrometry (MALDI-TOF MS)

MALDI-TOF MS is the abbreviation for “Matrix-Assisted Laser Desorption/Ionization-Time of Flight mass spectrometry”. This soft ionization technique has been widely used in mass spectrometry, because the minimal fragmentation produced which allows the identification of quasi-molecular ions of the intact analytes. During MALDI ionization process, a molecule is transferred into an ion by acquiring a positive or negative charge with the collaborated functions of laser and selected matrix. MALDI-TOF MS technique is a three-step processes as described in Figure 2.11.

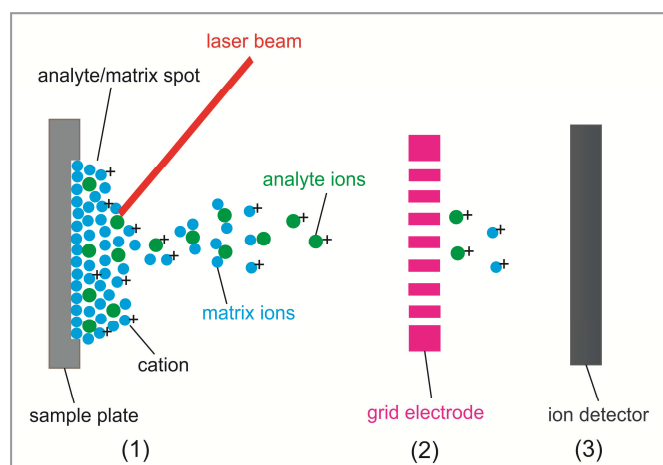


**Figure 2.11:** The working principle diagram of MALDI-TOF MS technique.

At the first step, a small amount of analyzed sample (A) is mixed with a large quantity of suitable matrix (M) and applied on a metal MALDI plate. The matrix absorbs the laser energy and then the matrix is desorbed and ionized. At this stage, many species are formed including neutral and ionized matrix molecules  $M^*$ , protonated  $M+H^+$  and deprotonated  $M-H^-$  matrix molecules. In positive ionization mode,  $M+H^+$  ions are usually the dominant species, while  $M-H^-$  ions are usually the most abundant species in negative ionization mode. When the matrix molecules are desorbed and ionized, the analyte molecules are ionized by electron and/or proton transferred from matrix.

At the second step, the ionized analyte molecules (analyte ions) are accelerated through an electric field and reach the grid electrode (Figure 2.11). As described in Equation 2.3, all ions including analyte ions and matrix ions obtain identical initial kinetic energy from this accelerating procedure.

$$E = qU = zeU = \frac{1}{2}mv^2 \quad (\text{Equation 2.3})$$

At the third step, the charged ions with various mass-charge ratios ( $m/z$ ) fly at a constant but different velocity towards the ion detector. Since the length of the flight tube  $L$  and the accelerated voltage  $U$  are constant for all ions, thus the ions with smaller  $m/z$  (higher velocity) has shorter flight time  $t$  and ions with large  $m/z$  values (lower velocity) experience longer flight time  $t$  (Equation 2.4). Therefore, the flight time of ions  $t$  correlates well to their mass-to-charge ( $m/z$ ) values, and the ions with different  $m/z$  ratios can be identified by using MALDI-TOF MS technique.

$$\frac{m}{z} = \frac{2eU}{L^2}t^2 \quad (\text{Equation 2.4})$$

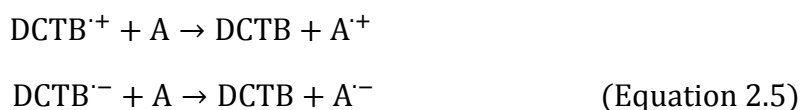
Here,  $m$  is the weight of an ion,  $z$  is its corresponding charge state,  $U$  is the accelerated voltage,  $L$  is the flight path length of ions,  $t$  is the flight time of an ion;  $e$  is elementary charge.

There are two charged modes in MALDI-TOF MS measurements, positive and negative ionization mode. The application of positive or negative charge mode mostly depends on the functional groups of the sample. If the analyzed molecule has functional groups which prefer to accept a proton ( $H^+$ ) or lose an electron then positive mode is used to detect analyzed sample ions. While negative ion detection mode is used if the analyzed sample has functional groups that readily lose a proton or obtain an electron. However, the exact ionization mechanism is still under debate.

As excellent and successful candidates for electron acceptor materials, [6,6]-phenyl- $C_{61}$ -butyric acid methyl ester (PCBM) (Figure 2.12) and its derivatives have been studied widely in organic and polymer solar cells. Thereby it is important to investigate

the degradation pathways of PCBM molecules under detrimental environments (i.e. under ambient or irradiation). Among kinds of various characterization techniques, MALDI-TOF MS is a powerful technique to detect the mass changes of PCBM molecules during the degradation process. As shown in Figure 2.12, PCBM consists of one methyl ester group which may show affinity to proton, which means a positive ion of  $[\text{PCBM}]^+$  can be detected. Additionally, PCBM also contains a bulky conjugated structure which prefers to form radical ions (cations and anions) [132]. Because of the  $\text{C}_{60}$  fullerene structure, PCBM is an electron deficient compound which can easily take up one electron and become negative ions of  $[\text{PCBM}]^-$ , which allows ions detection using negative MALDI-TOF MS mode.

The choice of a suitable matrix (M) is the first key step for a reliable MALDI-TOF MS spectrum. A perfect matrix should contain the following properties: (1) can absorb the laser wavelength of usually 237 nm; (2) can embed and isolate analytical sample (i.e. by co-crystallization); (3) should be stable under vacuum condition; (4) can induce co-desorption of the analytical sample under laser irradiation; (5) can promote the ionization of analytical sample. Here, The matrix trans-2-[3-(4-tert-Butylphenyl)-2-methyl-2-propenylidene] malononitrile (DCTB) (Figure 2.12) was chosen as the matrix for PCBM characterization using MALDI-TOF MS. One reason is that the MALDI-TOF MS was carried out on a Reflex II instrument with a UV laser of wavelength 337 nm, DCTB has a good absorption at 337 nm with a strong absorption property of  $> 2000$  (mol. absorption). This property enables the DCTB matrix molecules to absorb laser flux rapidly and efficiently. The other reason is that DCTB has been proven to be a suitable matrix material for the MALDI-TOF MS analysis of fullerenes and their derivatives [133]. DCTB matrix can promote the formation of analyte molecules ions at low laser fluencies. The analyte ions can be formed according to the reactions in Equation 2.5. Here A indicates the analyte molecules. The positive and negative analyte ions are formed by proton and electron transfers, respectively.



By using DCTB, the unwanted decomposition can be minimized while persisting good efficiency of desorption and ion formation of the analyte molecules [133]. As shown in Figure 2.12, DCTB matrix shows a signal centered at  $m/z$  250 and 500 are attributed to  $[\text{DCTB}]^+$  and  $[\text{DCTB}]^+$  dimer, respectively. The MALDI-TOF MS in positive mode of PCBM molecule in Figure 2.12d shows signal located at  $m/z$  909 which is assigned to the  $[\text{PCBM}]^+$  positive ions. Furthermore, the  $m/z$  signals of pure DCTB below 500 are mostly contributed to the matrix clusters [134]. Minimal fragmentation of PCBM

molecules could be observed at suitable lower laser energy. Thereby MALDI-TOF MS is an efficient approach for the detection of fragment ions which is related to the molecule structure of PCBM materials.

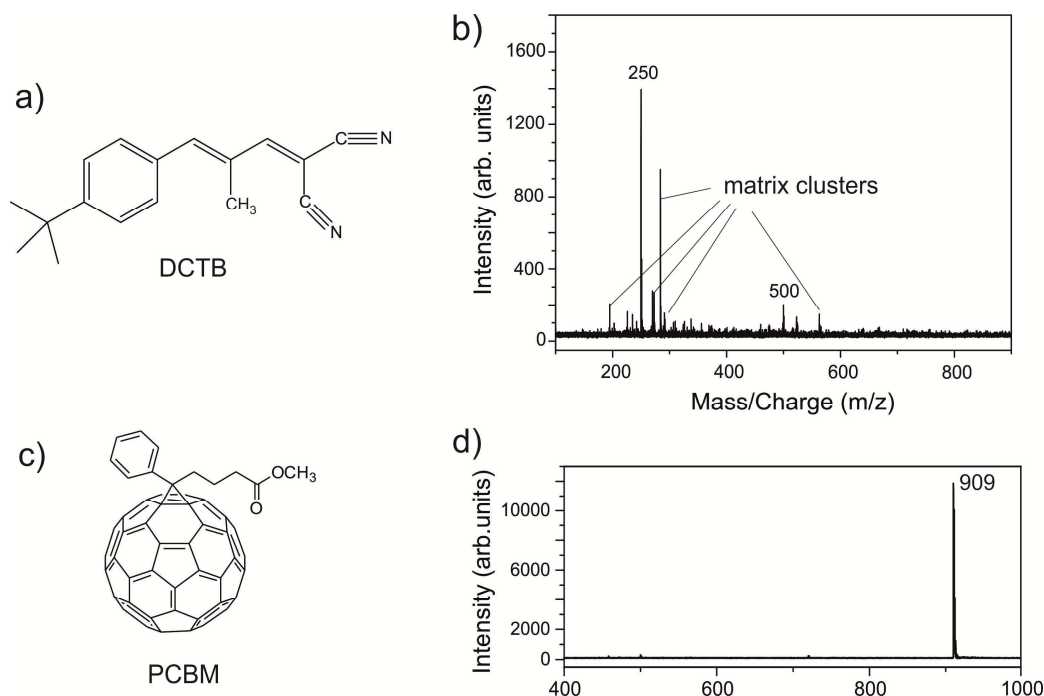


**Figure 2.12:** Molecular structures of DCTB (a) and PCBM (c) materials, and the MALDI-TOF mass spectrum of DCTB (b) and pristine PCBM film (d) in positive mode.

## 2.5 X-ray photoelectron spectroscopy (XPS)

XPS is a widely applied surface sensitive technique to measure the elemental composition and electronic state of the surface. In XPS, the energy of X-ray beam  $h\nu$  is absorbed by atoms (A) in sample surface, leading to ionization and emission of core electrons ( $A^+$ ). Then the kinetic energy and number of photoelectrons in the sample surface are being analyzed and a photoelectron spectrum is obtained. The kinetic energy of the emitted photoelectrons KE can be expressed using Equation 2.6:

$$KE = h\nu - (E_{A^+} - E_A) \quad (\text{Equation 2.6})$$

Here,  $h\nu$  is the excitation energy,  $(E_{A^+} - E_A)$  is the energy difference between ionized atom  $A^+$  and neutral atom A, also called as binding energy of electron (BE). Furthermore, the binding energies (BE) of energy levels in solids are conventionally measured regarding Fermi-level rather than the vacuum level. This introduces a small correction to the Equation 2.6 to account for the work function ( $\phi$ ) of solid. Therefore,

the above equation is rearranged to the following expression, where  $\phi$  is the work function of the analyzed sample:

$$KE = h\nu - (E_{A^+} - E_A) - \phi = h\nu - BE - \phi \quad (\text{Equation 2.7})$$

Typically, XPS experiment contains three parts as shown in Figure 2.13a. The first part is one fixed-energy X-ray radiation. The commonly used X-ray sources are Magnesium (Mg) K $\alpha$  radiation with energy of 1253.6 eV and Aluminum (Al) K $\alpha$  with energy of 1486.6 eV. The second part is an ultrahigh vacuum (UHV) chamber with pressure  $< 10^{-9}$  millibar in order to analyze emitted photoelectrons without interference from gas phase collisions. The third part is an electron energy detector to enable the emitted photoelectrons to be analyzed according to their kinetic energy (KE). An XPS spectrum plots the number of detected electrons versus their binding energy. Figure 2.13b shows a XPS spectrum of the top surface of methylammonium lead iodide (CH<sub>3</sub>NH<sub>3</sub>PbI<sub>3</sub>) perovskite solid film using Mg K $\alpha$  radiation. The XPS spectrum indicates a binding energy due to the emission from 1s levels of C and N atoms at 285 eV and 402 eV. The emission from 4f levels of Pb atom gives rise to peaks at 138 eV and 143 eV. The peak at 619 eV and 630 eV are due to emission from 3d levels of I atom. The XPS spectrum also indicates the surface elemental composition N: Pb: I with intensity ratio of 0.8:1:3.2 which is very close to the ideal CH<sub>3</sub>NH<sub>3</sub>PbI<sub>3</sub> (1:1:3).

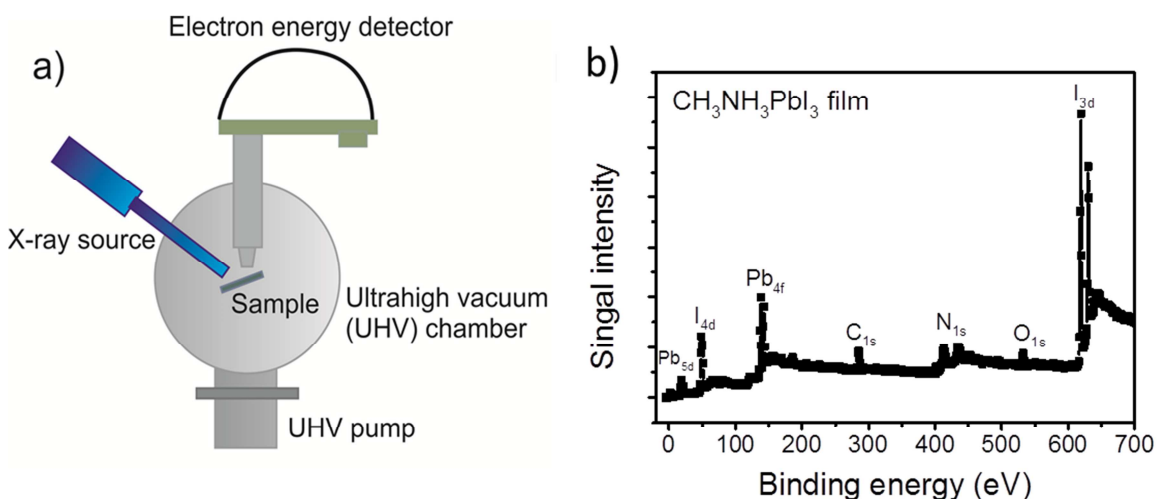


**Figure 2.13:** (a) Schematic diagram of a XPS setup and (b) XPS spectrum of CH<sub>3</sub>NH<sub>3</sub>PbI<sub>3</sub> perovskite film on top of PEDOT:PSS/ITO substrate

XPS is a surface chemical analysis technique which allows analyzing the surface chemistry of a sample from top 0 to 10 nm in depth. In order to quantitatively characterize the elemental and chemical information in the bulk perovskite solar cells, it would be useful to intentionally expose deeper layers of perovskite sample using depth-profiling XPS [135]. Depth-profiling XPS is performed by progressively removing

the materials from the surface and measured XPS at each step. At the beginning of removing sample materials, a XPS spectrum is measured from sample surface. An ion beam is then used to etch the sample surface over a square or rectangular area. After the etch step, the ion beam is blanked and another XPS spectrum is observed. The etching and recording steps are repeated until the profiling processes proceed to the required depth. Afterwards, all the recorded spectra from a required region are displayed in one graph which shows the trend of peak intensity and position. The XPS depth profile of an analyte sample is plotted using the sputtering time or profiling depth on the x-axis and the signal intensity or atomic concentration on the y-axis, which allows the comparison of the trends in different atoms in the sample. The depth profiling process may affect by the sample roughness, because the surface roughness is persisted during the profiling process. Therefore, an ideal sample for depth-profiling process is the sample which has a smooth and well-polished surface.

The schematic of depth-profiling XPS (Figure 2.14a) and in-depth distribution of the atomic species percentage (Pb and I atoms) are displayed as a function of sputtering time (Figure 2.14b). The Pb:I ratio is about 1:2.4 at the top of perovskite film (sputter time  $\sim 300$  s), which is lower than the theoretical value of 3. This phenomenon implies the possible presence of “free” iodine and precursor elements (i.e.  $\text{PbI}$ ,  $\text{PbI}_2$ ) are not completely converted into  $\text{CH}_3\text{NH}_3\text{PbI}_3$  perovskite material [135]. Therefore, depth-profiling XPS analysis is an important characterization technique which provides quantified information of the analyte sample.

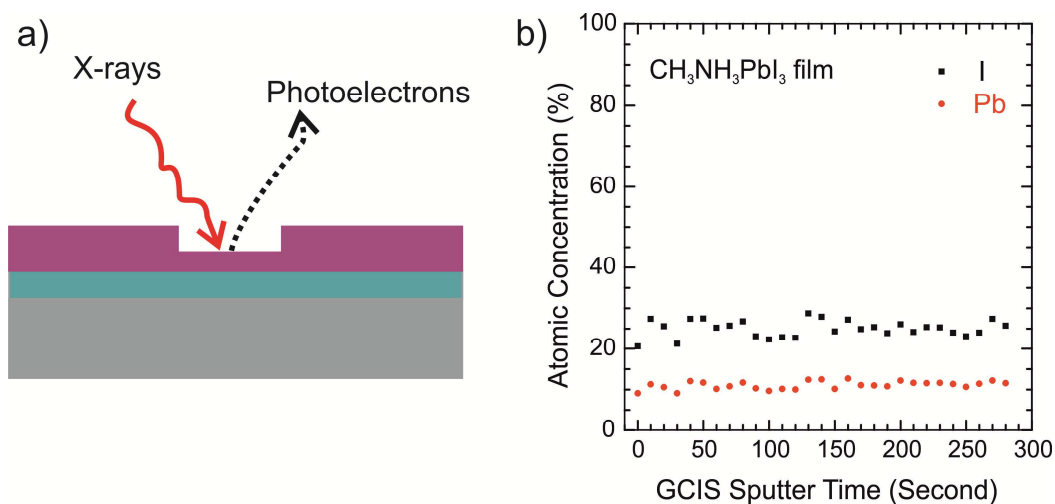


**Figure 2.14:** (a) Schematic of depth-profiling XPS measurements and (b) XPS depth profile of  $\text{CH}_3\text{NH}_3\text{PbI}_3$  perovskite film coated on PEDOT:PSS/ITO substrate.



## 2.6 Experimental setup

### 2.6.1 Substrates preparation

The ITO substrates were purchased from Präzisions Glas & Optik GmbH with a square resistance  $\leq 20$  Ohms/sq. The ITO substrates were 1.5 cm  $\times$  1.5 cm squares and were subsequently cleaned with 2% Hellmanex II, acetone and isopropanol by using a ultrasonic cleaner. After drying with an air gun, the ITO substrates were further cleaned for 10 or 20 min in an argon plasma cleaner (PDC-002, Harrick Plasma, Ithaca, NY 14850, USA). In order to protect the cleaned ITO substrates from contamination, they were stored in glass petri dish and transported into a N<sub>2</sub>-filled glovebox for usage.

### 2.6.2 Spin coating technique

Spin coating is a procedure used to deposit uniform thin films onto certain flat substrates [136, 137]. Usually the used substrate is mounted onto a rotor, and a small amount of sample solution is dropped onto the substrates. Afterwards, the substrate is rotated by applying a certain spinning speed for a certain time to spread the sample solution. In the end a flat film is formed. The machine for spin coating is usually called as spin coater. The film thickness can be controlled by changing the experimental parameters, such as spin-coating speed, time and the concentration of sample solution [137].

### 2.6.3 SFM cantilever cleaning

Silicon cantilevers (Olympus OMCL-AC160TS-W2) with a nominal resonance frequency 300 kHz, spring constant  $k = 42$  N/m and tip radius  $R < 5$  nm are employed. The cantilevers were put on a glass coverslip and cleaned in the Argon plasma (Plasma Cleaner/Sterilizer PDC-002, 200W, Harrick Scientific Corp., United States) for 30 s at a pressure of approximately 1.6 mbar prior to each experiment. The SFM data were flattened and analyzed using Gwyddion Software ([www.gwyddion.net](http://www.gwyddion.net)).

### 2.6.4 In-situ SFM measurements

The scanning force microscopy measurements were performed with an EnviroScope scanning force microscopy (Bruker, Santa Barbara, USA) in intermittent contact mode. The EnviroScope AFM combines with an environmental control and a hermetically sealed sample chamber. The chamber was flushed with different atmospheric gases during the measurements in order to obtain a comparable atmosphere as real

perovskite film preparation. EnviroScope SFM setup is equipped with a sample heater stage controlled by a commercial temperature controller (Lakeshore 331), which has an accuracy of 0.1 K and a maximum temperature of 458 K.

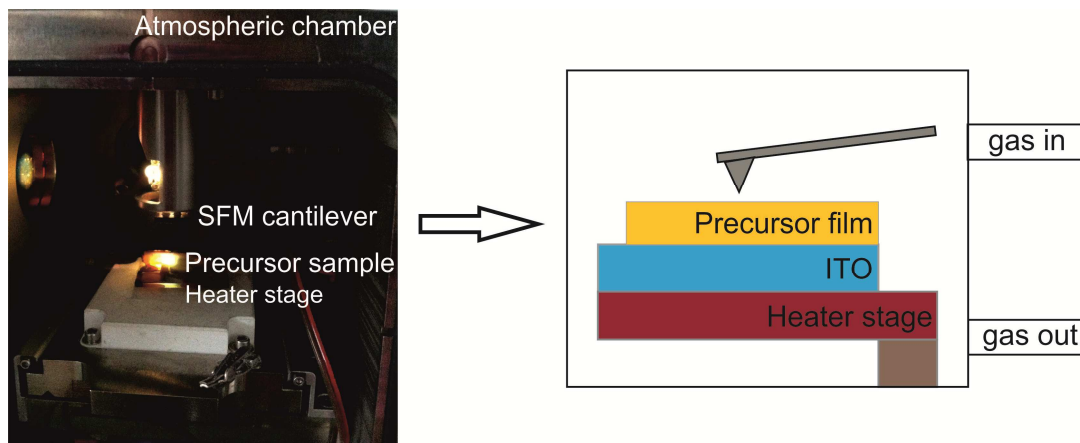


**Figure 2.15:** Experimental setup of in-situ thermal annealing experiments.

### 2.6.5 UV-vis absorption spectroscopy

The UV-visible absorption of  $\text{CH}_3\text{NH}_3\text{PbI}_3$  films was acquired on a Perkin-Elmer Lambda 900 spectrophotometer at room temperature. The PEDOT:PSS coated ITO substrate was used to measure the background spectrum.

### 2.6.6 In-situ SFM measurements under humidity

The in-situ scanning force microscopy measurements of the perovskite films were carried out on a EnviroScope SFM (Bruker, Santa Barbara, USA) and a MultiMode scanning force microscope using a standard liquid cell (Bruker, Santa Barbara, USA). The humidity level of the measurement chamber (20%, 50% and 80%) was adjusted using two flow controllers: the flow of a carrier gas (dry  $\text{N}_2$ ) and  $\text{N}_2$  saturated water vapor at room temperature were controlled and then mixed. A humidity sensor is located closely to the sample holder to precisely monitoring the humidity level of sample chamber. The precise humidity values were measured during the experiments using in house-made humidity sensor. The humidity 0% experiment was performed with a MFP-3D scanning force microscopy (Asylum Research, Santa Barbara, USA) in a glass glovebox (typeP10R180T2, GS Glovebox Systemtechnik GmbH) filled with dry  $\text{N}_2$  at room temperature. All SFM images were recorded in tapping mode and the same position was kept during the entire experiment.

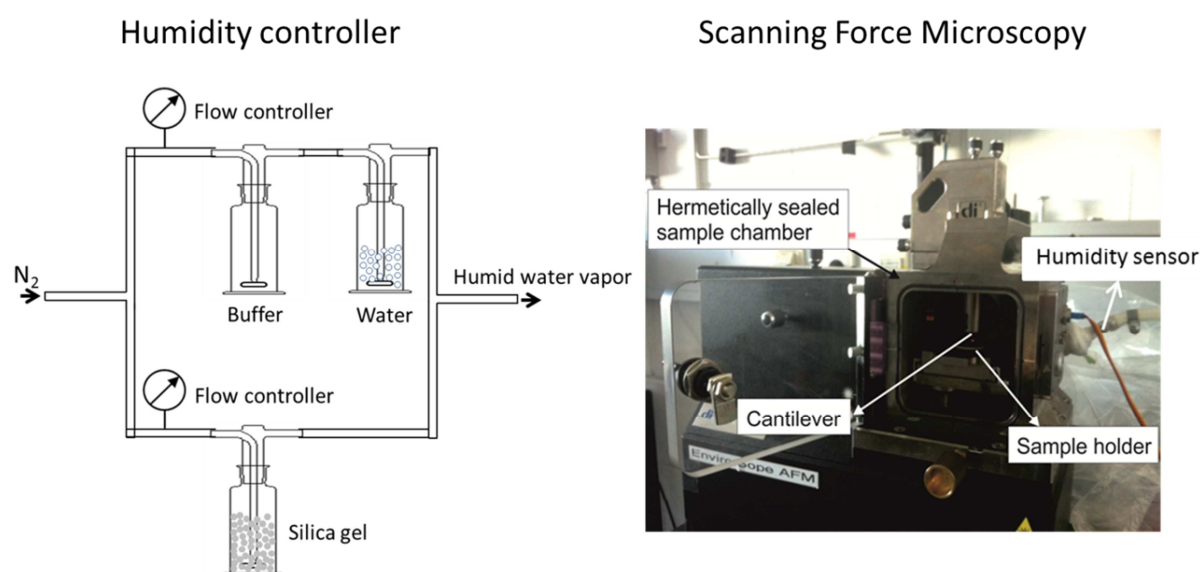


**Figure 2.16:** Schematic of the humidity controlled in-situ EnviroScope Scanning Force Microscopy (SFM) measurements.

### 2.6.7 X-ray diffraction measurements

The ex-situ X-ray diffraction (XRD) patterns were measured on a Philips powder diffractometer PW1810 in Bragg Brantano geometry using  $Cu-K\alpha$  radiation ( $\lambda=1.54 \text{ \AA}$ ).

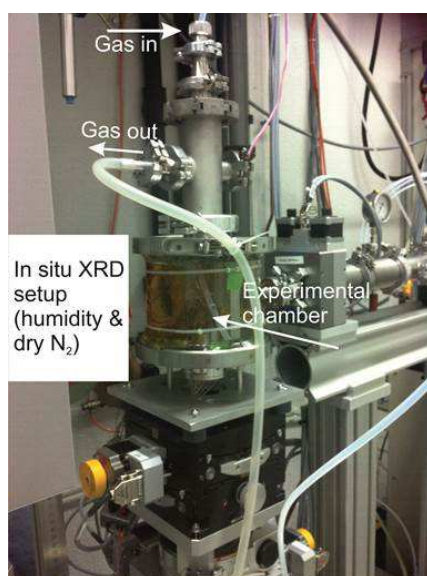


**Figure 2.17:** During an in-situ XRD experiment, the  $CH_3NH_3PbI_3$  perovskite film was kept inside an atmospheric chamber where the humidity can be controlled. This setup is kept in front of the X-ray detector.

The in-situ X-ray diffraction was performed on a 6-circle diffractometer using a Cu-K $\alpha$  radiation (Rigaku MicroMax 007 X-ray generator, Osmic Confocal Max-Flux curved multilayer optics). The sample was mounted in reflection geometry at an incident angle of 2.0° on a 6-circle diffractometer. 2D diffraction patterns were recorded every 15 min by an image plate detector (Mar345, 150  $\mu$ m pixel size) at a sample-detector distance of 34.92 mm. The whole setup of in-situ X-ray diffraction is shown in Figure 4.2.

### 2.6.8 X-ray photoelectron spectroscopy (XPS)

XPS measurement was conducted on a Kratos Axis Ultra<sup>DLD</sup> spectrometer (Kratos, Manchester, England) using an Al K $\alpha$  excitation source with a photon energy of 1487 eV. Depth profiling of the samples was generated in cycles where each XPS spectra was collected after exposing the sample center by the gas cluster ion source (GCIS) for 10 seconds. Within this process, the atomic composition in target sample was profiled with respect to perpendicular depth. For the given purpose, the sample probing depth was approximately ~ 30 nm in the profiling process, the GCIS sputter source was set to 5 keV Ar<sub>500</sub><sup>+</sup> with a raster size of 1.5 mm  $\times$  1.5 mm, while the spectra were collected in small spot mode (~ 110 mm<sup>2</sup>) using a 0° take-off angle, defined as the angle between the surface normal and the axis of the analyzer lens. To avoid surface charging, the charge neutralizer was always used during spectra collection (filament current 1.6 Å, charge balance 2 V, and filament bias 1.3 V). The analyzer pass energy was set to 80 eV for composition analysis. For spectra analysis, a linear background was subtracted for all peak quantifications. The peak areas were normalized by the manufacturer supplied sensitivity factors and atomic concentrations were calculated using the Kratos Vision software.

### 2.6.9 MALDI-TOF MS measurements

Matrix-assisted laser desorption/ionization time of flight mass spectrometry (MALDI-TOF MS) was used to investigate any possible photo-degradation products of PCBM because of its high sensitivity and accuracy. As matrix we used trans-2-[3-(4-tert-Butylphenyl)-2-methyl-2-propenylidene]malononitrile (DCTB, Sigma-Aldrich,  $\geq$  98%) which was previously shown to enable a very soft desorption and ionization process for labile molecules and to provide very good results in the negative as well as the positive MALDI-TOF MS mode [34]. A sharp knife was used to scratch degraded PCBM films from ITO substrates. The analyte was submitted to solvent free sample preparation for MALDI by mixing it with DCTB matrix in a ratio of 50:1 by weight in a ball mill for 1 hour. Then the mixture was deposited on a thoroughly cleaned stainless

steel sample holder from Bruker. MALDI-TOF MS was carried out on a Reflex II instrument from Bruker by using a 337 nm nitrogen laser. All samples were analyzed in both positive and negative ion mode.



# Chapter 3

## Thermal crystallization and decomposition of CH<sub>3</sub>NH<sub>3</sub>PbI<sub>3</sub> films

### 3.1 Introduction

One of the critical factors of solution-processed perovskite solar cells is the morphology quality of perovskite films which is highly related to their power conversion efficiency [82-87]. Therefore, the film morphology should be well controlled during the device processing. It is necessary to apply thermal or solvent annealing treatment to transform precursor films into perovskite films. It has been demonstrated that the annealing protocol and atmospheres play an important role in preparing high quality perovskite films. Thus numbers of strategies have been reported to prepare high quality perovskite films, such as precursor modification [89, 90, 98, 99, 138], deposition techniques [91] [139], varied annealing atmospheres (in air, vacuum or moisture) [79, 86, 93-95]. By optimizing the processing conditions, the efficiency of planar perovskite solar cells have been improved significantly [77-80]. The previous studies showed that the planar perovskite solar cell with an efficiency above 10% exhibited extremely uniform flat films [126, 139, 140]. This phenomenon indicates that perovskite films built in a planar heterojunction structure can result in high power conversion efficiency, but its efficiency is strongly dependent on the nature of perovskite films. Additionally, the reproducible production of smooth and uniform perovskite films is crucial for the performance of perovskite devices.

Methylammonium iodide (CH<sub>3</sub>NH<sub>3</sub>I) and lead iodide (PbI<sub>2</sub>) are the two common components called as precursor materials which are used in the synthesis process of perovskite materials (methylammonium lead iodide, CH<sub>3</sub>NH<sub>3</sub>PbI<sub>3</sub>). To address the formation and crystallization process of CH<sub>3</sub>NH<sub>3</sub>PbI<sub>3</sub> materials, and also the possible involved phases at the processing conditions, in-situ heating experiments were designed under a controlled environment. Here, I prepared the perovskite precursor films by depositing a 1:3 molar ratio solution of PbI<sub>2</sub> and CH<sub>3</sub>NH<sub>3</sub>I precursor materials mixed in dimethylformamide (DMF) onto PEDOT:PSS coated ITO substrates. These precursor films are subsequently thermal annealed at 100 °C for a certain time

resulting in the formation of perovskite films. I realized this by transferring the precursor films into the sample chamber of EnviroScope SFM with well controlled atmospheres. Here, I focused on the effect of the annealing temperature and the atmosphere during the crystallization transformation process, which is related to the morphology of perovskite films. The crystallization processes were analyzed by using in-situ SFM method which could track morphology evolution during annealing process. The aim of this study is to better understand the role of annealing temperature & protocol & atmosphere on the film morphology and crystallization.

## **3.2 Experimental section**

### **Film preparation**

The PEDOT:PSS (Sigma Aldrich) was spin-coated on top of pre-cleaned ITO substrates at a speed of 2500 rpm for 5 s and 5000 rpm for 25 s, then dried in the air at 120 °C for 60 min. Afterwards, the PEDOT:PSS coated ITO substrates were transferred into a N<sub>2</sub>-filled glovebox.

Methylammonium iodide (CH<sub>3</sub>NH<sub>3</sub>I) was synthesized using the method from Lee et al. [72]. Lead chloride (PbCl<sub>2</sub>, Sigma Aldrich, 99,999%) was carefully dehydrated under high vacuum conditions and nitrogen atmosphere at 60 °C. The perovskite precursor solution was prepared by mixing CH<sub>3</sub>NH<sub>3</sub>I (1.0 g) and PbCl<sub>2</sub> (582 mg) in 2.505 ml anhydrous N,N-dimethylformamide (DMF, Sigma Aldrich) with a molar ratio of 3:1 at 60 °C and stirred overnight in N<sub>2</sub>-filled glovebox. The precursor solution was passed through a 0.45 μm filter before usage and deposited onto PEDOT:PSS by spin-coating at 2000 rpm for 60 s. After resting for 10 min to allow solvent evaporation, the precursor films were transported out of glovebox by protecting it with a Parafilm (Bemis Company) to protect precursor films from air and humidity exposure. Afterwards, the precursor films were built into a SFM experimental chamber with a controlled atmosphere.



### 3.3 Results and discussion

#### 3.3.1 Under $\text{N}_2$ atmosphere

##### In-situ SFM

The fabrication of  $\text{CH}_3\text{NH}_3\text{PbI}_3$ -based perovskite solar cells were usually recommended to be carried out in a controlled environment with a humidity level of below 1% [91]. After depositing the precursor solution, a subsequent thermal annealing treatment of the precursor is required to obtain perovskite films. In this case, the sample chamber of EnviroScope SFM was filled with dry  $\text{N}_2$  gas with a controlled humidity below 1% during in-situ annealing process. In Figure 3.1a, the precursor film which was not annealed showed smooth surface with a film surface roughness of root-mean-square (RMS) value of 29.7 nm in the measured area of around  $225 \mu\text{m}^2$ . However, some pinholes were present in the precursor films.

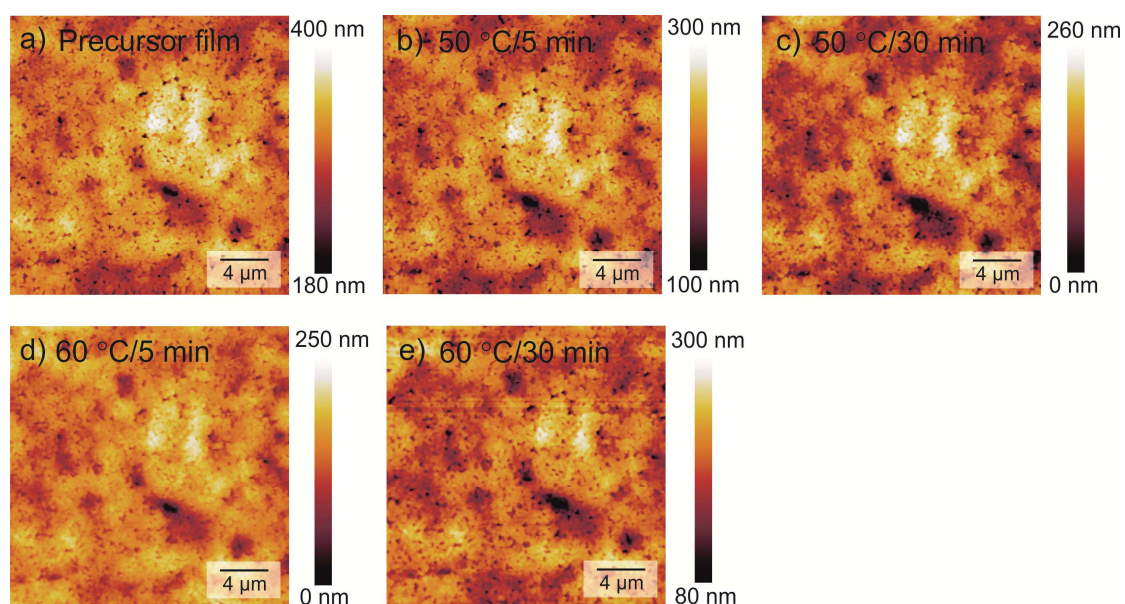


**Figure 3.1:** SFM images of precursor films deposited on PEDOT:PSS/ITO substrates annealed under  $\text{N}_2$  atmosphere at different stages (a) initial precursor film, (b) 50 °C for 5 min, (c) 50 °C for 30 min, (d) 60 °C for 5 min and (e) 60 °C for 30 min.

In the following, I would do step-by-step thermal annealing treatments on the precursor films. After annealed the film at each annealing temperature, the whole heating system would be cooled down to room temperature, SFM technique was then used to track the morphology changes which was always imaged on the same area. The precursor film did not indicate significant changes when continually increased thermal annealing at 60 °C even for 30 min (Figure 3.1b-e). The surface roughness of

precursor film annealed from 50 °C to annealing temperature of 60 °C for 30 min is 27.3 nm which is almost constant compared with the roughness of precursor film without any thermal annealing treatment 29.7 nm (Figure 3.1a).

As the annealing temperature was increased to 70 °C, there was a drastic change with additional species formed on top of the film surface even annealing for 5 min (Figure 3.2a). Additionally, the film surface roughness significantly increased from a RMS of 27.3 nm at 60 °C to 69.3 nm at 70 °C in a measured area of  $225 \mu\text{m}^2$  (Figure 3.3). The increase in surface roughness was mainly contributed to the additional formed species (indicated by black arrows in Figure 3.2a) during thermal annealing process. Furthermore, with progressively prolonging the annealing time from 5 min to 10 min at annealed temperature of 70 °C, the new formed species (indicated by black arrows in Figure 3.2a and b) evaporated or eliminated and some pores were formed afterwards (marked using solid circles in Figure 3.2b).

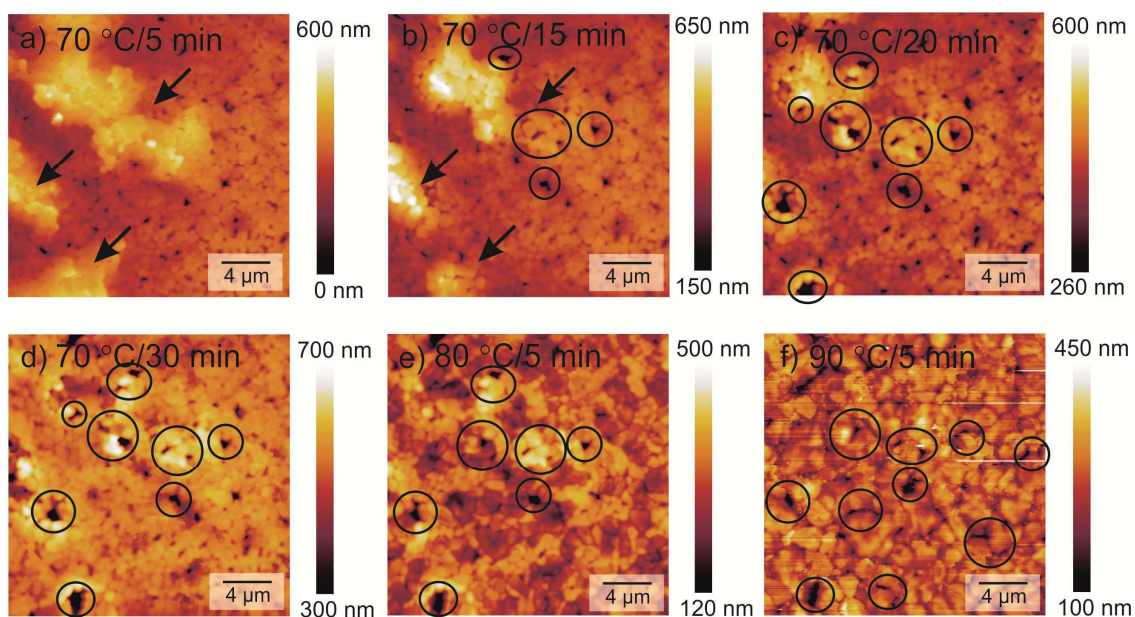


**Figure 3.2:** SFM images of precursor films deposited on PEDOT:PSS/ITO substrates annealed under  $\text{N}_2$  atmosphere at different stages (a) 70 °C for 5 min, (b) 70 °C for 15 min, (c) 70 °C for 20 min, (d) 70 °C for 30 min, (e) 80 °C for 5 min and (f) 90 °C for 5 min.

When continually heated films for 20 min, more new formed species disappeared and more pores were then observed (Figure 3.2c and d). The areas around the new formed pores started to crystallize accordingly. The possible reason is that, during the chemical reaction of precursor materials  $\text{PbCl}_2$  and  $\text{CH}_3\text{NH}_3\text{I}$ , a certain amount of byproduct was formed and slowly released or sublimated during annealing process. Xie et al. [86] performed XPS measurements which confirmed the chemical composition of the byproduct during reaction between  $\text{CH}_3\text{NH}_3\text{I}$  and  $\text{PbCl}_2$  precursor materials. Their

results showed that the release rate of  $\text{CH}_3\text{NH}_3\text{Cl}$  byproducts is an important factor for the pore formation in perovskite film. Moderately aggregation of  $\text{CH}_3\text{NH}_3\text{Cl}$  byproducts left small pores after thermal annealing treatment, and vacuum-assisted thermal annealing was considered as an effective approach for the preparation of perovskite films [86].

However, it is lack of direct observation of the release of  $\text{CH}_3\text{NH}_3\text{Cl}$  byproducts and the formation of small pores afterwards. In my experiments, the in-situ SFM measurements were performed during thermal annealing treatments. The new formed species (black arrows in Figure 3.2a and b) are assigned to the  $\text{CH}_3\text{NH}_3\text{Cl}$  byproducts and they disappeared with continuously thermal annealing. Afterwards, small pores were formed (solid circles in Figure 3.2b). With prolonging the annealing time to 20 min at 70 °C, most of the new formed  $\text{CH}_3\text{NH}_3\text{Cl}$  byproducts were released and more small pores formed accordingly (solid circles in Figure 3.2c). With the release of the  $\text{CH}_3\text{NH}_3\text{Cl}$  byproducts, film roughness decreased significantly (Figure 3.3). With continuously prolonging the annealing time to 30 min at 70 °C, the film roughness increased again which indicated the film crystallization (Figure 3.2d).

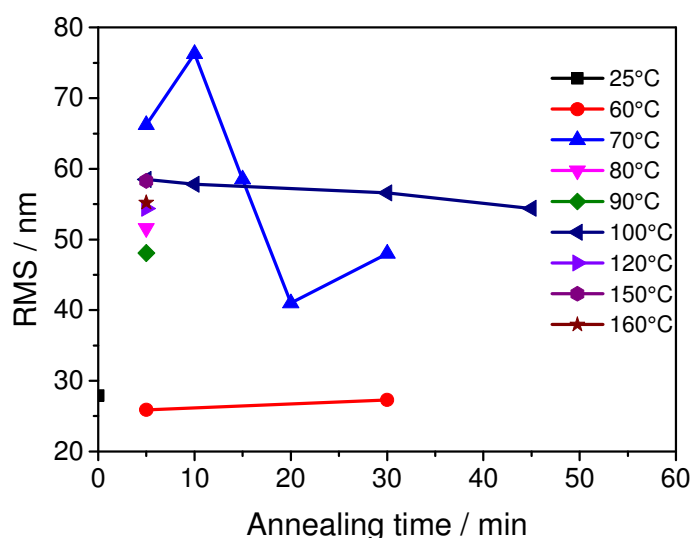


**Figure 3.3:** Root-mean-square (RMS) values of surface roughness of  $(\text{PbCl}_2+\text{CH}_3\text{NH}_3\text{I})$  films deposited on top of PEDOT:PSS/ITO substrates which were annealed under  $\text{N}_2$  atmosphere at different annealing temperatures and times.

The above findings revealed that the release or sublimation of these byproducts left space for the crystallization of perovskite structures and then induced the occurrence of film crystallization. When further performing thermal annealing at 80 °C for 5 min, the surface roughness of the film annealed at 80 °C for 5 min increased compared to the film annealed at 70 °C for 30 min (Figure 3.3), which indicated the crystallization of

film into big crystal structures (Figure 3.2e). Bigger crystal structures were visible upon thermal annealing at 90 °C even for 5 min (Figure 3.2f). The different distribution of small pores (solid circles in Figure 3.2f) might indicate the reorganization of crystal structure during thermal annealing process.

Further increasing thermal annealing temperature, the perovskite film formed bigger crystallized domains compared with the film annealed at 90 °C (Figure 3.4a – 3.4c). The crystallized domains preferred to form a closely dense structure and the films which were annealed at 100 °C for 5 min, 30 min and 45 min exhibited comparative morphologies (Figure 3.4a-c). Additionally, the films annealed at 100 °C at different annealing times showed almost constant surface roughness as shown in Figure 3.3. When further increasing the annealing temperature to 120 °C, small crystals were formed at the edge of each big crystallized domain (marked by black arrows in Figure 3.4d). This phenomenon indicates the possible decomposition of the big crystallized domains. Increasing the annealing temperature to 150 °C induced the significant decompositions of big crystallized domains which led to the formation of small crystals not only on the edge of big domains but the whole domains (Figure 3.4e). The small crystals persisted at an annealing temperature of 160 °C.

The above results indicate that the whole crystallized domains were progressively destroyed at high annealing temperature above 120 °C. Furthermore, the surface roughness of films annealed at 100 °C, 120 °C, 150 °C and 160 °C have comparative values as shown in Figure 3.3. This finding indicates that the perovskite crystallized domains decomposed into small crystals without structure reorganization. The above results showed that the annealing temperature during thermal annealing plays a vital role in the surface morphology of perovskite films. The annealing temperature should be under well controlled during the preparation process of perovskite films.



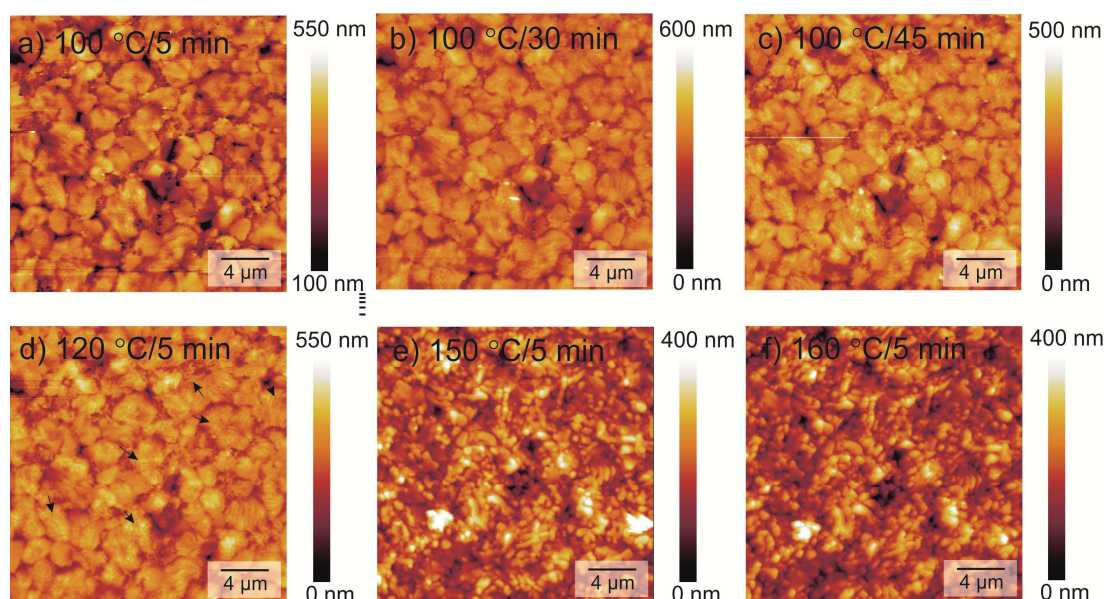


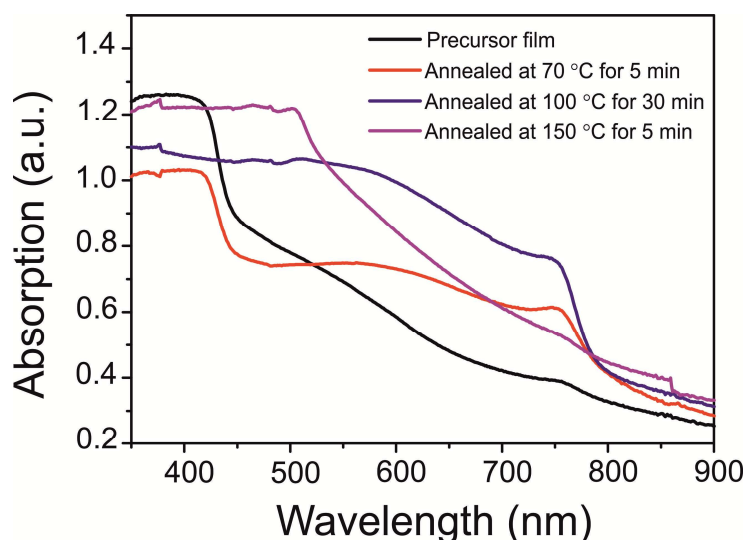
**Figure 3.4:** SFM images of precursor films deposited on PEDOT:PSS/ITO substrates annealed under  $\text{N}_2$  atmosphere at different stages (a) 100 °C for 5 min, (b) 100 °C for 30 min, (c) 100 °C for 45 min, (d) 120 °C for 5 min, (e) 150 °C for 5 min and (f) 160 °C for 5 min.

### UV-vis spectra

The UV-vis absorption spectra were used to study the chemical reactions during thermal annealing process at different annealing temperatures (Figure 3.5). The initial precursor film without any annealing treatment already showed the typical absorption spectrum of the perovskite films with a visible absorption peak at around 780 nm. When increasing the annealing temperature to 70 °C, the absorption peak at 780 nm and absorption spectrum across visible range became more significant. The in-situ SFM data also showed significant changes in film morphology. Combined these results, I could conclude that the  $\text{PbCl}_2 + \text{CH}_3\text{NH}_3\text{I}$  precursor materials started to react into  $\text{CH}_3\text{NH}_3\text{PbI}_3$  perovskite crystals at annealing temperature of 70 °C.

At an annealing temperature of 100 °C, an increase in the absorption across the entire spectrum was observed which indicated the fully conversion from precursor materials into perovskite crystals. Compared to the low absorbance of precursor films without thermal annealing treatment, the crystallization process required sufficient removal of the organic solvent from precursor film. Furthermore, thermal energy was also required to drive the conversion process from precursor materials to perovskite crystals. The absorption spectrum at an annealing temperature of 100 °C showed the best absorption across the entire spectral range. However, further increasing the annealing temperature to 150 °C led to a decrease in the absorption of perovskite

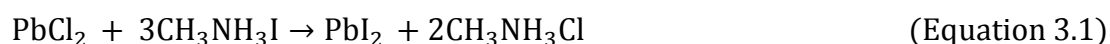
crystals, also resulted in additional absorption feature of  $\text{PbI}_2$  at 500 nm. This phenomenon confirmed the in-situ SFM data that the  $\text{CH}_3\text{NH}_3\text{PbI}_3$  perovskite crystals decomposed into  $\text{PbI}_2$  small crystals at higher annealing temperature. The formation of  $\text{PbI}_2$  became dominant at high annealing temperature with the disappearance of perovskite absorption onset at 780 nm.



**Figure 3.5:** UV-vis absorption spectra for films deposited on PEDOT:PSS/ITO substrates annealed under  $\text{N}_2$  atmosphere at different annealing temperatures.

### X-ray diffraction

In the following, the X-ray diffraction measurements were used to detect the crystal structure changes during annealing process (Figure 3.6). The X-ray diffraction data of precursor film without annealing treatment showed strong Bragg reflections at  $2\theta$  angles of  $19.84^\circ$ ,  $22.42^\circ$ ,  $25.08^\circ$  which were assigned to the precursor material  $\text{PbCl}_2$  [141]. Bragg reflections with  $2\theta$  angles of  $12.62^\circ$  and  $25.60^\circ$  were observed corresponding to the (001) and (002) lattice planes of crystalline  $\text{PbI}_2$  [91, 141-143]. The Bragg reflections at  $17.74^\circ$  and  $27.24^\circ$  confirmed the assumption of  $\text{CH}_3\text{NH}_3\text{Cl}$  in the precursor perovskite films [101]. These results implied that partial ion exchange occurred between Cl in  $\text{PbCl}_2$  and I in  $\text{CH}_3\text{NH}_3\text{I}$  even without annealing treatment. This finding is consistent with the previous study Wang et al. [144]. This process could be described as Equation 3.1:



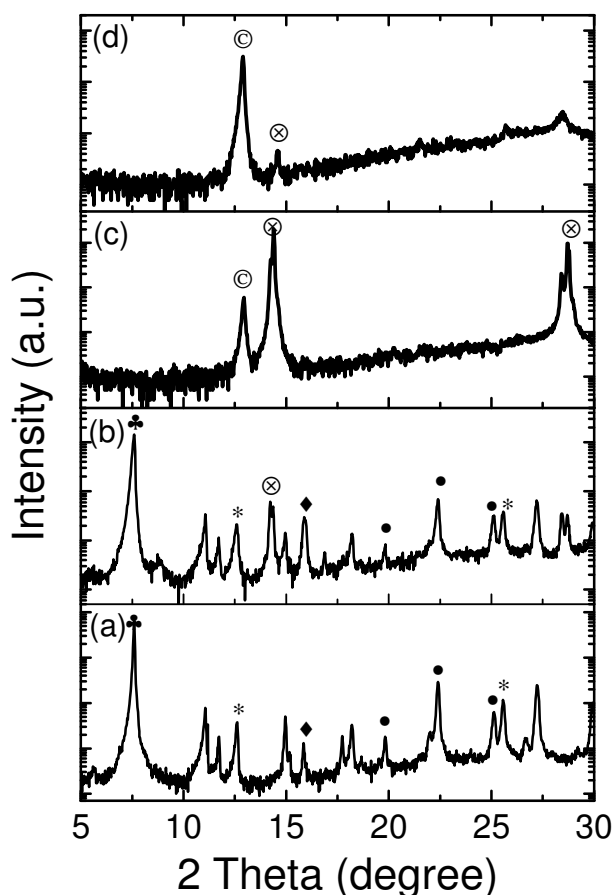


**Figure 3.6:** X-ray diffraction patterns for films deposited on PEDOT:PSS/ITO substrates annealed under  $\text{N}_2$  atmosphere at different annealing temperatures, (a) precursor films without annealing treatment, annealing temperature of (b) 70 °C, (c) 100 °C and (d) 150 °C. The  $\otimes$  indicated the perovskite crystals,  $\odot$  indicated the formation of  $\text{PbI}_2$ ,  $\clubsuit$  indicated the intermediate compound in the precursor film. The other detailed signals would be clarified clearly in the main text.

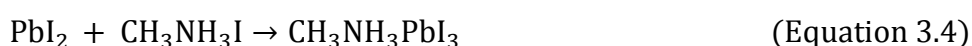
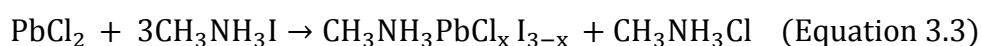
The Bragg reflections with  $2\theta$  angles of  $15.84^\circ$  and  $26.70^\circ$  were observed at early annealing stages which might be assigned to the  $\text{CH}_3\text{NH}_3\text{PbCl}_3$  phase [97, 125, 139, 145], and these reflections disappeared when further annealed precursor film at 100 °C (Figure 3.6c). It could be assumed that these reflections were related to an intermediate phase  $(\text{CH}_3\text{NH}_3)_x\text{PbI}_y\text{Cl}_z$ , as shown in Equation 3.2:



However, the X-ray diffraction data of precursor perovskite film did not reveal any visible Bragg reflections at  $14.40^\circ$ ,  $28.40^\circ$  indicating the (110) and (220) planes of  $\text{CH}_3\text{NH}_3\text{PbI}_3$  perovskite crystalline with a tetragonal structure [97, 144]. In addition, the Bragg reflection with a  $2\theta$  angle of  $7.58^\circ$  was not related to any perovskite crystal

structures or precursor materials. This reflection might be associated with an intermediate phase of a Pb-halide-DMF complex [97, 146]. With thermal annealing treatment to 100°C, this Bragg reflection at  $2\theta = 7.58^\circ$  disappeared which was probably as a result of the removal of residual DMF solvent inside the solid film (Figure 3.6c). The Bragg reflection at  $11.74^\circ$  was likely associated with a  $\text{H}_2\text{O}$ -incorporated perovskite complex at the early thermal annealing stage [125, 147]. The Bragg reflections at  $14.94^\circ$  and  $18.20^\circ$  did not belong to any perovskite or precursor crystalline. The existence of these reflections implied the formation of some complex intermediate phases.

Since there was a significant phase transformation at annealing temperature of 70 °C, it was essential important to detect the crystal structure changes. Therefore, I prepared another precursor perovskite film using the same preparation procedures. And the precursor film was built into EnviroScope experimental chamber and annealed with the same heating procedures and took the sample out after annealing at 70 °C for 5 min. The X-ray diffraction data in Figure 3.6b showed new additional Bragg reflections with  $2\theta$  angles of  $14.40^\circ$ ,  $28.40^\circ$  which were due to the appearance of  $\text{CH}_3\text{NH}_3\text{PbI}_3$  perovskite crystals. However, the Bragg reflection indicating Pb-halide-DMF complex,  $\text{PbCl}_2$  precursor materials were still existed probably because of the incomplete phase transformation. The remaining precursor material  $\text{PbCl}_2$  may also react with  $\text{CH}_3\text{NH}_3\text{PbI}$  leading some perovskite intermediate phases with a release of  $\text{CH}_3\text{NH}_3\text{Cl}$  during thermal annealing process. The partial phase transformation can be described in Equation 3.3 and 3.4, as follows:



When further increasing the annealing temperature to 100 °C, the ex-situ X-ray diffraction data showed other Bragg reflections with  $2\theta$  angles of  $14.40^\circ$  and  $28.40^\circ$  which were assigned to formation of  $\text{CH}_3\text{NH}_3\text{PbI}_3$  perovskite crystals. The Bragg reflections indicating intermediate phases disappeared accompanied by the formation of perovskite crystalline. In addition, the Bragg reflection at  $2\theta = 12.70^\circ$  indicated the presence of  $\text{PbI}_2$  in the annealed film [148]. This was mostly caused by the partial degradation of  $\text{CH}_3\text{NH}_3\text{PbI}_3$  perovskite during thermal annealing at a temperature of 100 °C [149].

With increasing annealing temperature to 120 °C, the  $\text{CH}_3\text{NH}_3\text{PbI}_3$  perovskite crystal decomposed into small crystals at the edge of each crystal structure as shown in Figure 3.4d. The entire crystallized structure would decomposed into small crystals with further high annealing temperature of 150 °C and 160 °C (Figure 3.4e and 3.4f). The



peak intensity of perovskite crystals at  $2\theta = 14.40^\circ$  decreased with the formation of  $\text{PbI}_2$  components (Figure 3.6d). The decomposition of  $\text{CH}_3\text{NH}_3\text{PbI}_3$  perovskite could be described in Equation 3.5.



The ex-situ XRD data were combined with in-situ SFM measurements and tried to elucidate the crystallization mechanism during perovskite film preparation. The above results indicate that many reaction steps occurred during the synthesis of  $\text{CH}_3\text{NH}_3\text{PbI}_3$  crystals from  $\text{PbCl}_2$  and  $\text{CH}_3\text{NH}_3\text{I}$  precursor materials. At the first step, partial ion exchange occurred between precursor materials in the fresh prepared precursor film without any annealing. In addition, an intermediate phase of Pb-halide-DMF complex was detected in ex-situ XRD measurement. The in-situ SFM data did not show obvious morphology changes when the annealing temperature below  $70^\circ\text{C}$ . This might indicate that the removal of residual DMF solvent inside the solid film played a dominant role at early annealing stage.

At the second step,  $\text{CH}_3\text{NH}_3\text{PbI}_3$  crystal structure was observed when annealed at  $70^\circ\text{C}$ . The synthesis of  $\text{CH}_3\text{NH}_3\text{PbI}_3$  led to the formation of  $\text{CH}_3\text{NH}_3\text{Cl}$  or a related crystal, which was related with the significant morphology changes from in-situ SFM measurement.

At the third step, the  $\text{CH}_3\text{NH}_3\text{PbI}_3$  crystal structure was dominant in ex-situ XRD measurement. This finding reveals that the big crystals in the in-situ SFM measurements when film annealed at  $100^\circ\text{C}$  were because of the crystallized  $\text{CH}_3\text{NH}_3\text{PbI}_3$ .

At the fourth step, the formed  $\text{CH}_3\text{NH}_3\text{PbI}_3$  crystals were not stable under higher annealing temperature above  $100^\circ\text{C}$ , which could cause the decomposition of  $\text{CH}_3\text{NH}_3\text{PbI}_3$  big crystals into  $\text{PbI}_2$  small crystals.

Understanding the crystallization and reaction process during thermal annealing enable us to modify the film morphology and tune the crystal size by controlling annealing protocol. The film quality is a key factor for the fabrication of high-efficiency perovskite solar cells.

### 3.3.2 Thermal annealing vs solvent vapor annealing

In addition to the thermal annealing treatment, solvent vapor annealing treatment is another important post-treatment method to improve the crystallization process. Solvent vapor annealing method has been widely applied in organic photovoltaic devices to improve film crystallinity and device performance [150-153]. In 2014, Xiao

et al. [154] and Chen et al. [155] introduced solvent vapor annealing method into the fabrication of perovskite photovoltaics to increase the crystallinity and the grain size. Although larger grain size and better performance were achieved by using solvent vapor annealing, it is still lack of fundamental understanding on film formation and crystal growth. Therefore, in this part the precursor film was prepared inside a  $\text{N}_2$ -filled glovebox and put on the center of a hot plate, and a small amount of DMF solvent was dripped around the precursor film. Then the precursor film and DMF solvent were covered by a glass Petri dish rapidly. Afterwards, the precursor film was thermal annealed at  $100\text{ }^\circ\text{C}$  under DMF solvent vapor atmosphere. Figure 3.7 shows the SFM images of perovskite film annealed under  $\text{N}_2$  and DMF solvent vapor.

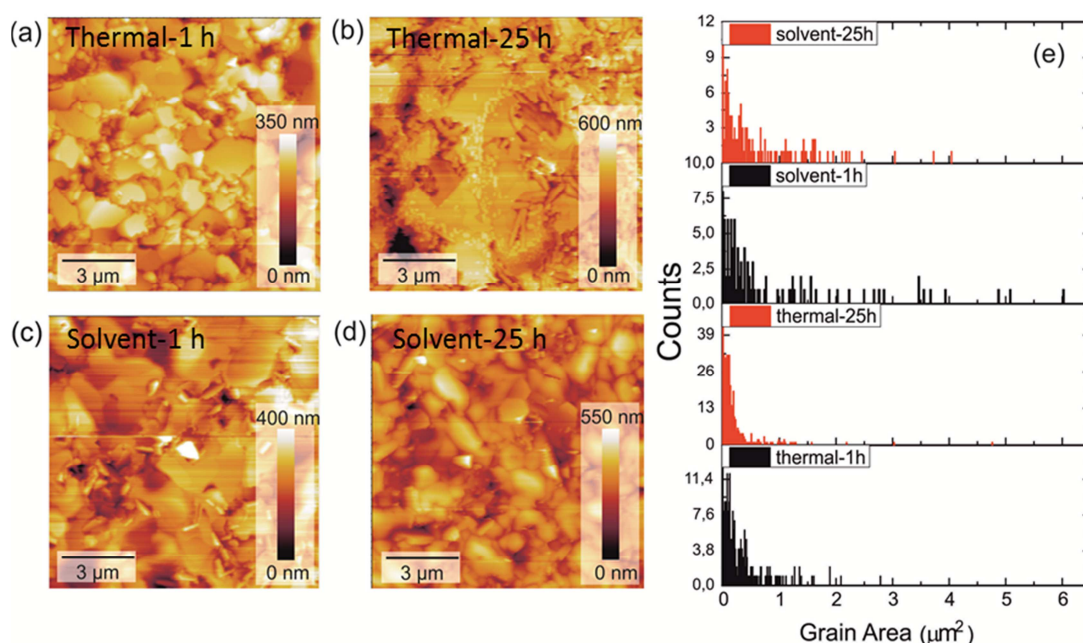


**Figure 3.7:** SFM images of the perovskite films which were thermally annealed at  $100\text{ }^\circ\text{C}$  for 1 hour (a) and 25 hours (b), solvent vapor annealed at  $100\text{ }^\circ\text{C}$  for 1 hour (c) and 25 hours (d). The corresponding grain area distribution obtained based on the SFM images by using Gwyddion software.

The results showed that the perovskite film thermal annealed under  $\text{N}_2$  atmosphere exhibited flat surface with fine crystallites (Figure 3.7a). The perovskite film annealed under DMF solvent vapor showed bigger crystals (Figure 3.7c). The grain area distributions of perovskite films annealed at  $100\text{ }^\circ\text{C}$  for 1 hour showed that thermally annealed film exhibited small crystal size compared with film under DMF solvent vapor annealing (Figure 3.7e). It indicates that DMF vapor might offer a wet atmosphere for  $\text{CH}_3\text{NH}_3\text{I}$  and  $\text{PbCl}_2$  precursor materials during the annealing process, which induces the occurrences of recrystallization and reorganization of perovskite film. Thus  $\text{CH}_3\text{NH}_3\text{PbI}_3$  film showed crystallized domains with bigger grain size under DMF solvent vapor

annealing. However, the DMF solvent vapor annealed perovskite film also showed small crystals around the perovskite crystals, indicating the possible re-dissolve of precursor materials under DMF solvent vapor atmospheres. Furthermore, the DMF solvent vapor annealed film showed a lower maximum absorption relative to the  $\text{N}_2$  annealed film (Figure 3.8). This result could be because of the partially re-dissolved precursor materials under DMF vapor atmosphere, and the partial reaction of precursor materials led to thinner perovskite films. Therefore, it is quite important to control the full reaction of precursor materials during solvent vapor annealing method.

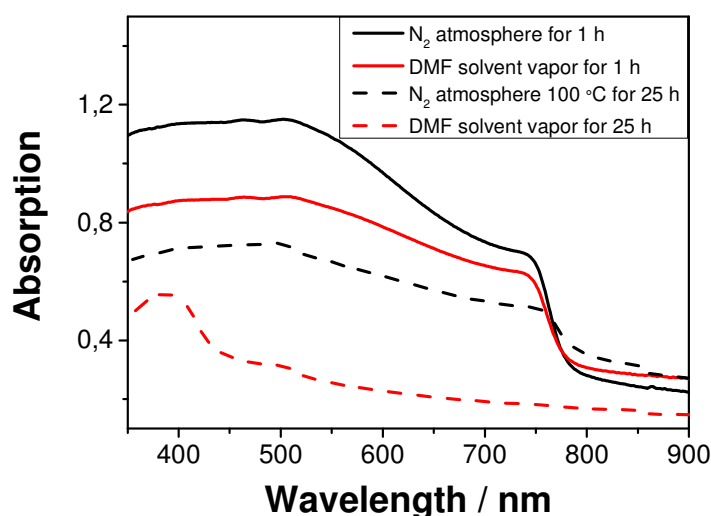


**Figure 3.8:** UV-visible absorption spectra of  $\text{CH}_3\text{NH}_3\text{PbI}_3$  film annealing under  $\text{N}_2$  and DMF solvent vapor for 1 hour and 25 hours.

Furthermore, the crystallinity changes during thermally and solvent vapor annealing processes were measured by using X-ray diffraction. Figure 3.9 shows the X-ray diffraction results of thermally and solvent vapor annealed films. The data show that the  $\text{CH}_3\text{NH}_3\text{PbI}_3$  film annealed under  $\text{N}_2$  and DMF solvent vapor exhibited the same Bragg reflections, which implied the same crystal orientation from these two annealing methods.

From the previous studies in Section 3.3.1, the results showed that when thermally annealed perovskite film at 100 °C for shorter annealing time (below 1 hour) did not induce significant morphology changes (Figure 3.4a-c). To address the effect of prolonging annealing time on the growth of perovskite films, I further thermally annealed the perovskite films at 100 °C for 25 hours, the SFM images in Figure 3.7b showed large amount of small crystals appeared at the edge of perovskite crystals for thermally annealed perovskite film under  $\text{N}_2$  atmosphere. Additionally, the UV-vis absorption spectra showed a decrease in the absorption range below 750 nm, and X-

ray diffraction data exhibited an additional reflection peak at around  $2\theta = 12.9^\circ$  implying the formation of decomposed species  $\text{PbI}_2$ .

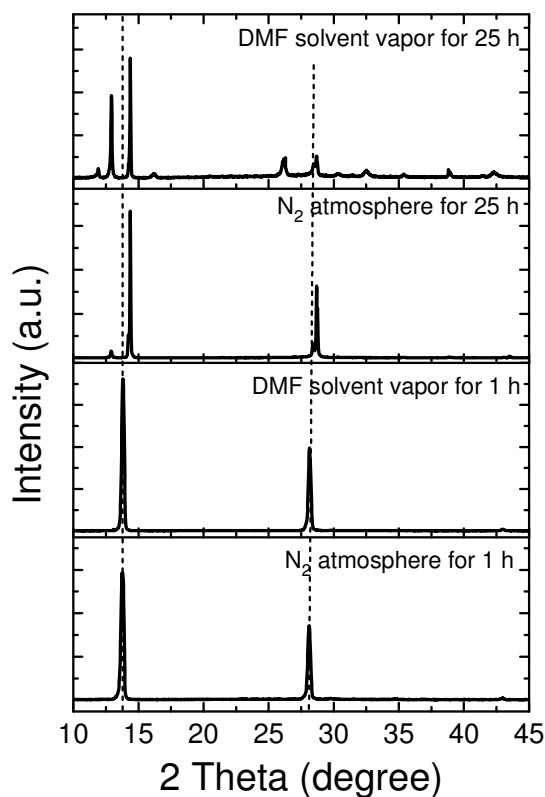


**Figure 3.9:** X-ray diffraction pattern of  $\text{CH}_3\text{NH}_3\text{PbI}_3$  film annealing under  $\text{N}_2$  and DMF solvent vapor for 1 hour and 25 hours.

For the perovskite film annealed under DMF solvent vapor for 25 hours, the SFM image in Figure 3.7d showed the formation of smaller crystal compared with the film solvent vapor annealed for 1 hour. The UV-vis absorption spectra showed a significant decrease in the perovskite absorption range. The remaining absorption spectrum can be attributed mainly to the  $\text{PbI}_2$ . X-ray diffraction data exhibited Bragg reflections at  $2\theta = 12.9^\circ$  and  $14.4^\circ$ , which suggested a decomposition of perovskite crystals. Even though the SFM image in Figure 3.7d still showed good surface morphology and grain size. This observation indicates that solvent-vapor annealed film still maintains good morphology, which should effectively reduce charge loss in the corresponding perovskite solar cells.

### 3.4 Summary and conclusion

In summary, I investigated the effect of annealing temperatures and annealing atmospheres on the morphology and crystallization of  $\text{CH}_3\text{NH}_3\text{PbI}_3$  perovskite films. The in-situ SFM results indicated that the conversion process from precursor materials to perovskite crystals under different annealing temperatures underwent different stages:

Stage 1: Annealed the precursor film below 70 °C under  $\text{N}_2$  atmosphere, there was no significant crystallization occurring on the precursor film. But some precursor material-solvent complex might be formed in the precursor film.

Stage 2: When the annealing temperature reached 70 °C, the perovskite crystal structure was observed by using X-ray diffraction method. It suggested the transition from precursor materials to perovskite crystals. Additionally, this conversion process was combined with the release of certain byproducts.

Stage 3: At annealing temperature of 100 °C, in-situ SFM and X-ray diffraction measurements showed the fully formation of perovskite structure and the disappearance of precursor materials and intermediate phases.

Stage 4: When further increasing the annealing temperature above 100 °C, perovskite crystals decomposed into small  $\text{PbI}_2$  crystals, leading to a degradation of perovskite film.

Compared to the thermal annealing under  $\text{N}_2$  atmosphere, the perovskite film annealed under DMF solvent vapor exhibited good crystallinity with bigger grain size. The above results indicated the importance of annealing temperature, time and atmosphere during film preparation procedures. Higher annealing temperature above 100 °C and prolonging annealing time above 1 hour could lead to the decomposition of  $\text{CH}_3\text{NH}_3\text{PbI}_3$  crystals. To achieve perovskite films with uniform & smooth surfaces and large grain sizes, the post-annealing treatment could be further optimized by controlling the annealing temperature and annealing protocol during film fabrication.



# Chapter 4

## Humidity-induced degradation of $\text{CH}_3\text{NH}_3\text{PbI}_3$ perovskite films

### 4.1 Introduction

The storage of  $\text{CH}_3\text{NH}_3\text{PbI}_3$ -based perovskite solar cells is sensitive to humidity, thus humid environment is always been considered as negative factor for the stability of  $\text{CH}_3\text{NH}_3\text{PbI}_3$ -based solar cells. It was considered that humidity could induce the decomposition of dark brown  $\text{CH}_3\text{NH}_3\text{PbI}_3$  crystals into yellow  $\text{PbI}_2$  components, leading to a degradation of  $\text{CH}_3\text{NH}_3\text{PbI}_3$  films and declining device performance [105-107]. Afterwards, Christians et al. and Yang et al. proposed the formation of a pale yellow hydrated intermediate phase  $(\text{CH}_3\text{NH}_3)_4\text{PbI}_6 \cdot 2\text{H}_2\text{O}$  during the degradation of  $\text{CH}_3\text{NH}_3\text{PbI}_3$  perovskite films at high humid environment [103, 104]. After flushing with dry gas or storing in vacuum, the pale yellow  $(\text{CH}_3\text{NH}_3)_4\text{PbI}_6 \cdot 2\text{H}_2\text{O}$  film rapidly dehydrated and regenerated the characteristic dark brown color of a  $\text{MAPbI}_3$  film. This phenomenon was accompanied by a partial recovery of perovskite absorbance which indicated a partial reversibility of  $(\text{CH}_3\text{NH}_3)_4\text{PbI}_6 \cdot 2\text{H}_2\text{O}$  hydrate phase [103, 104].

Recently, Leguy et al. [111] introduced a degradation model of  $\text{CH}_3\text{NH}_3\text{PbI}_3$  upon exposure of the compound to humidity. First, a monohydrate  $\text{CH}_3\text{NH}_3\text{PbI}_3 \cdot \text{H}_2\text{O}$  at an early humidity induced-degradation stage was observed, which was fully reversible upon subsequent drying in gas. Second, a dihydrate  $(\text{CH}_3\text{NH}_3)_4\text{PbI}_6 \cdot 2\text{H}_2\text{O}$  formed upon longer exposure time. Leguy et al. found that the hydration process was isotropic and homogeneous throughout the film [111]. Based on time-resolved ellipsometry, X-ray diffraction (XRD) and JV measurements, Leguy et al. proposed a microscopic degradation mechanism. The hydration of the  $\text{CH}_3\text{NH}_3\text{PbI}_3$  led to a separation of grains which resulted in electrical isolation and increased charge recombination at the grain interface. Interestingly, the JV behavior recovered almost to its original state upon subsequent drying of the film.

However, Leguy et al. noticed an increase in the magnitude of the JV-hysteresis behavior that might be associated with perovskite crystal size. In another context, Kim

and Park reported that a decrease in crystal size led to an increasing hysteresis [112]. In addition, Leguy et al. observed an increase in the magnitude of JV-hysteresis behavior of the degraded  $\text{CH}_3\text{NH}_3\text{PbI}_3$ -based solar cell [111]. Nevertheless, it is still an open question to which extends the temporary exposure to humidity leads to irreversible changes in the film, which can be a drawback for commercial application.

In this chapter, the  $\text{CH}_3\text{NH}_3\text{PbI}_3$  perovskite films were exposed at different humid environments, 0%, 20%, 50% and 80% at room temperature. For the lower humidity (0%, 20% and 50%), the in-situ scanning force microscope (in-situ SFM) and ex-situ X-ray diffraction pattern (ex-situ XRD) were applied to observe the morphology and crystal structure changes. For the  $\text{CH}_3\text{NH}_3\text{PbI}_3$  perovskite film exposure at 80% humidity, I performed in-situ scanning force microscope (in-situ SFM) and in-situ X-ray diffraction (in-situ XRD) measurements to track changes in the film morphology and the crystal structure. The aim is to refine the current picture of humidity-induced degradation of inverted planar  $\text{CH}_3\text{NH}_3\text{PbI}_3$  perovskite solar cells.

## 4.2 Experimental section

### Preparation of $\text{CH}_3\text{NH}_3\text{PbI}_3$ perovskite films

Methylammonium iodide ( $\text{CH}_3\text{NH}_3\text{I}$ ) was synthesized using the method from Lee et al. [72]. Lead chloride ( $\text{PbCl}_2$ , Sigma Aldrich, 99,999%) was carefully dehydrated under high vacuum conditions and nitrogen atmosphere at 60 °C. The perovskite precursor solution was prepared by mixing  $\text{CH}_3\text{NH}_3\text{I}$  (1.0 g) and  $\text{PbCl}_2$  (582 mg) in 2.505 ml anhydrous N,N-dimethylformamide (DMF, Sigma Aldrich) with molar ratio of 3:1 at 60 °C and stirred overnight in  $\text{N}_2$ -filled glovebox. The precursor solution was passed through a 0.45  $\mu\text{m}$  filter before usage and deposited onto poly(3,4-ethylene dioxythiophene) polystyrene sulfonate (PEDOT:PSS, Sigma Aldrich) by spin-coating at 2000 rpm for 60 s. After resting for 10 min, the precursor films were put on top of a hotplate at a temperature of 100 °C for 30 min to obtain perovskite crystal structures. All films were prepared and stored in a  $\text{N}_2$ -filled glovebox prior to measurements.

## 4.3 Results and discussion

### 4.3.1 $\text{CH}_3\text{NH}_3\text{PbI}_3$ films at low humidity (0%, 20% and 50%)

In the beginning, a  $\text{CH}_3\text{NH}_3\text{PbI}_3$  film was exposed to 0% humidity and in-situ SFM experiments were performed to locally track the morphology evolution. Here, the



$\text{CH}_3\text{NH}_3\text{PbI}_3$  perovskite film was built into a MFP-3D SFM device, which is stored inside a  $\text{N}_2$ -filled glovebox to protect the experiment from exposure to air or humidity. Before humidity exposure, the  $\text{CH}_3\text{NH}_3\text{PbI}_3$  perovskite films contained large crystalline (Figure 4.1a, d, g). I locally measured the film morphology changes every 24 hours. It is found that film morphology kept the same before and after humidity exposure at low humidity environment  $\leq 20\%$  even when exposed the  $\text{CH}_3\text{NH}_3\text{PbI}_3$  films for 144 hours, 6 days (Figure 4.1c, f). At a humidity of 50%, additional holes were formed in the  $\text{CH}_3\text{NH}_3\text{PbI}_3$  films after 24 hours (Figure 4.1h), which did not change with further exposure to 50% humidity even up to 6 days (Figure 4.1l). This observation is also in agreement with the report from Matsumoto et al. that the optical properties of the  $\text{CH}_3\text{NH}_3\text{PbI}_3$  perovskite film did not change when exposed to a relative humidity of 40% in the dark [156].

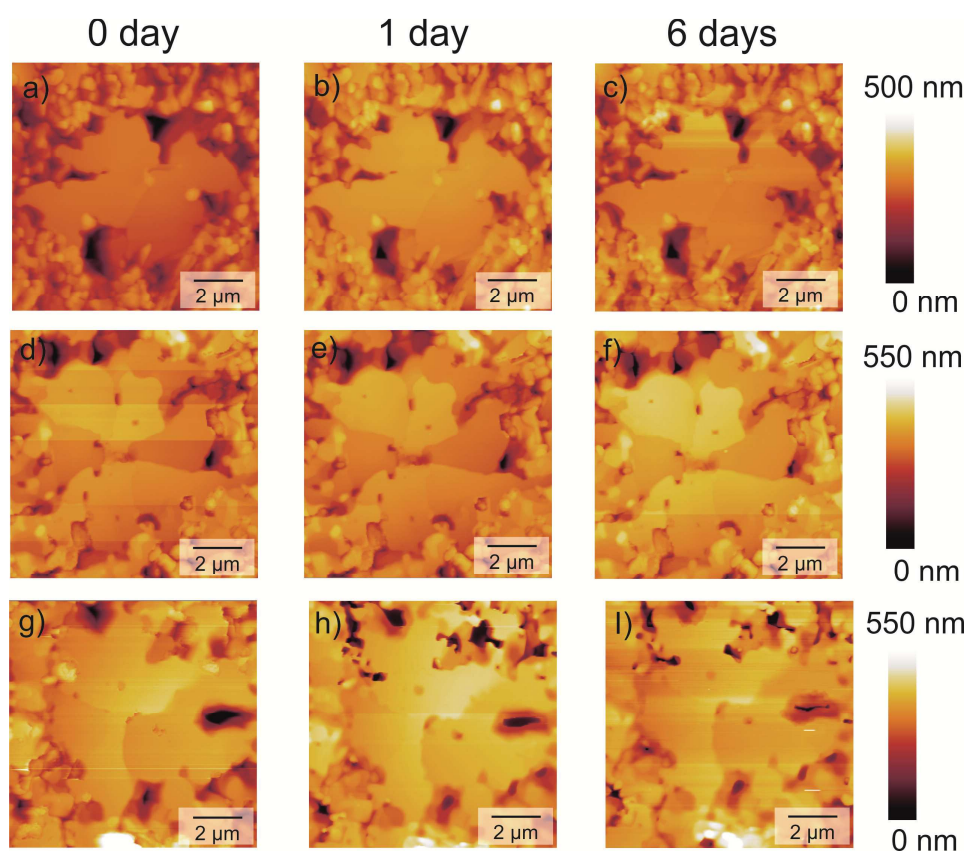


**Figure 4.1:** SFM images of  $\text{CH}_3\text{NH}_3\text{PbI}_3$  perovskite films exposed to a humidity of 0%, inside a  $\text{N}_2$ -filled glovebox (a, b, c), 20% (d, e, f) and 50% (g, h, l) for different exposure times 0 day (a, d, g), 1 day (b, e, h) and 6 days (c, f, l).

In order to detect the effect of long-time humidity exposure on the electronic structure and crystal structure of perovskite  $\text{CH}_3\text{NH}_3\text{PbI}_3$  films, UV-visible absorption spectroscopy and X-ray diffraction measurements were performed on  $\text{CH}_3\text{NH}_3\text{PbI}_3$  films ex-situ before and after humidity exposure for 6 day (Figure 4.2 - 4.4). The

degraded  $\text{CH}_3\text{NH}_3\text{PbI}_3$  perovskite film used for ex-situ UV-visible absorption spectroscopy and X-ray diffraction measurements were built into an atmospheric chamber and exposed to different humidity environments (0%, 20% and 50%) for 6 days. Afterwards, the degraded films were taken out from the atmospheric chamber and sealed by using Para film to protect from further exposure to air. The typical absorption spectrum of a non-degraded  $\text{CH}_3\text{NH}_3\text{PbI}_3$  film shows a broad absorption in the range of 400 - 530 nm with an onset at around 780 nm corresponding to the material's optical band gap  $E_g = 1.58 \text{ eV}$  [128, 157]. Our ex-situ UV-vis absorption spectra show that the degraded  $\text{CH}_3\text{NH}_3\text{PbI}_3$  films exposed to  $\leq 50\%$  humidity have comparable absorption spectra with the initial non-degraded  $\text{CH}_3\text{NH}_3\text{PbI}_3$  film over the visible to near-IR spectrum range (Figure 4.2).

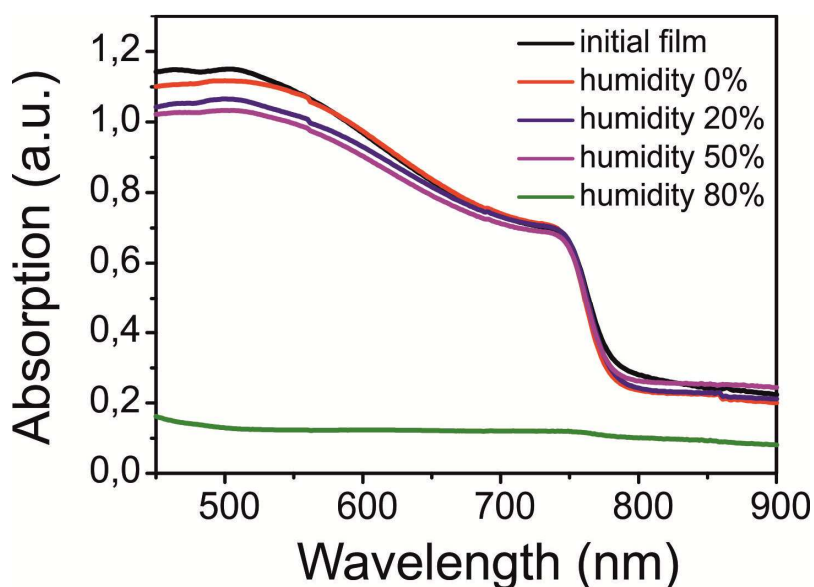


**Figure 4.2:** Ex-situ UV-vis absorption spectra of degraded  $\text{CH}_3\text{NH}_3\text{PbI}_3$  films at different humidity atmospheres (0%, 20%, 50%) before and after 144 hours (6 days).

In addition, the X-ray diffraction measurements were carried out on non-degraded and degraded  $\text{CH}_3\text{NH}_3\text{PbI}_3$  perovskite films coated on top of PEDOT:PSS/ITO substrates. First, a reference sample of PEDOT:PSS/ITO substrate was made for ex-situ X-ray diffraction measurements (Figure 4.3). The Bragg reflections with  $2\theta$  angles at  $20.88^\circ$ ,  $29.92^\circ$ ,  $34.90^\circ$  and  $50.24^\circ$  are assigned to the PEDOT:PSS/ITO substrate [158]. The X-ray diffraction data of non-degraded  $\text{CH}_3\text{NH}_3\text{PbI}_3$  perovskite film exhibits Bragg reflections with  $2\theta$  angles at  $14.38^\circ$ ,  $28.72^\circ$ ,  $31.98^\circ$  and  $43.52^\circ$  indicating the (110), (220), (310) and (330) planes of tetragonal  $\text{CH}_3\text{NH}_3\text{PbI}_3$  perovskite structure (Figure 4.4) [72, 139, 154, 159]. The X-ray diffraction data did not reveal changes of the diffraction peaks before and after exposed at low humidity environments  $\leq 20\%$  for 6 days.

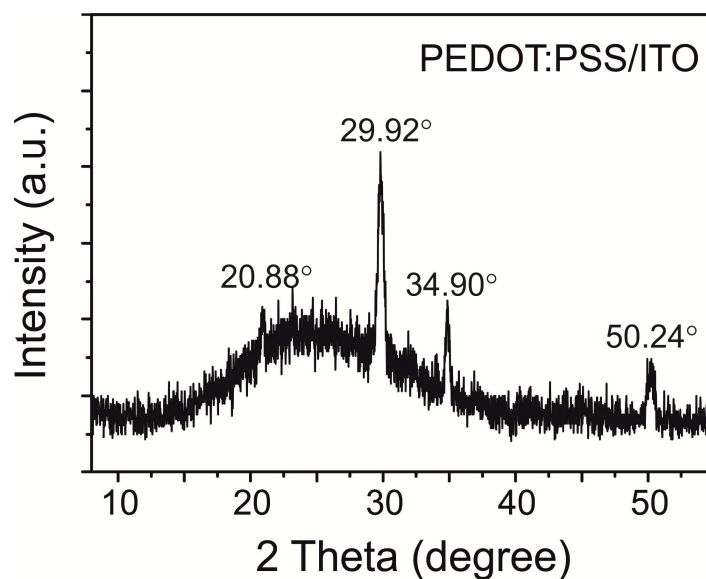


**Figure 4.3:** X-ray diffraction of PEDOT:PSS layer spin-coated on top of pre-cleaned ITO glass substrate.

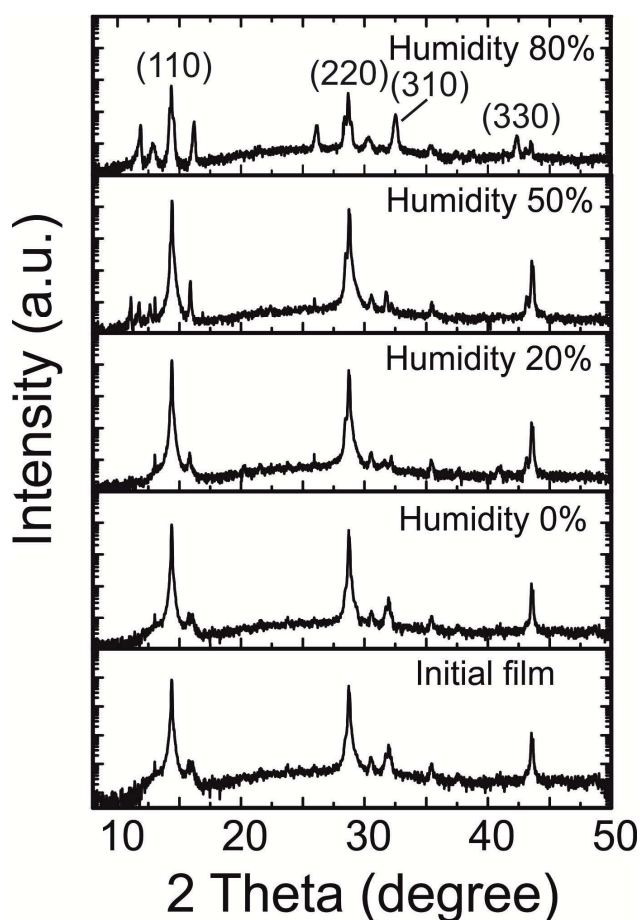


**Figure 4.4:** Ex-situ X-ray diffraction patterns of non-degraded  $\text{CH}_3\text{NH}_3\text{PbI}_3$  film and degraded  $\text{CH}_3\text{NH}_3\text{PbI}_3$  films at different humidity conditions (0%, 20%, 50% and 80%) after 144 hours (6 days).

SFM, UV-vis spectra and X-ray diffraction experiments did not indicate degradation in the macrostructure and crystal structure of  $\text{CH}_3\text{NH}_3\text{PbI}_3$  perovskite film after exposure for 144 hours to low humidity  $\leq 20\%$  in the dark at room temperature. This observation is also in agreement with the report from Matsumoto et al. who found that the optical properties of the  $\text{CH}_3\text{NH}_3\text{PbI}_3$  perovskite film did not change upon exposure to a relative humidity of 40% in the dark [156]. At a humidity of 50%, SFM image in Figure 4.1 shows additional holes formed after 24 hours. However, the formed morphology did not change for further humidity exposure for 6 days.

### 4.3.2 $\text{CH}_3\text{NH}_3\text{PbI}_3$ film at 80% humidity

#### In-situ SFM measurements

There are no significant morphology and structure changes under low humidity conditions. Thus I furthered increased the humidity to 80% and varied exposure time. To track humidity-induced morphology changes, in-situ SFM experiments were performed in the center of  $\text{CH}_3\text{NH}_3\text{PbI}_3$  perovskite films on top of PEDOT:PSS coated ITO substrates. This preparation procedure is often used for a one-step preparation of planar type  $\text{CH}_3\text{NH}_3\text{PbI}_3$  perovskite solar cells leading to PCEs up to 17.1% [79]. At first, I varied the exposure time and probed time-resolved morphology evolution under a controlled humidity level of 80% (Figure 4.5). Before humidity exposure, the  $\text{CH}_3\text{NH}_3\text{PbI}_3$  perovskite film contained crystalline up to a diameter of 4  $\mu\text{m}$ , which exhibits a smooth topography profile with a peak-to-peak roughness below 3.0 nm after subtracting the background slope (Figure 4.5a). After 4 hours of exposure to a humidity of 80%, the topography in the  $\text{CH}_3\text{NH}_3\text{PbI}_3$  film changed (black profile line in Figure 4.5b). The smooth topography appeared additional steps which had a height up to 5.0 nm (Figure 4.5b). With prolonging exposure time, more steps were introduced and the groves with depths of around 1.5 nm appeared in the  $\text{CH}_3\text{NH}_3\text{PbI}_3$  film (Figure 4.5c). The rough topography and additional groves were attributed to the grain boundaries which were generated in  $\text{CH}_3\text{NH}_3\text{PbI}_3$  perovskite crystallites upon exposure to 80% humidity (Figure 4.5b - 4.5d).

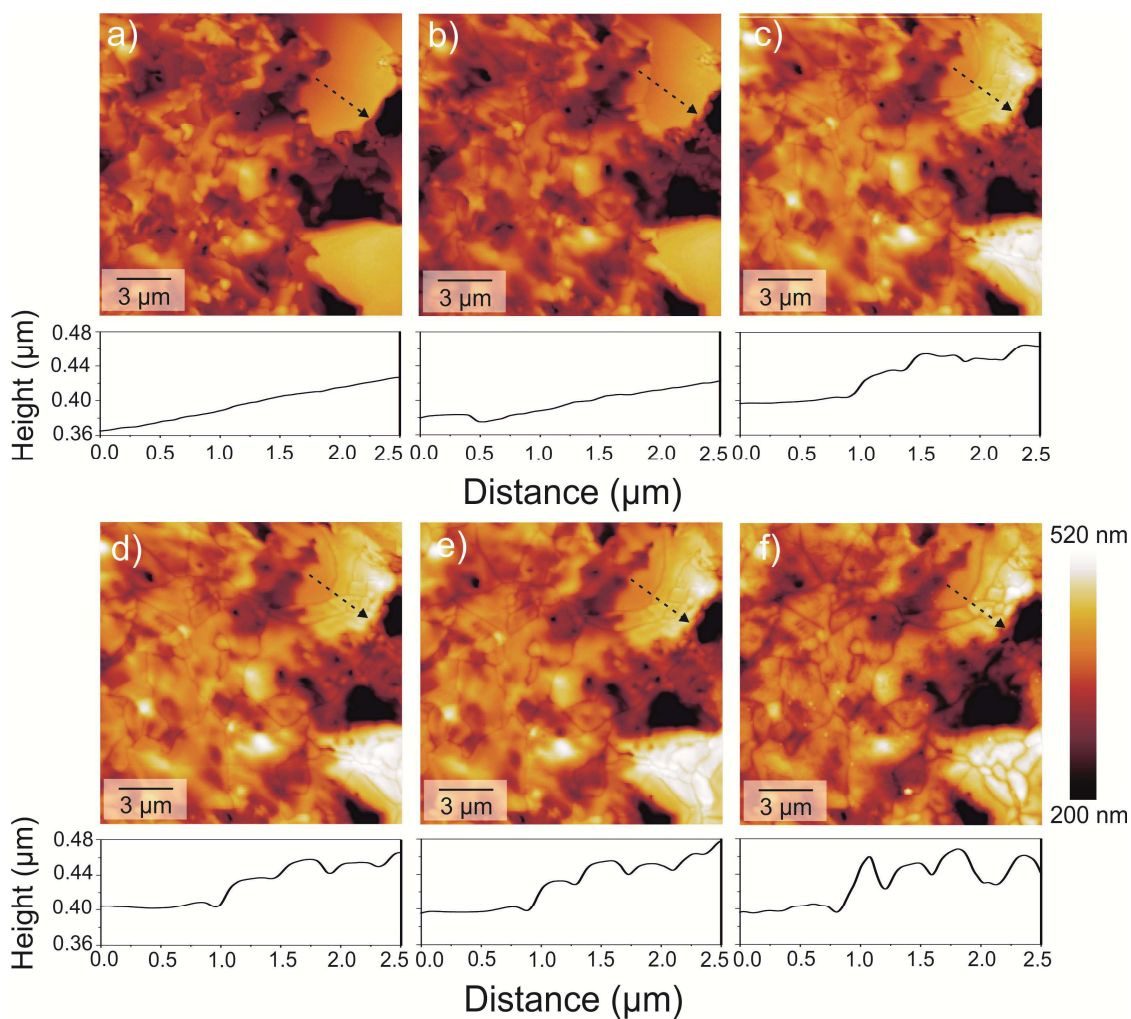


**Figure 4.5:** SFM images and profiles of the  $\text{MAPbI}_3$  films in a humidity level of 80% at different exposure times (a) initial morphology, after (b) 4 hours, (c) 6 hours, (d) 8 hours, (e) flushing with dry  $\text{N}_2$  overnight (13 hours) and (f) 80% humidity for 144 hours. The SFM profiles were extracted from the same area along the black profile lines indicated in each SFM image. SFM experiments were performed without external illumination. The SFM setup is operated in the dark at constant temperature of 20 °C with a laser power less than 1.0 mW at a wavelength of 670 nm to read out the cantilever deflection. The laser focus was positioned slightly away from the apex of the cantilever to avoid illumination of the sample.

Afterwards, I closed the tube of humid  $\text{H}_2\text{O}$  vapor and exposed the  $\text{CH}_3\text{NH}_3\text{PbI}_3$  perovskite films to dry  $\text{N}_2$  gas. The rough topography because of 80% humidity exposure was conserved and the depth of the grain boundaries also remained constant (Figure 4.5e). Therefore, humidity-induced morphology degradation was irreversible in terms of the surface microstructure. Upon further elongating the exposure time to 144 hours (6 days), more new grain boundaries formed and the depth of grain boundaries



increased (Figure 4.5f). An analysis of the grain sizes revealed that only grains above 500 nm are subject to additional grain boundaries upon exposure to humidity. Furthermore, the change in morphology was reflected in a change in the root-mean-square roughness (rms) of the  $\text{CH}_3\text{NH}_3\text{PbI}_3$  perovskite film, which increased from 60 – 65 nm to 80 nm in the measured area of around  $155 \mu\text{m}^2$  for the longest exposure time that was used here (Figure 4.6).

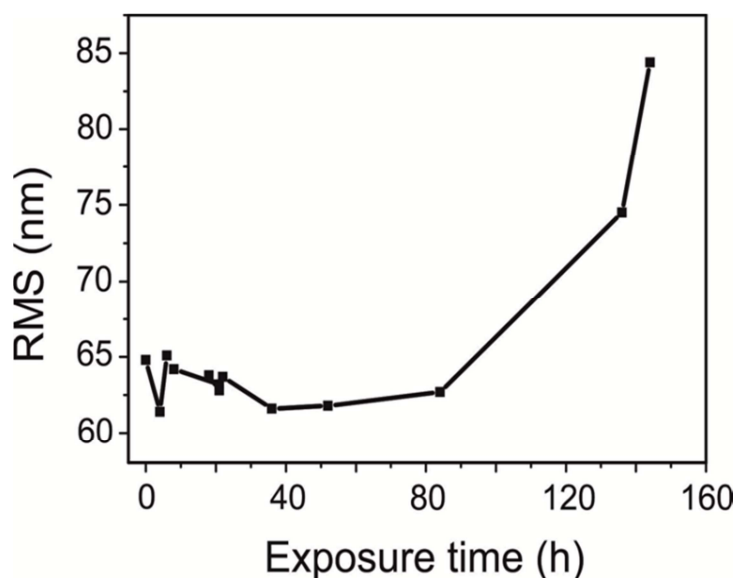


**Figure 4.6:** Root-Mean-Square (RMS) values of surface roughness for  $\text{CH}_3\text{NH}_3\text{PbI}_3$  film the time-resolved SFM images at a humidity of 80% vs exposure time.

As shown in Figure 4.2, the absorption spectra of degraded  $\text{CH}_3\text{NH}_3\text{PbI}_3$  film at a humidity of 80% for 144 hours showed a significant decrease of about 90% at the absorption peak of 750 nm (perovskite band edge). This phenomenon indicated that high humid atmosphere greatly affect the electronic properties of  $\text{CH}_3\text{NH}_3\text{PbI}_3$  film, and the optical absorption at the visible region was also significantly decreased [127]. In addition, except for the reflections at  $14.38^\circ$  and  $28.72^\circ$  indicating the tetragonal  $\text{CH}_3\text{NH}_3\text{PbI}_3$  perovskite crystals, the ex-situ XRD experiments of degraded  $\text{CH}_3\text{NH}_3\text{PbI}_3$  film showed additional reflections at  $2\theta$  angles of  $11.80^\circ$  and  $12.45^\circ$  which implied the formation of dihydrated phase  $(\text{CH}_3\text{NH}_3)_4\text{PbI}_6 \cdot 2\text{H}_2\text{O}$ . This phenomenon indicates that additional degraded phases appeared during the high humidity-induced degraded process. To correlate the appearance of grain boundaries with the formation of additional phases, I performed time-resolved in-situ XRD measurements on a freshly prepared sample that was not exposed to humidity before.

## In-situ XRD data

The X-ray diffraction data for a non-degraded  $\text{CH}_3\text{NH}_3\text{PbI}_3$  film showed strong Bragg reflections at  $2\theta$  angles of  $14.38^\circ$ ,  $20.27^\circ$ ,  $23.80^\circ$ ,  $24.77^\circ$  and  $28.72^\circ$  (Figure 4.7a). They were attributed to the (110), (200), (211), (202) and (220) crystal planes of the tetragonal  $\text{CH}_3\text{NH}_3\text{PbI}_3$  perovskite structure [104, 160]. The weak Bragg reflection at  $12.90^\circ$  indicates the presence of  $\text{PbI}_2$  crystalline in the freshly prepared  $\text{CH}_3\text{NH}_3\text{PbI}_3$  film [104, 161]. The co-existence of  $\text{PbI}_2$  crystal is likely to be caused by thermal annealing at  $100^\circ\text{C}$  during film preparation [149].

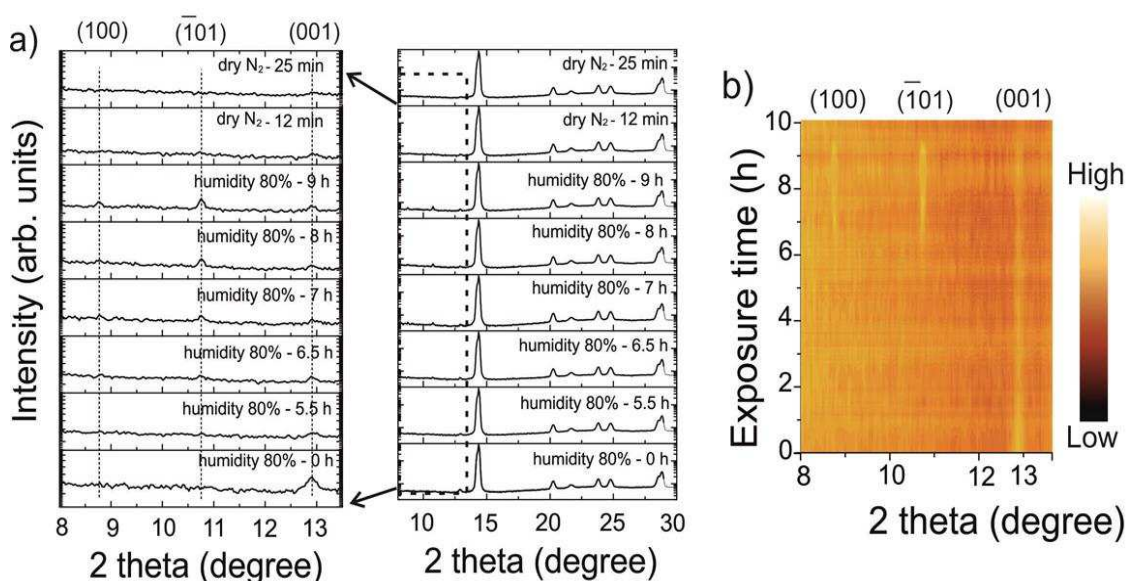


**Figure 4.7:** Time-resolved in-situ XRD of a  $\text{CH}_3\text{NH}_3\text{PbI}_3$  film during first hydration-dehydration round and the zoom-in image at  $2\theta$  angles from  $8.0^\circ$  to  $13.5^\circ$  (a) and the corresponding contour plot showing changes in XRD peak intensity during the first hydration-dehydration cycle (b).

Afterwards, the experimental chamber was flushed with 80% humid  $\text{N}_2$  gas. In-situ XRD measurements in reflection geometry were made every 15 minutes at the same sample tilted angle of 5 degree. After exposed to 80% humidity for 5.5 hours, additional Bragg reflections at a  $2\theta$  angle of  $10.75^\circ$  were detected (Figure 4.7a at humidity 80% for 5.5 h). This Bragg reflection indicates the formation of monohydrate phase  $\text{CH}_3\text{NH}_3\text{PbI}_3 \cdot \text{H}_2\text{O}$  during hydration process [111]. Another Bragg reflection at  $2\theta$  angle of  $8.76^\circ$  appeared after 6.5 hours exposure to 80% humidity, indicating the formation of  $\text{CH}_3\text{NH}_3\text{PbI}_3 \cdot \text{H}_2\text{O}$  monohydrate phase (Figure 4.7a at humidity 80% for 6.5 h). The Bragg reflections at the  $2\theta$  angles of  $8.76^\circ$  and  $10.75^\circ$  corresponds to the (100) and  $(\bar{1}01)$  reflections of monoclinic P21/m crystal structure, indicating the formation monohydrate phase  $\text{CH}_3\text{NH}_3\text{PbI}_3 \cdot \text{H}_2\text{O}$  [111]. This phenomenon implies that water

molecules first preferentially approached and located on a certain side of the  $\text{CH}_3\text{NH}_3\text{PbI}_3$  perovskite crystal structure. Water molecules may form hydrogen bonds with perovskite cavity [96].

In order to visualize the appearance of the Bragg reflections and the transformation process, I plotted the X-ray diffraction pattern data versus time in a contour plot (Figure 4.7b). At exposure times of  $> 6 \text{ h} \pm 15 \text{ min}$ , clear Bragg reflections at (100) and  $(\bar{1}01)$  were detected. Interestingly, the appearance of the (100) and  $(\bar{1}01)$  diffraction peaks coincided in time with the appearance of grain boundaries as observed by in-situ SFM experiment. Upon further exposure of the  $\text{CH}_3\text{NH}_3\text{PbI}_3$  film to a humid environment, the peak intensities of the monohydrate phase increased accordingly (Figure 4.7a at 7 h, 8 h, and 9 h). As been reported previously, the monohydrate phase  $\text{CH}_3\text{NH}_3\text{PbI}_3 \cdot \text{H}_2\text{O}$  could dehydrate spontaneously in dry environments by forming polycrystalline  $\text{CH}_3\text{NH}_3\text{PbI}_3$  [147]. Therefore, the hydration process was stopped after 9 hours by switching to flush the experimental chamber with dry  $\text{N}_2$  gas. The X-ray diffraction data revealed that the Bragg reflections indicating  $\text{CH}_3\text{NH}_3\text{PbI}_3 \cdot \text{H}_2\text{O}$  monohydrate were still detectable after 10 min drying, but disappeared after 25 min (Figure 4.7).

Based on these results, I can conclude that the formation of monohydrate phase at around 5.5 h is linked to the appearance of steps and grain boundaries observed by in-situ SFM measurements. One plausible explanation would be that upon humidity exposure the  $\text{CH}_3\text{NH}_3\text{PbI}_3$  perovskite film swells. Thus it was very likely that at the initial stage (0 - 5.5 h) water molecules diffused into  $\text{CH}_3\text{NH}_3\text{PbI}_3$  structure but did not form a significant portion of the hydrated phase. When a critical uptake of water was reached, the hydrated methylammonium lead iodide phase  $\text{CH}_3\text{NH}_3\text{PbI}_3 \cdot \text{H}_2\text{O}$  formed. The transformation of  $\text{CH}_3\text{NH}_3\text{PbI}_3$  perovskite to monohydrate phase  $\text{CH}_3\text{NH}_3\text{PbI}_3 \cdot \text{H}_2\text{O}$  led to a 6% volume expansion, which was based on the relative lattice parameters of  $\text{CH}_3\text{NH}_3\text{PbI}_3$  ( $247 \text{ \AA}^3$  per formula unit) and  $\text{CH}_3\text{NH}_3\text{PbI}_3 \cdot \text{H}_2\text{O}$  ( $263 \text{ \AA}^3$  per formula unit) [110, 111, 147]. Therefore, the stress inside the  $\text{CH}_3\text{NH}_3\text{PbI}_3$  film built up and was released by creating additional steps and grain boundaries.

## Repeated hydration-dehydration process

Directly after the first exposure to 80% humidity (hydration) and subsequent drying in  $\text{N}_2$  gas (dehydration), a second hydration-dehydration experiment was performed. As shown in Figure 4.8, the Bragg reflection at  $2\theta$  angle of  $10.75^\circ$  indicating (100) reflection of  $\text{CH}_3\text{NH}_3\text{PbI}_3 \cdot \text{H}_2\text{O}$  monohydrate phase was first detected after 7 hours. The Bragg reflection at  $8.76^\circ$  indicating the  $(\bar{1}01)$  reflection of  $\text{CH}_3\text{NH}_3\text{PbI}_3 \cdot \text{H}_2\text{O}$



monohydrate phase appeared after 9 hours (Figure 4.8a). At exposure times  $> 9$  hours, the peak intensity of monohydrate phase gradually increased with prolonging exposure time at 80% humidity, while the peak intensity of  $\text{CH}_3\text{NH}_3\text{PbI}_3$  perovskite at (110) Bragg reflection only slightly decreased (Figure 4.8a and 4.8b). Thus, a significant fraction of  $\text{CH}_3\text{NH}_3\text{PbI}_3$  crystals was not directly affected by humidity.

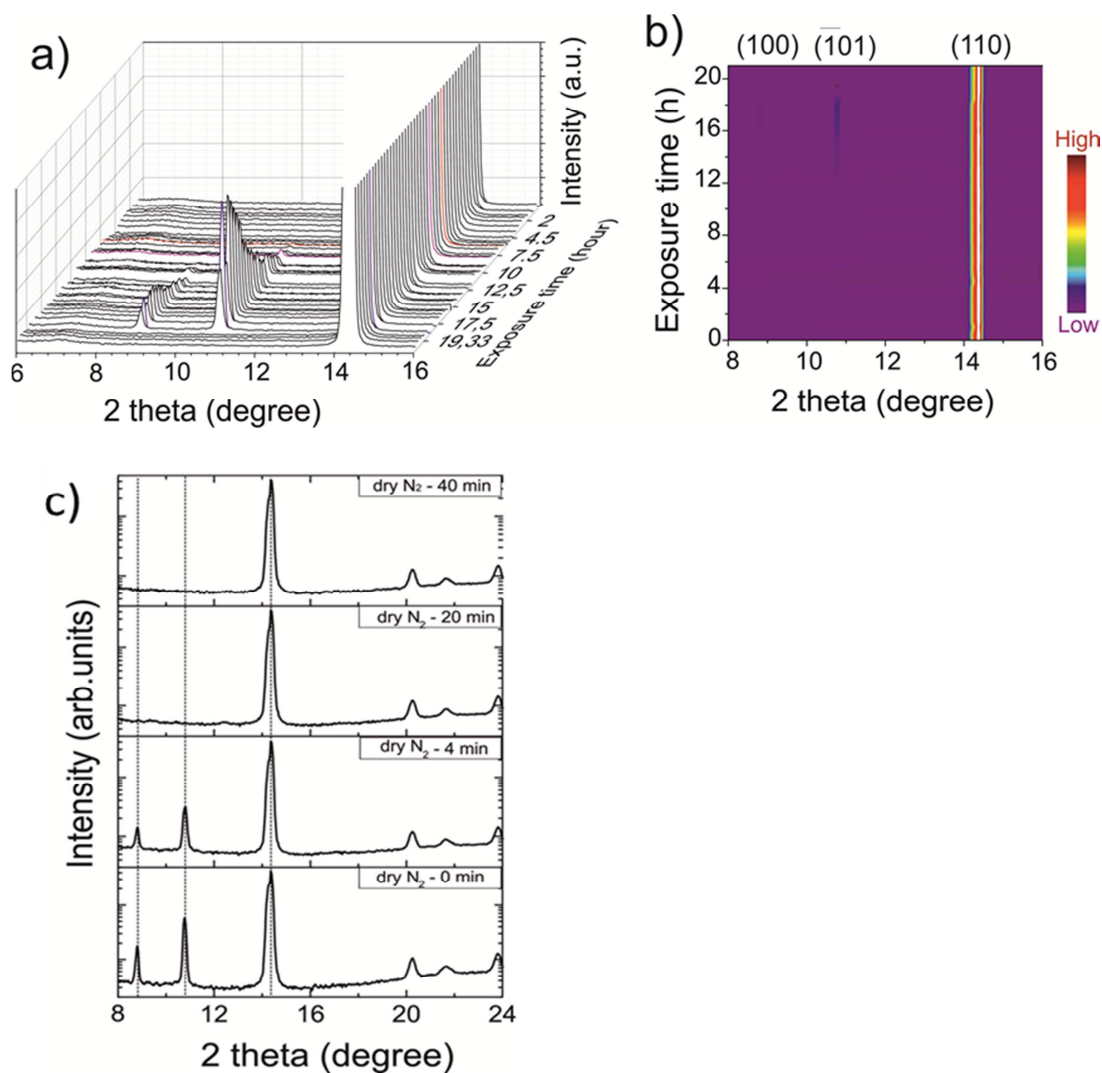


**Figure 4.8:** 3D waterfall graph of time-resolved in-situ X-ray diffraction results of a  $\text{CH}_3\text{NH}_3\text{PbI}_3$  film at the second hydration-dehydration round (a), and the corresponding contour plot shows changes in reflection peak intensities during the hydration-dehydration cycle (b). The in-situ dehydration process flushing with dry  $\text{N}_2$  at different drying times (c). The diffraction patterns show that the recovery of perovskite compound  $\text{CH}_3\text{NH}_3\text{PbI}_3$  was accompanied by disappearance of  $\text{CH}_3\text{NH}_3\text{PbI}_3 \cdot \text{H}_2\text{O}$  monohydrated phase within 20 minutes.

After exposing the  $\text{CH}_3\text{NH}_3\text{PbI}_3$  perovskite film at 80% humidity for 19 hours, I switched to flush the experimental chamber with dry  $\text{N}_2$  gas. The (100) and  $(\bar{1}01)$  Bragg reflections of monohydrate  $\text{CH}_3\text{NH}_3\text{PbI}_3 \cdot \text{H}_2\text{O}$  remained visible after flushing for 4 min. However, they disappeared before the third measurements, starting after 20 min dehydration. This phenomenon is similar to the first hydration-dehydration round that the dehydration process was much faster than hydration.

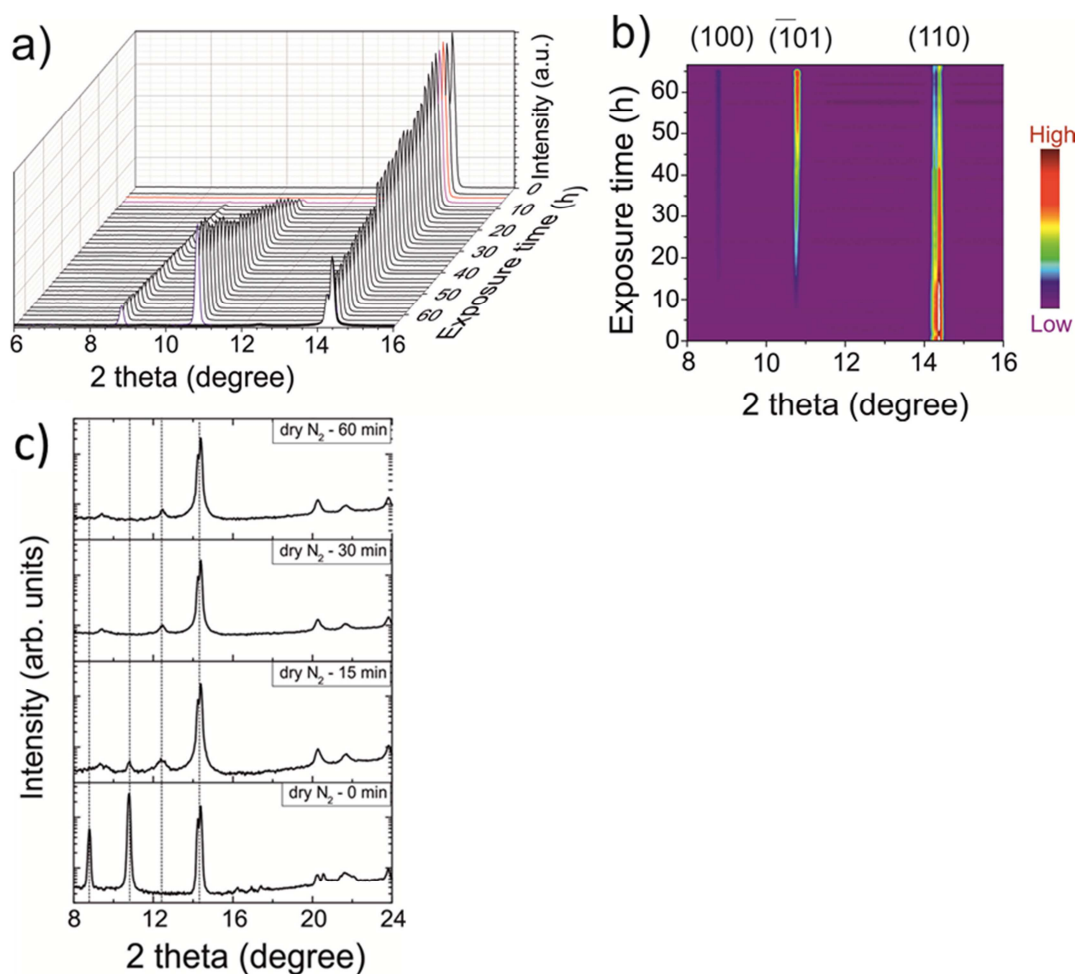


**Figure 4.9:** The 3D waterfall graph of the time-resolved in-situ X-ray diffraction results at the third hydration-dehydration round (a) and the corresponding contour plot (b). The in-situ dehydration process flushing with dry  $\text{N}_2$  at different drying times (c).

Afterwards, a third long-term exposure of the  $\text{CH}_3\text{NH}_3\text{PbI}_3$  perovskite film to a humidity of 80% for 65 hours was carried out (Figure 4.9). The XRD measurements indicated the presence of  $(\bar{1}01)$  reflection in monohydrate phase  $\text{CH}_3\text{NH}_3\text{PbI}_3 \cdot \text{H}_2\text{O}$  after 5 hours exposure to humidity. The peak intensities of (100) and  $(\bar{1}01)$  reflections in monohydrate phase increased with prolonging exposure time. Simultaneously the peak intensity of (110) reflection at a  $2\theta$  angle of  $14.38^\circ$  in  $\text{CH}_3\text{NH}_3\text{PbI}_3$  perovskite

structure decreased (Figure 4.10). Even close to the end of exposure experiment after 65 hours, still no saturation of the peak intensities was observed. In the following, I switched off the  $\text{H}_2\text{O}$  humidity tube and flushed the experimental chamber with dry  $\text{N}_2$  gas. Even after this long-term humidity exposure, the monohydrate phase  $\text{CH}_3\text{NH}_3\text{PbI}_3 \cdot \text{H}_2\text{O}$  disappeared within 30 min (Figure 4.9c).

However, the Bragg reflection corresponding to the  $\text{CH}_3\text{NH}_3\text{PbI}_3$  perovskite structure clearly did not return to its initial intensity value (Figure 4.10). A possible explanation is that only a fraction of the hydrated phase was converted back into  $\text{CH}_3\text{NH}_3\text{PbI}_3$  perovskite structure. Additionally, a new Bragg reflection at a  $2\theta$  angle of  $12.45^\circ$  appeared during the dehydration process (Figure 4.9c). This peak indicates the formation of crystalline  $\text{PbI}_2$  at the late dehydration process.

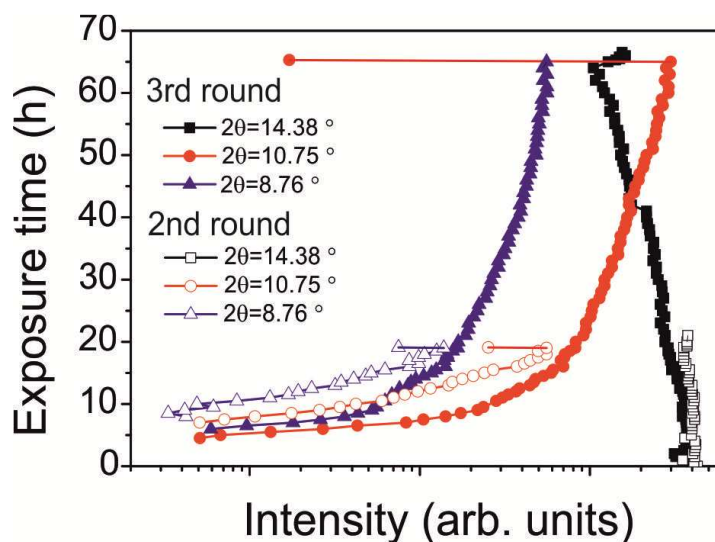


**Figure 4.10:** The peak intensities as a function of exposure time (c): perovskite  $2\theta=14.38^\circ$  (110) reflection, monohydrate phase which locates at  $10.75^\circ$  ( $\bar{1}01$ ) reflection and  $8.76^\circ$  (100) reflection at second and third hydration-dehydration cycles, and the Bragg reflection of (110) with a  $2\theta$  angle of  $14.38^\circ$  in  $\text{CH}_3\text{NH}_3\text{PbI}_3$  perovskite crystal .

Furthermore, to study the effect of very long exposure (144 hours) of  $\text{CH}_3\text{NH}_3\text{PbI}_3$  perovskite film to 80% humidity, I also performed ex-situ X-ray diffraction measurement on a power diffractometer in Bragg-Brentano geometry. In contrast to the in-situ experiments on the time-scale up to 65 hours, a dihydrate phase with a possible formula of  $(\text{CH}_3\text{NH}_3)_4\text{PbI}_6 \cdot 2\text{H}_2\text{O}$  was formed when exposure to 80% humidity for 6 days (Figure 4.4).

Notably, at the second hydration-dehydration round, the Bragg reflections of monohydrate  $\text{CH}_3\text{NH}_3\text{PbI}_3 \cdot \text{H}_2\text{O}$  appeared after 7 hours when exposed to 80% humidity. The Bragg reflections of  $\text{CH}_3\text{NH}_3\text{PbI}_3 \cdot \text{H}_2\text{O}$  monohydrate appeared around 1.5 hours

later in the second hydration-dehydration round compared to the first and third one which were around 5.5 hours. One possibility for a delay in the formation of a hydrated phase could be the formation of a thin protective skin layer that formed on top of  $\text{CH}_3\text{NH}_3\text{PbI}_3$  film after the first hydration-dehydration process. Such a skin layer could act as a protective layer onto  $\text{CH}_3\text{NH}_3\text{PbI}_3$  film which prevents further penetration of  $\text{H}_2\text{O}$  vapor molecules at the second hydration round [162].

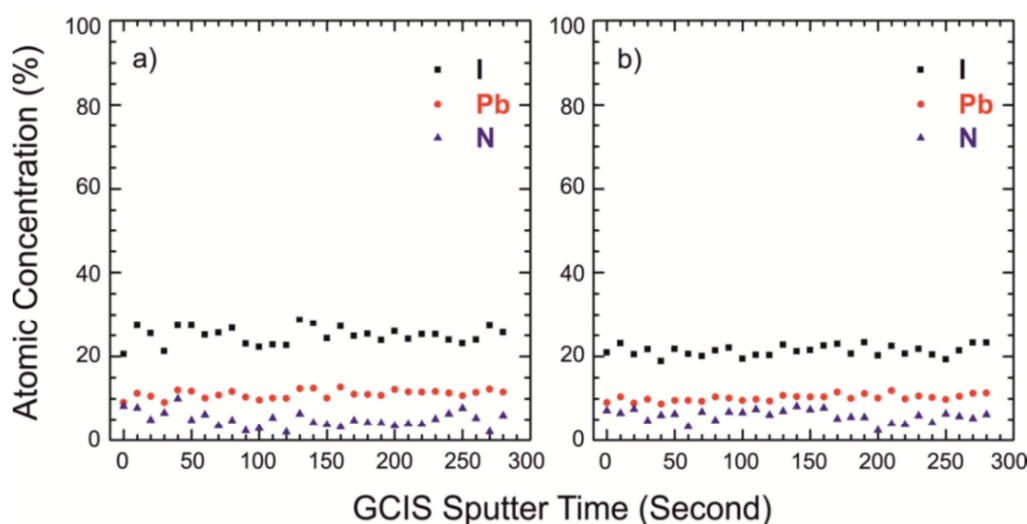


**Figure 4.11:** X-ray photoelectron spectroscopy (XPS) depth profile of (a) reference  $\text{MAPbI}_3$  film and (b) humidity-exposed  $\text{MAPbI}_3$  film for 10 hours on top of PEDOT:PSS/ITO substrates.

In order to probe the possible presence of a skin layer I performed depth profiling X-ray photoelectron spectroscopy (XPS) on both reference and 10 hours' humidity-exposed  $\text{CH}_3\text{NH}_3\text{PbI}_3$  film (Figure 4.11). The depth profiling XPS data revealed almost identical atomic ratios of I/Pb and N/Pb for both reference and humidity-exposed  $\text{CH}_3\text{NH}_3\text{PbI}_3$  films within the error of the measurements. Therefore, I excluded the formation of a skin layer on top of  $\text{CH}_3\text{NH}_3\text{PbI}_3$  film during exposure to humidity.

Based on the findings described above, I proposed a degradation model, which is based on the model outlined previously by Leguy et al. [111]. First water molecules diffused into  $\text{CH}_3\text{NH}_3\text{PbI}_3$  films upon exposure to humidity mostly probably along already existing grain boundaries (Figure 4.12a). In the beginning this neither had an effect on the  $\text{CH}_3\text{NH}_3\text{PbI}_3$  crystal structure nor on the surface morphology. The monohydrate  $\text{CH}_3\text{NH}_3\text{PbI}_3 \cdot \text{H}_2\text{O}$  could only form after a prolonged exposure time to an environment of humidity above 50%. Once the monohydrate phase formed, additional steps and grain boundaries appeared on the  $\text{CH}_3\text{NH}_3\text{PbI}_3$  films, which induced a rougher surface (Figure 4.12b, the monohydrate phase is sketched in a light blue color).

At later stages, more and more grain boundaries were observed by in-situ SFM for continuing exposure to humidity (Figure 4.12c).

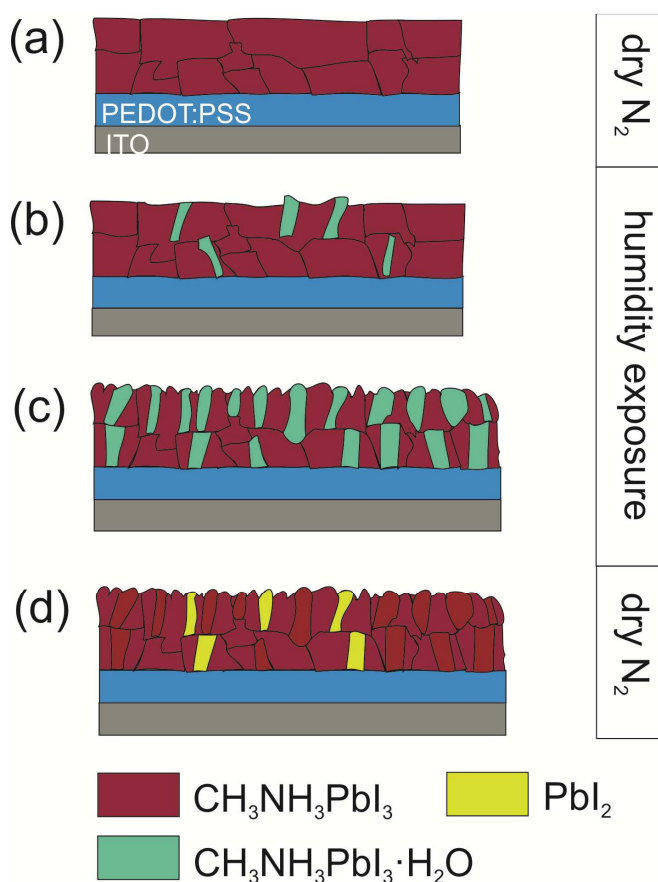


**Figure 4.12:** Proposed degradation model of  $\text{CH}_3\text{NH}_3\text{PbI}_3$  perovskite films prepared on top of a PEDOT:PSS coated ITO substrate<sup>32</sup> at microscopic scale under humidity exposure (80%) and dry  $\text{N}_2$  gas flushing. Grain boundaries in the  $\text{CH}_3\text{NH}_3\text{PbI}_3$  phase are indicated with black lines. The square on the right side of the scheme shows the experimental atmospheres (80% humidity and dry  $\text{N}_2$ ) in our measurements.

Accordingly, the intensity of monohydrate  $\text{CH}_3\text{NH}_3\text{PbI}_3 \cdot \text{H}_2\text{O}$  Bragg reflections increased. Under a dry atmosphere in-situ XRD measurements showed that the monohydrate  $\text{CH}_3\text{NH}_3\text{PbI}_3 \cdot \text{H}_2\text{O}$  converted back to  $\text{CH}_3\text{NH}_3\text{PbI}_3$  again. However, the grain boundaries persisted. After longer humidity exposure for 65 hours,  $\text{PbI}_2$  was detected during the following dehydration process under dry atmosphere (Figure 4.12d,  $\text{PbI}_2$  crystals is sketched in yellow color). Furthermore, after dehydration the peak intensity of  $\text{CH}_3\text{NH}_3\text{PbI}_3$  at (110) reflection did not return to its initial intensity value. This observation might be explained by a partially irreversible degradation of  $\text{CH}_3\text{NH}_3\text{PbI}_3$  films that led to the formation of  $\text{PbI}_2$ .

## 4.4 Summary and conclusion

The measurements in this chapter confirmed the formation of monohydrate  $\text{CH}_3\text{NH}_3\text{PbI}_3 \cdot \text{H}_2\text{O}$  under high humidity environment (80%), which was reversible under dry  $\text{N}_2$  flushing. The results were consistent with the reports on reversibility between perovskite phase and hydrated phase during humidity-induced degradation process [103, 111]. However, the measurements did not exhibit that degradation primarily started from or along the grain boundaries as proposed by Leguy et al. [111]. In particular, I found irreversible morphology features such as grain boundaries and steps which persisted after drying the  $\text{CH}_3\text{NH}_3\text{PbI}_3$  film overnight. The presence of grain boundaries could limit the charge transport [163] and act as recombination centers [115, 163, 164]. Quillettes et al. claimed the grain boundaries exhibited faster non-radiative decay which decreases the device performance [165].

Therefore, I assumed the presence of these grain boundaries was most likely the reason for an increase in hysteresis upon humidity exposure that was measured by Leguy et al. [111]. This interpretation is consistent with the finding that a decrease in crystal size leads to an increasing hysteresis [112]. Interestingly I noticed that morphological changes could not be observed for exposure to humidity  $\leq 50\%$  for a duration of 144 h. Thus passivation layers which are able to keep the humidity in devices below this value could be very beneficial for device performance.

# Chapter 5

## Photo-oxidation of PCBM films

### 5.1 Introduction

Up to now, the fullerene derivative [6,6]-phenyl-C<sub>61</sub>-butyric acid methyl ester (PCBM) is a widely used and well investigated electron acceptor material in polymer: fullerene based solar cells. However, the lifetime of polymer solar cells is still an obstacle for the successful commercialization of this technology. The important factors that limit their lifetime are chemical degradation with light, humidity and oxygen [16, 17, 23, 41, 57,] and physical degradation [16]. As a mostly studied electron acceptor material in polymer solar cells, it is quite important to investigate the chemical degradation pathways of PCBM material when exposed to light, humidity and oxygen. By using photoelectron spectroscopy, Bao et al. reported the effects of in-situ oxygen exposure on energetics of PCBM films [57]. The results showed that oxygen-induced degradation was reversible by thermal treatment in vacuum which implied a weak interaction between oxygen and PCBM [57].

However, Reese et al. reported a strong interaction between oxygen and C<sub>60</sub> moiety in PCBM, which implied an irreversible oxygen-induced degradation of PCBM molecules [23]. The fullerene moiety in PCBM was found to undergo series of oxidations which decreased the photoconductivity of PCBM material [23]. In 2012, Matsuo et al. reported that a photooxidized fullerene derivative-contained bulk heterojunction organic solar cells exhibited poor power conversion efficiency than the solar cells with non-oxidized fullerene derivative [166]. This phenomenon implies that oxidized fullerene derivatives can degrade device performance in organic solar cells. The possible structures of these ions during degradation process are described on Figure 5.1. Even though, it is necessary to investigate the photo-oxidation mechanism of PCBM acceptor materials.



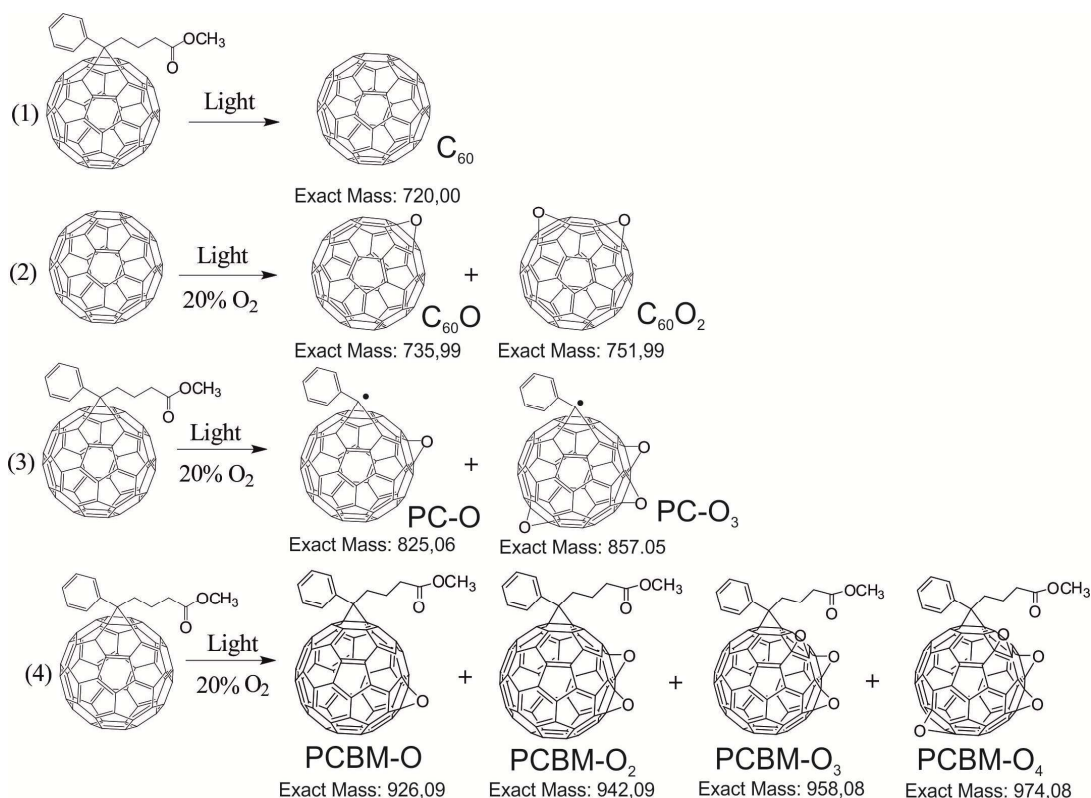


**Figure 5.1:** The possible structures of degraded PCBM with adsorbed one oxygen atoms, two oxygen atoms or one oxygen molecule during photo-degradation process in 20% atmosphere.

The physical degradation usually refers to the morphological degradation of active films in polymer solar cells. The SFM technique is very sensitive to film surface information and can be used to observe the morphology changes during degradation process [16]. As shown in Figure 5.2, the thickness changes of PCBM film is presented as a function of degradation time and photo doses in a synthetic gas environment (20% O<sub>2</sub> and 80% N<sub>2</sub>). When the PCBM film was illuminated below a photo dose 15 kJ/cm<sup>2</sup> (20 hours at 2 Sun intensity), there was no topography difference between illuminated and non-illuminated areas (Figure 5.2a). Here, a cross-shaped mask was used to protect part of PCBM film as non-illuminated area, and the exposed parts as illuminated area (Figure 5.2b) [120]. When further increasing the illumination photo dose > 20 kJ/cm<sup>2</sup>, the thickness of illuminated PCBM increased relative to the non-illuminated area. When the illuminated photo dose increased to 25.2 kJ/cm<sup>2</sup>, the thickness difference between illuminated and non-illuminated area reached 18 ± 3 nm. When further illuminating PCBM film for 45 hours at 2 Sun intensity with the photo dose of 32.4 kJ/cm<sup>2</sup>, the thickness of the illuminated PCBM part showed a slight decrease of 16 ± 3 nm by drawing a line profile along the SFM image (Figure 5.2b and 5.2c). These results indicated that the film thickness of illuminated area only increased



at photo doses  $>20 \text{ kJ/cm}^2$  under an oxygen environment. Below this photo dose, no topography changes were detectable [120].

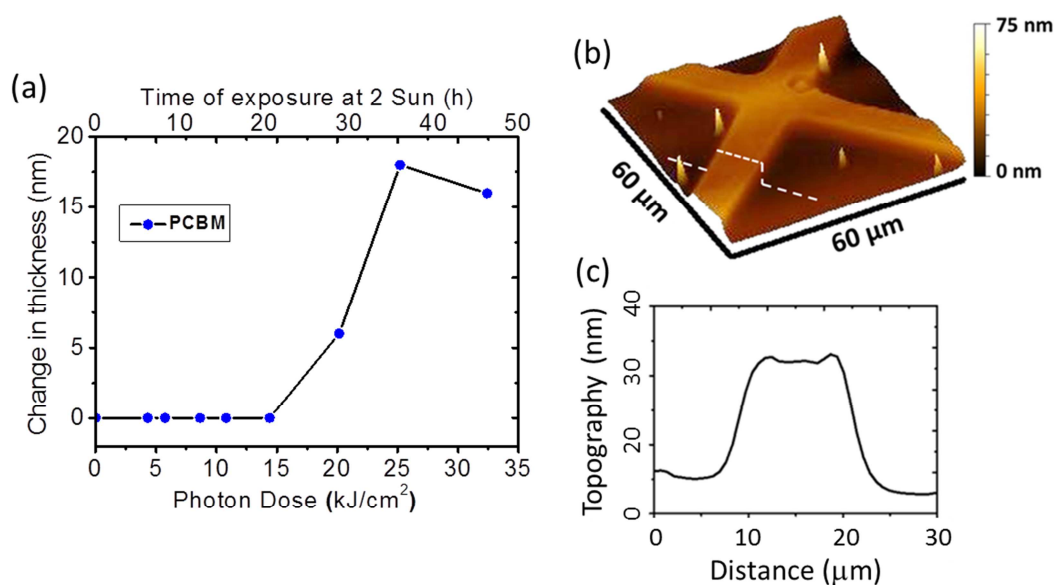


**Figure 5.2:** (a) Thickness changes of PCBM films for different degradation time and exposure photo doses, (b) the SFM image of a locally degraded PCBM film in controlled atmosphere (20% O<sub>2</sub> and 80% N<sub>2</sub>) at 2 Sun intensity for 45 hours, (c) the corresponding profile between degraded and non-degraded areas along the white dotted line in SFM image (From Dr. Esha Sengupta's dissertation [120]).

Furthermore, the Kelvin probe force microscopy (KPFM) and photo-conductive scanning force microscopy (c-SFM) were performed by Sengupta et al. on the P3HT:PCBM samples under different degradation conditions [16]. Their report indicated no topography changes under illumination in the absence of oxygen [16]. In summary, the SFM results indicated that possible chemical reactions occurred between PCBM and oxygen molecules, which caused the thickness changes of PCBM films under photo-oxidation [168, 169]. The dimerization process of PCBM molecules upon illumination in absence of oxygen were also reported to be responsible for the degradation of device performance [58, 61, 170].

However, SFM technique is only sensitive to film surface information and cannot obtain specific information on the degradation species. Additionally, matrix-assisted laser desorption/ionization time of flight mass spectrometry (MALDI-TOF MS) is one of the most powerful approaches to identify the amounts of analyte products because of its high sensitivity and high mass/charge resolution. Therefore, in order to complement the SFM results about film morphology, I further utilized MALDI-TOF MS method to elucidate the possible degradation products during photo-oxidation process. Here, the

PCBM films were stored in a controlled atmosphere, synthetic gas containing 20% O<sub>2</sub> and 80% N<sub>2</sub> (Figure 5.3). Then the non-degraded and degraded PCBM films were characterized by using MALDI-TOF MS to track the degradation products in detail.

## 5.2 Experimental section

### 5.2.1 Film preparation

PCBM material was purchased from Sigma-Aldrich and used as received without further purification. PCBM has electronic grade of > 90%. The PCBM solutions were made by dissolving PCBM powder into o-dichlorobenzene at a weight 2% and stirred overnight at 90 °C on a hotplate inside N<sub>2</sub>-filled glovebox. The solutions were filtered with a Millipore filter with a pore size of 0.45 μm in order to remove any undissolved particles. PCBM films were prepared by depositing PCBM solution onto pre-cleaned ITO substrates, and spin-coated at a speed of 500 rpm for 360 s inside N<sub>2</sub>-filled glovebox. Then the PCBM films were put onto a hotplate and did thermal annealing at 140 °C for 5 min.

### 5.2.2 Degradation procedures of PCBM films

In order to make degraded PCBM films for MALDI-TOF experiments, the fresh prepared PCBM films were taken out from glovebox for photo-degradation. The PCBM films were built into an in-house made atmospheric chamber which was filled with synthetic air (20% O<sub>2</sub> and 80% N<sub>2</sub>) (Figure 5.3). The PCBM films were illuminated at 1 sun from solar simulator at AM 1.5 G with light intensity 100 mW/cm<sup>2</sup> for different time. During illumination, the temperature of the PCBM films was below 30 °C which could rule out annealing effects due to temperature. The incident light intensities and times were converted into an illumination dose according to the following steps: At 1 sun with an intensity 100 mW/cm<sup>2</sup>, the photo dose is 1 sun = 100 × 10<sup>-3</sup> W/cm<sup>2</sup> = 0.1 J/s·cm<sup>2</sup>. Thus, the photo dose for 1 hour is 0.1 × 3600 s·J/ s·cm<sup>2</sup> = 360 J/cm<sup>2</sup>.

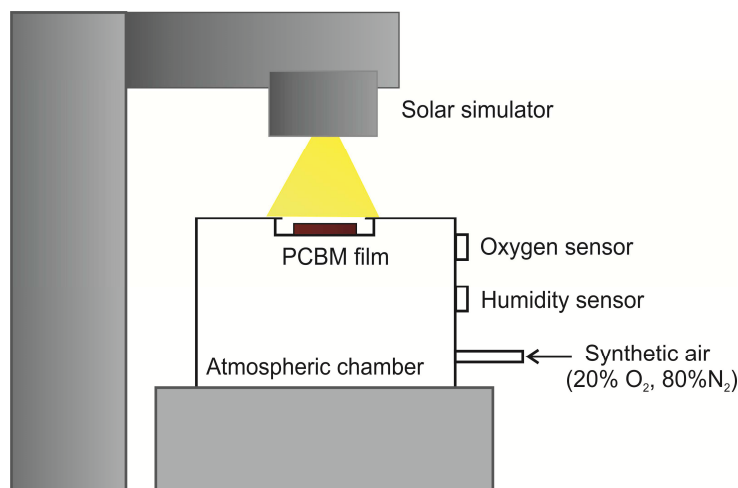


**Figure 5.3:** To degrade PCBM film, they were kept inside one in-house made atmospheric chamber with a controlled oxygen and humidity.

### 5.3 Results and discussion

In MALDI-TOF MS measurements, the selection of an adequate matrix influences the quality of the mass spectra [134]. The matrix *trans*-2-[3-(4-*tert*-Butylphenyl)-2-methyl-2-propenylidene] malononitrile (DCTB) is an excellent matrix for the analysis of fullerene derivatives by MALDI-TOF [134]. DCTB is found to yield the most abundant analyte ion signals with extremely low fragmentation. The molecule structure and its MALDI-TOF MS spectrum is shown in Figure 5.4.

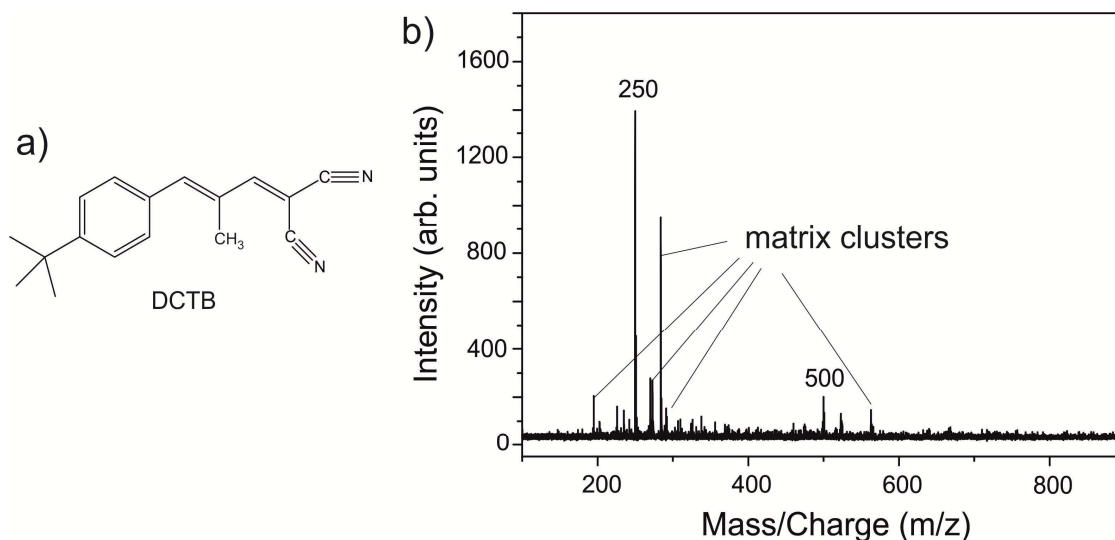


**Figure 5.4:** The molecule structure of DCTB matrix (a) and its corresponding MALDI-TOF MS data in positive ion mode.

The signal centered at  $m/z$  250 and 500 are assigned to  $\text{DCTB}^+$  and DCTB dimer, respectively. The signals of pure DCTB matrix below  $m/z$  500 are mostly contributed to the matrix clusters (Figure 5.4b) [134]. Therefore, the  $m/z$  signals below 500 will not be considered and discussed in the following data analysis of PCBM analyte, because the MALDI-TOF MS spectra below  $m/z$  500 overlap with varieties of matrix ion signals.

As a good matrix for MALDI-TOF MS experiment on the analysis of fullerene derivatives, DCTB has been proven to show good performance in both positive- and negative-ion modes [134, 171]. Furthermore, PCBM is an electron deficient fullerene derivative which allows applying both positive- and negative-ion mode in MALDI-TOF MS experiments. Therefore, I first performed reference MALDI-TOF MS experiment with a pristine PCBM film in positive- and negative-ion mode (Figure 5.5).

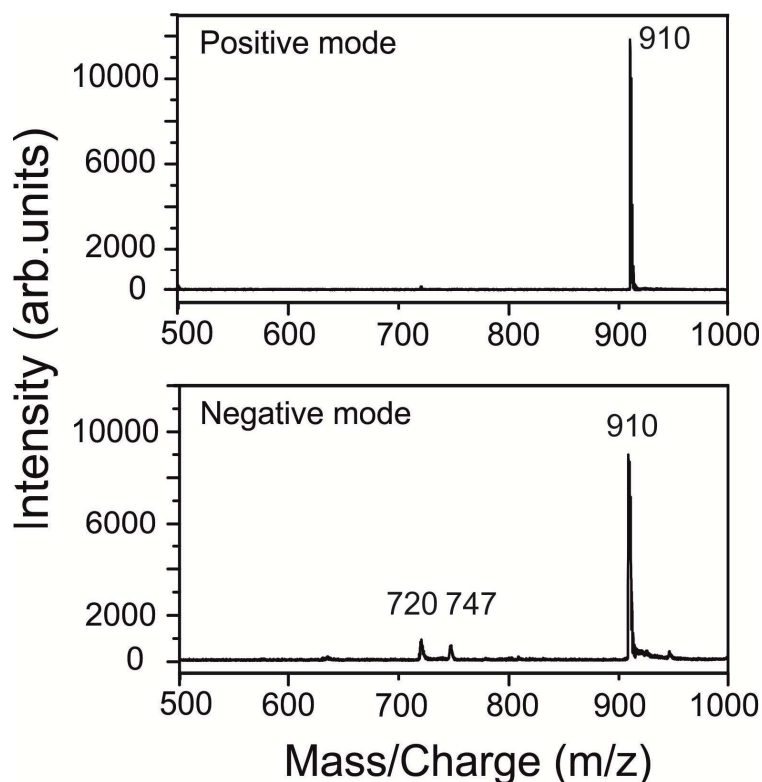


**Figure 5.5:** The MALDI-TOF mass spectra of pristine PCBM film in positive mode (a) and the negative mode (b).

Here, PCBM material was obtained by scratching off the PCBM film from ITO-coated glass substrate. The spectrum below  $m/z$  500 was cut due to the overlap with DCTB matrix clusters. The MALDI-TOF MS spectra revealed that PCBM molecular ion peak centered at  $m/z$  910 which corresponded to the pristine PCBM materials itself. In negative-ion mode MALDI-TOF MS, the ion signals centered at  $m/z$  720 and 747 were assigned to the  $\text{C}_{60}$  fullerene moiety ( $\text{C}_{60}^-$ ) and  $\text{C}_{62}\text{H}_3^-$  fragments [134].  $\text{C}_{60}^-$  is a

common fragment ion in both positive- and negative-ion modes which might be accompanied by low abundant  $C_{62}$  fragments [134]. Additionally, the PCBM molecule contains a bulky conjugated structure which prefers to form radical ions including cations or anions.

### 5.3.1 Positive-ion mode MALDI-TOF MS

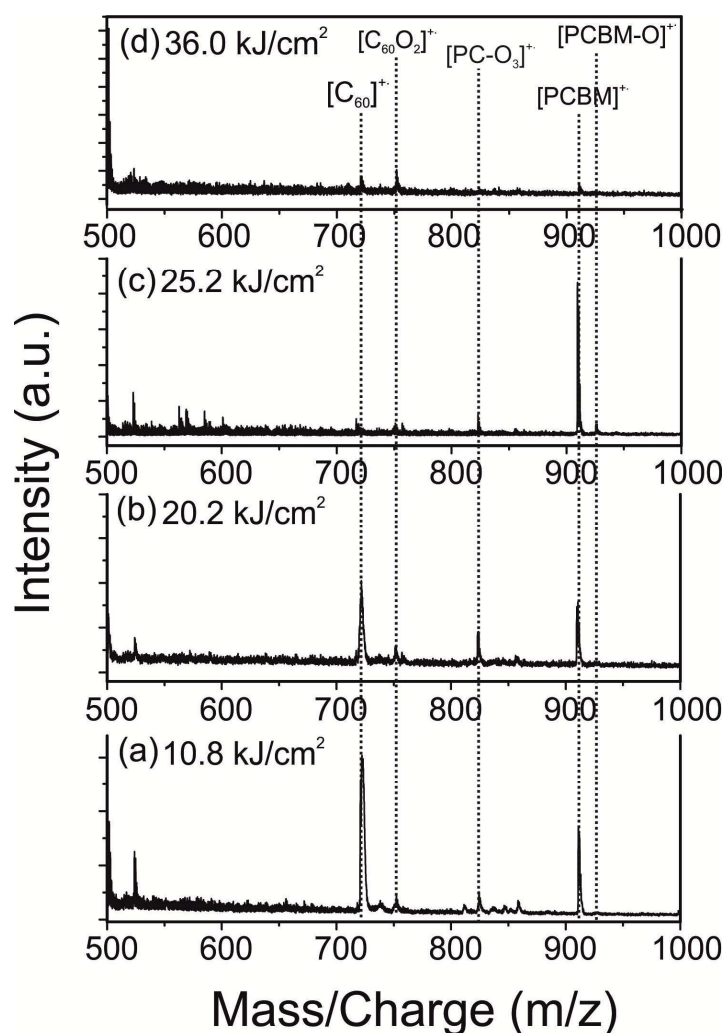


**Figure 5.6:** Positive ion mode MALDI-TOF MS mass spectrum of degraded PCBM films at different photo doses: (a)  $10.8 \text{ kJ/cm}^2$ , (b)  $20.2 \text{ kJ/cm}^2$ , (c)  $25.2 \text{ kJ/cm}^2$  and (d)  $36.0 \text{ kJ/cm}^2$ .

Compared to the MALDI-TOF MS data of the pristine PCBM film (non-degraded) and the pure DCTB matrix, the MALDI-TOF MS mass spectrum of degraded PCBM materials showed new additional ion signals after photo-degradation (Figure 5.6). Besides the signals at  $m/z$  910 and 720 indicating PCBM molecular and  $C_{60}^+$ , the positive-ion MALDI-TOF mass spectra also showed new ion signals locating at  $m/z$  of 752 and 823.

The ion signal with  $m/z$  752 might be caused by the oxidation of  $C_{60}$  fullerene moiety during the photo-oxidation process of PCBM film. At first, photo-illumination might induce the formation of  $C_{60}$  ions by losing the side chains of PCBM molecules. Then the  $C_{60}$  ions were oxidized in the 20%  $O_2$  atmosphere during photo-illumination process. The formation of  $C_{60}O_2^+$  showed ion signal located at  $m/z$  of 752 in MALDI-TOF MS experiments [134]. The possible structure  $C_{60}O_2^+$  is described in Figure 5.1.

The ion signal at  $m/z = 823$  indicated another possible fragment  $[PC-O]^+$  which meant losing the butyric acid methyl ester from PCBM structure, then adding one oxygen atom in the fullerene moiety (as shown in Figure 5.1). When the illumination dose was increased to  $25.2 \text{ kJ/cm}^2$ , the positive-ion mode MALDI-TOF MS mass spectrum showed new ion signal centered at  $m/z$  of 926 which indicated the formation of oxidized PCBM ion  $[PCBM-O]^+$  with one oxygen atom onto fullerene moiety (Figure 5.6c). The possible structures of  $[PCBM-O]$  oxidations are shown in Figure 5.1. However, when further increasing the illumination dose to  $36.0 \text{ kJ/cm}^2$ , the ion signal at  $m/z$  926 disappeared (Figure 5.6d). This phenomenon implied the decomposition of PCBM oxidations at high illumination dose.

Except for positive-ion mode MALDI-TOF MS, PCBM material also allows ion detection by using negative-ion mode. The reason is that PCBM is an electron deficient compound due to the  $C_{60}$  fullerene structure which can easily take up one electron and become PCBM negative ions. Therefore, I also performed negative-ion mode MALDI-TOF MS of degraded PCBM films using DCTB matrix.

### 5.3.2 Negative-ion mode MALDI-TOF MS

Negative-ion mode MALDI-TOF MS was carried to investigate the chemical changes of photo-oxidized PCBM films (Figure 5.7). The ion signal centered at  $m/z = 910$  corresponds to the pristine PCBM analyte. The ion signals located at  $m/z$  720, 736 and 748 indicate the formation of  $C_{60}^-$ ,  $C_{60}O^-$  and  $C_{60}CO^-$ , respectively. Additional ion signals were also detected in the negative-ion mode MALDI-TOF MS experiment. After degradation at an illumination dose of  $10.8 \text{ kJ/cm}^2$ , the photo-oxidized PCBM products were observed with a significant amount of remaining PCBM materials. The MALDI-TOF mass spectrum showed additional ion signals centered at 926  $m/z$ , 942  $m/z$ , 958  $m/z$  and 974  $m/z$  (Figure 5.7a). These ion signals corresponded to oxidized PCBM compounds ( $910+16n$ ) and every neighboring peak was spaced by 16 mass units. Here  $n$  means the number of oxygen atoms attached to PCBM molecular structure. Therefore, these MALDI-TOF MS signals correspond to the oxidized PCBM with up to four oxygen atoms per molecule, such as PCBM-O, PCBM-O<sub>2</sub>, PCBM-O<sub>3</sub> and PCBM-O<sub>4</sub> (Figure 5.1). Higher oxidation states were not detected. In addition, each subsequent

PCBM oxidation product had a weaker MALDI-TOF intensity which indicated the oxygen atoms attacked PCBM structure step by step. This phenomenon implied that only one oxygen atom attached to PCBM molecule at each time during the photo-oxidation process.

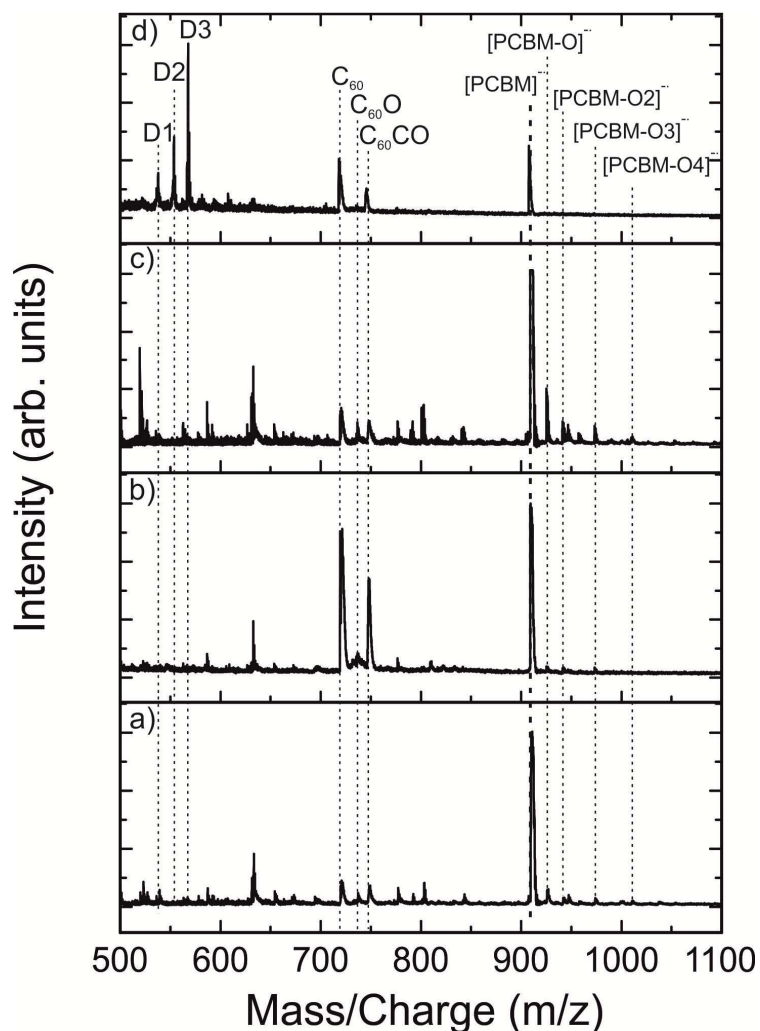


**Figure 5.7:** MALDI-TOF MS mass spectra in negative-ion mode of PCBM films photo-degraded at different illumination dose in 20% O<sub>2</sub> environment, (a) 10.8 kJ/cm<sup>2</sup>, (b) 20.2 kJ/cm<sup>2</sup>, (c) 25.2 kJ/cm<sup>2</sup> and (d) 36.0 kJ/cm<sup>2</sup>. DCTB was used as the matrix.

When the degradation photo dose increased to 20.2 kJ/cm<sup>2</sup>, the SFM results showed a thickness increase of the photo-degraded PCBM film of 6% as shown in Figure 5.2a. But qualitatively, the MALDI-TOF mass spectrum at 20.2 kJ/cm<sup>2</sup> was similar to spectrum at illumination dose of 10.8 kJ/cm<sup>2</sup> and did not exhibit additional new ion signals (Figure 5.7b). Further increasing the illumination dose to 25.2 kJ/cm<sup>2</sup> did not cause more new ion signals as well (Figure 5.7c).



The bonding reaction between oxygen and C<sub>60</sub> moiety is still under debate. Bao *et al.* revealed that there is no chemical bonding between oxygen and C<sub>60</sub> cage when exposed PCBM sample to oxygen environment by performing X-ray photo-electron spectroscopy (XPS) [57]. However, by combining the mobility measurement and MALDI-TOF experiment, Reese *et al.* reported that the chemisorption of atomic oxygen to C<sub>60</sub> cage could be an important deteriorate pathway for organic solar cells [23]. Brumboiu *et al.* investigated the interaction between oxygen atoms and the C<sub>60</sub> molecular moiety of PCBM by using O1s XPS and near-edge x-ray absorption fine structure (NEXAFS) [167]. They suggested two different possible sites for oxygen absorption on C<sub>60</sub> moiety, oxygen adsorption onto 6-6 sites (between two neighboring hexagons) and onto 5-6 sites (between a pentagon and a hexagon). However, the detailed oxidation mechanism of PCBM molecules is still under investigation and beyond the scope of this thesis.

However, when the illumination dose was further increased to 36.0 kJ/cm<sup>2</sup>, the ion signals centered at m/z 926, 942, 958 and 974 were not detectable in the MALDI-TOF MS mass spectrum. But new ion signals were observed at around m/z 538 m/z, 554 and 568 (Figure 5.7d), which were not detectable in the MALDI-TOF measurements at lower illumination doses or the reference measurements for DCTB matrix and non-degraded PCBM film. This supplied important information that the PCBM oxidation products could be fragmented into small pieces with low m/z values upon high illumination dose. The highest illumination dose was 36.0 kJ/cm<sup>2</sup> used in this study. The ion signals at m/z 538, 554 and 568 were assigned to the PCBM fragmentations in which the oxidized fullerene moiety was broken. The possible structures for these fragmentations are outlined in Figure 5.8.

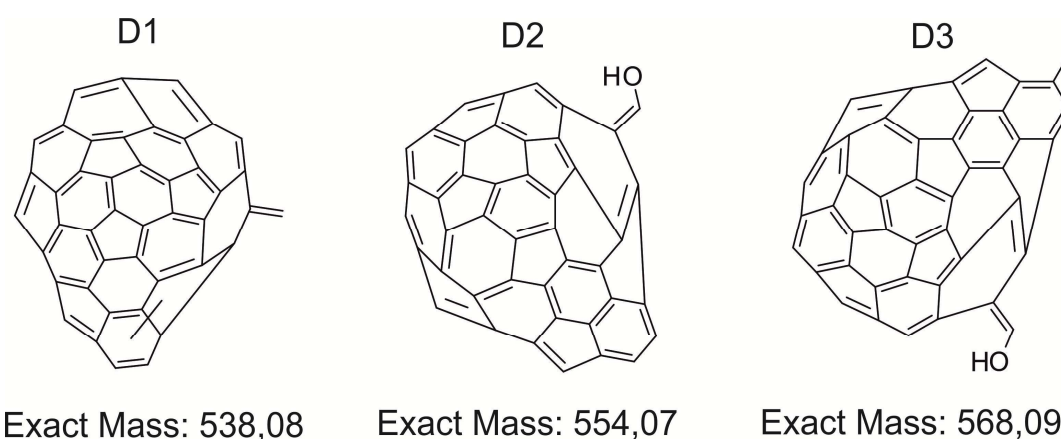


**Figure 5.8:** Possible structures of PCBM fragments due to the decomposition of PCBM oxidations at higher photo dose (36.0 kJ/cm<sup>2</sup>) during photo-degradation in 20% O<sub>2</sub> atmosphere.



In addition, several studies reported a light-induced dimerization of PCBM molecules under inert atmosphere during photo-degradation process [58-61]. However, we did not observe the ion signal locating at 1820 m/z at all illuminated photo doses which would correspond to the PCBM dimer. In our experiments, the photo-degradation of PCBM in 20% O<sub>2</sub> atmosphere formed PCBM oxidations at first and then fragmentations, without PCBM dimerization. According to the literatures, the PCBM dimers only formed under illumination in an inert environment without oxygen present [60, 172]. In the oxygen-filled environment, the oxygen might quench the PCBM triplet state, which could stabilize the PCBM molecules against photo-dimerization [173].

The above findings from MALDI-TOF MA measurements are related to SFM results from Dr. Sengupta in Figure 5.2 [120]. The SFM results showed a maximum thickness increase when the photo-oxidation of PCBM film under illumination dose of 25.2 kJ/cm<sup>2</sup>. When the illumination dose > 25.2 kJ/cm<sup>2</sup>, the film thickness of photo-degraded PCBM film slightly decreased from its maximum value (Figure 5.2). This phenomenon implies that the formation of PCBM oxidation products might introduce additional stress to the whole PCBM films causing a film swelling and film thickness increase. Combined with MALDI-TOF MS measurements, it indicated that the formation of oxidized PCBM products could cause an increase in film thickness. Furthermore, the decomposition of PCBM oxidations under high illumination dose and the elimination of PCBM oxidation could lead to a decrease of film thickness.

## 5.4 Summary and conclusion

According to the SFM results and combined with MALDI-TOF MS mass spectra both in positive- and negative-ion mode, I conclude that pristine PCBM molecules are first been oxidized and second fragmented under photo-illumination at 20% O<sub>2</sub> atmosphere. As shown in Figure 5.9a, the pristine PCBM films onto ITO-coated substrates were attached to the atmospheric chamber using magnet. The photo-degradation of PCBM films in the present of oxygen includes two following steps.

### First step:

The MALDI-TOF MS mass spectra revealed that the oxidation of PCBM molecules already occurred when illuminated at a low photo dose of 10.8 kJ/cm<sup>2</sup>. Ion signals corresponding to PCBM oxidations (PCBM+16×n, n=1-4) were observed in the photo-degraded PCBM films in negative-ion mode MALDI-TOF MS mass spectra, which indicated up to 4 oxygens present in the PCBM oxidations. However, the SFM results did not show any thickness changes at this illumination dose between degraded and

non-degraded PCBM areas. It demonstrated that PCBM oxidation products were in the minority at low illumination dose. The small amount of PCBM oxidations could not affect the volume of the whole PCBM films. Upon further increasing the photo dose of illumination ( $20.2 \text{ kJ/cm}^2$  and  $25.2 \text{ kJ/cm}^2$ ) during photo-degradation process, the MALDI-TOF MS mass spectra showed stronger intensity of PCBM oxidation ions, indicating more and more PCBM oxidations were formed at 20%  $\text{O}_2$  atmosphere. The large amount of PCBM oxidations could lead to a critical stress value in the degraded PCBM films, which led to a delamination and blistering. The stronger blistering effect could swell the whole film resulting in an increase in film thickness (Figure 5.9b).

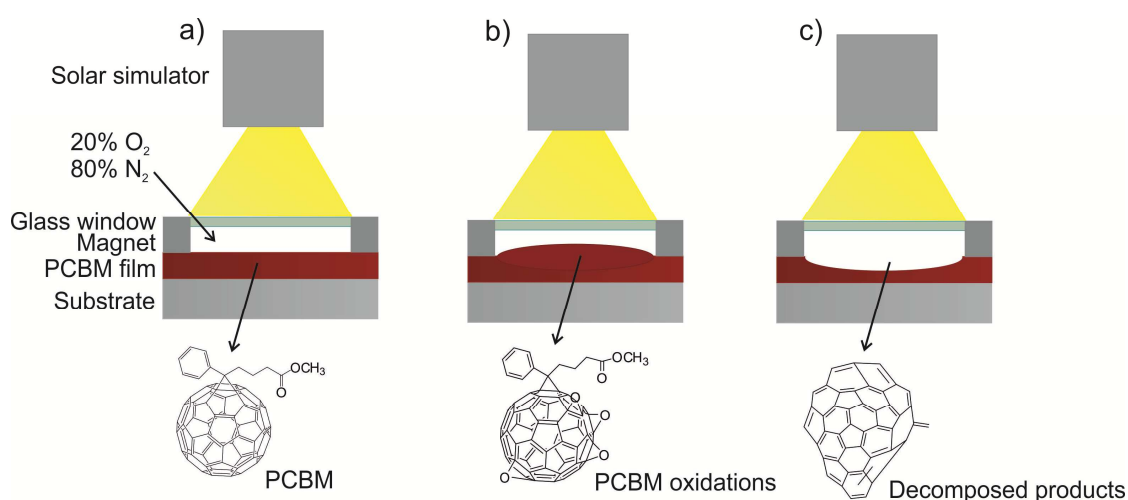


**Figure 5.9:** Schematic of the photo-degradation process inside pristine PCBM films. (a) The non-degraded PCBM film and the corresponding structure of PCBM molecule. (b) The formation of PCBM oxidations during photo-degradation led to a swelling of film thickness. (c) Higher illuminated photo dose decomposed PCBM oxidations into decomposed products resulting in a decrease in film thickness.

### Second step:

With the blistering of PCBM films under photo-degradation, the film thickness change reached a maximum value at a photo dose of  $25.2 \text{ kJ/cm}^2$ . But further increasing the photo dose to  $36.0 \text{ kJ/cm}^2$  did not lead to larger thickness change, but a decrease in film thickness (Figure 5.1 and 5.9c). The reason for this might be that the blistering reached a maximum value and collapsed afterwards, or the PCBM oxidations were not stable under high illuminated photo dose. The PCBM oxidations could decompose into fragmented species, such as the fragments with  $m/z$  centered at 538, 554 and 568. The evaporation of the fragmented species led to a decrease in PCBM film thickness at high photo dose.

In conclusion, the photo-oxidation of PCBM materials and the decompositions of PCBM oxidations could significantly change the surface morphology and thickness of PCBM films. Because of the widely used of PCBM in solution-processed photovoltaic cells, our findings might have significant implications for device performance and device lifetime of PCBM-based photovoltaic cells. Furthermore, it is essential to investigate the photo-oxidation and photo-decomposition of PCBM materials in complete devices under operating conditions. Another approach is to replace PCBM materials with other photovoltaic materials with higher photo-stability.



# Chapter 6

## Concluding remarks and Outlook

In my thesis, I investigated the crystallization, humidity-induced degradation of perovskite solar cell materials and the photo-degradation of organic solar cell materials. Numerous techniques have been applied in my thesis, such as SFM, MALDI-TOF MS, UV-vis absorption spectroscopy, X-ray diffraction. With these techniques, I could precisely measure the morphology changes, chemical changes and crystal structure changes during degradation and crystallization processes. Furthermore, the degradation mechanisms of organic solar materials and perovskite solar materials are detailed investigated and clarified in the thesis.

The first part of my thesis focused on the commonly used perovskite solar cell materials  $\text{CH}_3\text{NH}_3\text{PbI}_3$  and the work was separated into two subparts. The first subpart was about the crystallization of  $\text{CH}_3\text{NH}_3\text{PbI}_3$  perovskite films during thermal annealing under an inert environment. SFM is suitable for heating samples in-situ combined with a high temperature heater stage, which allowed local observation of film crystallization at different heating temperatures and times. I could conclude that the formation of  $\text{CH}_3\text{NH}_3\text{PbI}_3$  occurred above annealing temperature of 70 °C. Furthermore, the  $\text{CH}_3\text{NH}_3\text{PbI}_3$  crystals were not stable at too high annealing temperature (i.e. 120 °C) which led to their decomposition. The studies reveal that annealing temperature plays an important role in the formation of  $\text{CH}_3\text{NH}_3\text{PbI}_3$  films. The quality of  $\text{CH}_3\text{NH}_3\text{PbI}_3$  films is essential for the electrical parameters and device performance.

Currently, I made a detailed study on the morphology changes of  $\text{CH}_3\text{NH}_3\text{PbI}_3$  films during crystallization. Another approach would be to apply in-situ Kelvin Probe Force Microscopy (KPFM) on the cross-section samples during thermal annealing. The observation of cross-section sample gives the information on the film growth on the vertical direction. Furthermore, the measured surface potential from KPFM is related to the device electrical parameters, i.e. open circuit voltage. This method will lead to a further understanding on the effect of annealing temperature and time on the film crystallization and device performance.

The second subpart of perovskite project described the degradation of  $\text{CH}_3\text{NH}_3\text{PbI}_3$  films under humid environment. In detail, in-situ SFM and in-situ XRD were performed to track changes in film morphology and crystal structure during degradation. High

humidity of 80% caused irreversible formation of new steps and grain boundaries on top of  $\text{CH}_3\text{NH}_3\text{PbI}_3$  films, which was most likely the reason for an increase in hysteresis in JV behavior upon humidity exposure. In particular, I could refine the current degradation picture of  $\text{CH}_3\text{NH}_3\text{PbI}_3$  films under humid environment. The findings from the current thesis give us a hint on how to protect perovskite photovoltaic devices. One approach is to keep  $\text{CH}_3\text{NH}_3\text{PbI}_3$ -based perovskite devices under dry environments. Another approach is to encapsulate the perovskite devices with hydrophobic layers. Future experiments would be performed on the complete devices under detrimental environments, i.e. high humidity, photo-illumination. This way, the role of humidity or light on the perovskite films or perovskite/electrode interfaces could be further clarified.

In the second part of the thesis, MALDI-TOF MS was applied to observe the photo-degradation of PCBM films in presence of oxygen. The data showed chemical structure changes of PCBM molecules during photo-oxidation process. PCBM molecules underwent photo-oxidation and photo-decomposition which could significantly change the surface morphology and film thickness. From the investigation of PCBM material degradation under illumination in the presence of oxygen, I conclude that the formation and decomposition of PCBM oxidations influenced not only the film morphology/thickness but also the lifetime of the corresponding PCBM-based photovoltaics. One alternative approach to protect PCBM photovoltaics is to replace PCBM materials with other semiconducting materials with higher photo-stability.

Understanding the crystallization and degradation processes of perovskite solar cell material and degradation of PCBM materials is essential for us to optimize the photovoltaic devices and design more stable photovoltaic for practical applications. Overall, MALDI-TOF MS has been proven to be an efficient method to track chemical structure changes during molecule degradation. SFM is shown to be a unique method to do in-situ investigation on sample morphology at a nanometer scale. X-ray diffraction allows in-situ and ex-situ observation on the crystal structure changes of analytes.

---

# Bibliography

1. (IEA), I. E. A., 2014 Key world energy statistics. *International Energy Agency (IEA)*, **2014**.
2. (UNDP), U. N. D. P., World energy assessment. *United Nations Development Programme (UNDP)*, **2000**. United Nations Department of economic and social affairs.
3. A. E. Becquerel, Recherches sur les effets de la radiation chimique de la lumiere solaire au moyen des courants electriques. *Comptes Rendus de L'Academie des Sciences*, **1839**. 9: p. 145-149.
4. A. E. Becquerel, Memoire sur les effets d'electricques produits sous l'influence des rayons solaires. *Annalen der Physick und Chemie*, **1841**. 54: p. 35-42.
5. C. E. Fritts, On the Fritts selenium cells and batteries. *Van Nostrands Engineering Magazine*, **1885**. 32: p. 388-395.
6. D. M. Chapin, C. S. Fuller, and G. L. Pearson, A New Silicon p-n Junction Photocell for Converting Solar Radiation into Electrical Power. *Journal of Applied Physics*, **1954**. 25(5): p. 676-677.
7. H. Shirakawa, E. J. Louis, A. G. MacDiarmid, C. K. Chiang, and A. J. Heeger, Synthesis of Electrically Conducting Organic Polymers: Halogen Derivatives of Polyacetylene, (CH)<sub>x</sub>. *Journal of the Chemical Society, Chemical Communications*, **1977**. 16: p. 578-580.
8. M. Kaltenbrunner, M. S. White, E. D. Głowacki, T. Sekitani, T. Someya, N. S. Sariciftci, and S. Bauer, Ultrathin and Lightweight Organic Solar Cells with High Flexibility. *Nature Communications*, **2012**. 3: p. 770.
9. Z. A. Page, Y. Liu, V. V. Duzhko, T. P. Russell, and T. Emrick, Fulleropyrrolidine Interlayers: Tailoring Electrodes to Raise Organic Solar Cell Efficiency. *Science*, **2014**. 346(6208): p. 441-444.
10. J.-D. Chen, C. Cui, Y.-Q. Li, L. Zhou, Q.-D. Ou, C. Li, Y. Li, and J.-X. Tang, Single-Junction Polymer Solar Cells Exceeding 10% Power Conversion Efficiency. *Advanced Materials*, **2015**. 27(6): p. 1035-1041.
11. Y. Liu, J. Zhao, Z. Li, C. Mu, W. Ma, H. Hu, K. Jiang, H. Lin, H. Ade, and H. Yan, Aggregation and Morphology Control Enables Multiple Cases of High-efficiency Polymer Solar Cells. *Nature Communications*, **2014**. 5: p. 5293.
12. You, J., L. Dou, K. Yoshimura, T. Kato, K. Ohya, T. Moriarty, K. Emery, C.-C. Chen, J. Gao, G. Li, and Y. Yang, A Polymer Tandem Solar Cell with 10.6% Power Conversion Efficiency. *Nature Communications*, **2013**. 4: p. 1446.

- 
13. G. Li, R. Zhu, and Y. Yang, Polymer Solar Cells. *Nature Photonics*, **2012**. 6(3): p. 153-161.
  14. M. A. Green, K. Emery, Y. Hishikawa, and W. Warta, Solar Cell Efficiency Tables (Version 34). *Progress in Photovoltaics: Research and Applications*, **2009**. 17(5): p. 320-326.
  15. A. Seemann, H. J. Egelhaaf, C. J. Brabec, and J. A. Hauch, Influence of Oxygen on Semi-Transparent Organic Solar Cells with Gas Permeable Electrodes. *Organic Electronics*, **2009**. 10(8): p. 1424-1428.
  16. E. Sengupta, A. L. Domanski, S. A. L. Weber, M. B. Untch, H. J. Butt, T. Sauermann, H. J. Egelhaaf, and R. Berger, Photoinduced Degradation Studies of Organic Solar Cell Materials Using Kelvin Probe Force and Conductive Scanning Force Microscopy. *Journal of Physical Chemistry C*, **2011**. 115(40): p. 19994-20001.
  17. A. Rivaton, S. Chambon, M. Manceau, J. L. Gardette, N. Lamaitre, and S. Guillerez, Light-induced Degradation of the Active Layer of Polymer-based Solar Cells. *Polymer Degradation and Stability*, **2010**. 95(3): p. 278-284.
  18. A. Moujoud, S. H. Oh, J. J. Hye, and H. J. Kim, Improvement in Stability of Poly(3-hexylthiophene-2,5-diyl)/[6,6]-Phenyl-C<sub>61</sub>-butyric Acid Methyl Ester Bulk Heterojunction Solar Cell by Using UV Light Irradiation. *Solar Energy Materials and Solar Cells*, **2011**. 95(4): p. 1037-1041.
  19. U. Dettinger, H.-J. Egelhaaf, C. J. Brabec, F. Latteyer, H. Peisert, and T. Chassé, FTIR Study of the Impact of PC[60]BM on the Photodegradation of the Low Band Gap Polymer PCPDTBT under O<sub>2</sub> Environment. *Chemistry of Materials*, **2015**. 27(7): p. 2299-2308.
  20. H. C. Weerasinghe, S. E. Watkins, N. Duffy, D. J. Jones, and A. D. Scully, Influence of Moisture Out-gassing from Encapsulant Materials on the Lifetime of Organic Solar Cells. *Solar Energy Materials and Solar Cells*, **2015**. 132(0): p. 485-491.
  21. I. Visoly-Fisher, A. Mescheloff, M. Gabay, C. Bounioux, L. Zeiri, M. Sansotera, A. E. Goryachev, A. Braun, Y. Galagan, and E. A. Katz, Concentrated Sunlight for Accelerated Stability Testing of Organic Photovoltaic Materials: Towards Decoupling Light Intensity and Temperature. *Solar Energy Materials and Solar Cells*, **2015**. 134(0): p. 99-107.
  22. S. Chambon, A. Rivaton, J.-L. Gardette, and M. Firon, Photo- and Thermal Degradation of MDMO-PPV:PCBM Blends. *Solar Energy Materials and Solar Cells*, **2007**. 91(5): p. 394-398.
  23. M. O. Reese, A. M. Nardes, B. L. Rupert, R. E. Larsen, D. C. Olson, M. T. Lloyd, S. E. Shaheen, D. S. Ginley, G. Rumbles, and N. Kopidakis, Photoinduced



- 
- Degradation of Polymer and Polymer–Fullerene Active Layers: Experiment and Theory. *Advanced Functional Materials*, **2010**. 20(20): p. 3476-3483.
24. S. R. Scully and M. D. McGehee, Effects of Optical Interference and Energy Transfer on Exciton Diffusion Length Measurements in Organic Semiconductors. *Journal of Applied Physics*, **2006**. 100(3): p. 034907.
  25. D. Kearns, and M. Calvin, Photovoltaic Effect and Photoconductivity in Laminated Organic Systems. *The Journal of Chemical Physics*, **1958**. 29(4): p. 950-951.
  26. C. W. Tang, Two-layer Organic Photovoltaic Cell. *Applied Physics Letters*, **1986**. 48(2): p. 183-185.
  27. G. Yu, J. Gao, J. C. Hummelen, F. Wudl, and A. J. Heeger, Polymer Photovoltaic Cells: Enhanced Efficiencies via a Network of Internal Donor-Acceptor Heterojunctions. *Science*, **1995**. 270(5243): p. 1789-1791.
  28. R. R. Lunt, N. C. Giebink, A. A. Belak, J. B. Benziger, and S. R. Forrest, Exciton Diffusion Lengths of Organic Semiconductor Thin Films Measured by Spectrally Resolved Photoluminescence Quenching. *Journal of Applied Physics*, **2009**. 105(5): p. 053711.
  29. L.-G. Yang, H.-Z. Chen, and M. Wang, Optimal Film Thickness for Exciton Diffusion Length Measurement by Photocurrent Response in Organic Heterostructures. *Thin Solid Films*, **2008**. 516(21): p. 7701-7707.
  30. A. Mishra and P. Bäuerle, Small Molecule Organic Semiconductors on the Move: Promises for Future Solar Energy Technology. *Angewandte Chemie International Edition*, **2012**. 51(9): p. 2020-2067.
  31. Y. Huang, M. Zhang, L. Ye, X. Guo, C. C. Han, Y. Li, and J. Hou, Molecular Energy Level Modulation by Changing the Position of Electron-Donating Side Groups. *Journal of Materials Chemistry*, **2012**. 22(12): p. 5700-5705.
  32. Z. B. Henson, K. Müllen, and G. C. Bazan, Design Strategies for Organic Semiconductors beyond the Molecular Formula. *Nature Chemistry*, **2012**. 4(9): p. 699-704.
  33. S. E. Shaheen, C. J. Brabec, N. S. Sariciftci, F. Padinger, T. Fromherz, and J. C. Hummelen, 2.5% Efficient Organic Plastic Solar Cells. *Applied Physics Letters*, **2001**. 78(6): p. 841.
  34. O. Armbruster, C. Lungenschmied, and S. Bauer, Investigation of Trap States and Mobility in Organic Semiconductor Devices by Dielectric Spectroscopy: Oxygen-doped P3HT:PCBM Solar Cells. *Physical Review B*, **2012**. 86(23): p. 235201.
  35. J. V. Shinar, Z. V.; Kafafi, Z. H., Optical and Electronic Properties of Fullerenes and Fullerene-based Materials. *Marcel Dekker: New York*, **1999**.

- 
36. M. Jørgensen, K. Norrman, and F. C. Krebs, Stability/Degradation of Polymer Solar Cells. *Solar Energy Materials and Solar Cells*, **2008**. 92(7): p. 686-714.
  37. E. A. Katz, S. Gevorgyan, M. S. Orynbayev, and F. C. Krebs, Out-door Testing and Long-term Stability of Plastic Solar Cells. *The European Physical Journal - Applied Physics*, **2006**. 36(03): p. 307-311.
  38. C. J. Schaffer, C. M. Palumbiny, M. A. Niedermeier, C. Jendrzewski, G. Santoro, S. V. Roth, and P. Muller-Buschbaum, A Direct Evidence of Morphological Degradation on a Nanometer Scale in Polymer Solar Cells. *Advanced Materials*, **2013**. 25(46): p. 6760-6764.
  39. K. Kawano, R. Pacios, D. Poplavskyy, J. Nelson, D. D. C. Bradley, and J. R. Durrant, Degradation of Organic Solar Cells due to Air Exposure. *Solar Energy Materials and Solar Cells*, **2006**. 90(20): p. 3520-3530.
  40. Norrman, K., S. A. Gevorgyan, and F. C. Krebs, Water-Induced Degradation of Polymer Solar Cells Studied by H<sub>2</sub><sup>18</sup>O Labeling. *ACS Applied Materials & Interfaces*, **2009**. 1(1): p. 102-112.
  41. H. Hintz, H. J. Egelhaaf, H. Peisert, and T. Chassé, Photo-Oxidation and Ozonization of Poly(3-hexylthiophene) Thin Films as Studied by UV/VIS and Photoelectron Spectroscopy. *Polymer Degradation and Stability*, **2010**. 95(5): p. 818-825.
  42. M. Manceau, A. Rivaton, J. L. Gardette, S. Guillerez, and N. Lemaitre, The Mechanism of Photo- and Thermooxidation of Poly(3-hexylthiophene) (P3HT) Reconsidered. *Polymer Degradation and Stability*, **2009**. 94(6): p. 898-907.
  43. Y. Aoyama, T. Yamanari, N. Ohashi, Y. Shibata, Y. Suzuki, J. Mizukado, H. Suda, and Y. Yoshida, Direct Effect of Partially Photooxidized Poly(3-hexylthiophene) on the Device Characteristics of a Bulk Heterojunction Solar Cell. *Solar Energy Materials and Solar Cells*, **2014**. 120, Part B(0): p. 584-590.
  44. H. W. Kroto, J. R. Heath, S. C. O'Brien, R. F. Curl, and R. E. Smalley, C<sub>60</sub>: Buckminsterfullerene. *Nature*, **1985**. 318(6042): p. 162-163.
  45. R. S. Ruoff, D. S. Tse, R. Malhotra, and D. C. Lorents, Solubility of Fullerene (C<sub>60</sub>) in a Variety of Solvents. *The Journal of Physical Chemistry*, **1993**. 97(13): p. 3379-3383.
  46. J. C. Hummelen, B. W. Knight, F. LePeq, F. Wudl, J. Yao, and C. L. Wilkins, Preparation and Characterization of Fulleroid and Methanofullerene Derivatives. *The Journal of Organic Chemistry*, **1995**. 60(3): p. 532-538.
  47. A. Distler, P. Kutka, T. Sauermann, H.-J. Egelhaaf, D. M. Guldi, D. Di Nuzzo, S. C. J. Meskers, and R. A. J. Janssen, Effect of PCBM on the Photodegradation Kinetics of Polymers for Organic Photovoltaics. *Chemistry of Materials*, **2012**. 24(22): p. 4397-4405.

- 
48. D. F. Kronholm, J. C. Hummelen, and A. B. Sieval, *Higher Fullerenes Useful as Radical Scavengers*. 2010, Google Patents.
  49. Z Markovic. and V. Trajkovic, Biomedical Potential of the Reactive Oxygen Species Generation and Quenching by Fullerenes (C<sub>60</sub>). *Biomaterials*, **2008**. 29(26): p. 3561-3573.
  50. P. Spohn, C. Hirsch, F. Hasler, A. Bruinink, H. F. Krug, and P. Wick, C<sub>60</sub> Fullerene: A Powerful Antioxidant or a Damaging Agent? The Importance of an in-depth Material Characterization Prior to Toxicity Assays. *Environmental Pollution*, **2009**. 157(4): p. 1134-1139.
  51. E. B. Zeynalov, N. S. Allen, and N. I. Salmanova, Radical Scavenging Efficiency of Different Fullerenes C<sub>60</sub>–C<sub>70</sub> and Fullerene Soot. *Polymer Degradation and Stability*, **2009**. 94(8): p. 1183-1189.
  52. E. T. Hoke, I. T. Sachs-Quintana, M. T. Lloyd, I. Kauvar, W. R. Mateker, A. M. Nardes, C. H. Peters, N. Kopidakis, and M. D. McGehee, The Role of Electron Affinity in Determining Whether Fullerenes Catalyze or Inhibit Photooxidation of Polymers for Solar Cells. *Advanced Energy Materials*, **2012**. 2(11): p. 1351-1357.
  53. F. A. Salazar, A. Fedorov, and M. N. Berberan-Santos, A Study of Thermally Activated Delayed Fluorescence in C<sub>60</sub>. *Chemical Physics Letters*, **1997**. 271(4–6): p. 361-366.
  54. F. Prat, R. Stackow, R. Bernstein, W. Qian, Y. Rubin, and C. S. Foote, Triplet-State Properties and Singlet Oxygen Generation in a Homologous Series of Functionalized Fullerene Derivatives. *The Journal of Physical Chemistry A*, **1999**. 103(36): p. 7230-7235.
  55. H. Wang, Y. He, Y. Li, and H. Su, Photophysical and Electronic Properties of Five PCBM-like C<sub>60</sub> Derivatives: Spectral and Quantum Chemical View. *The Journal of Physical Chemistry A*, **2012**. 116(1): p. 255-262.
  56. S Cook., H. Ohkita, Y. Kim, J. J. Benson-Smith, D. D. C. Bradley, and J. R. Durrant, A Photophysical Study of PCBM Thin Films. *Chemical Physics Letters*, **2007**. 445(4–6): p. 276-280.
  57. Q. Bao, X. Liu, S. Braun, and M. Fahlman, Oxygen- and Water-Based Degradation in [6,6]-Phenyl-C<sub>61</sub>-Butyric Acid Methyl Ester (PCBM) Films. *Advanced Energy Materials*, **2014**. 4(6): p. 1301272.
  58. A. Distler, T. Sauermann, H.-J. Egelhaaf, S. Rodman, D. Waller, K.-S. Cheon, M. Lee, and D. M. Guldi, The Effect of PCBM Dimerization on the Performance of Bulk Heterojunction Solar Cells. *Advanced Energy Materials*, **2014**. 4(1): p. 1300693.

- 
59. F. Piersimoni, G. Degutis, S. Bertho, K. Vandewal, D. Spoltore, T. Vangerven, J. Drijkoningen, M. K. Van Bael, A. Hardy, J. D'Haen, W. Maes, D. Vanderzande, M. Nesladek, and J. Manca, Influence of Fullerene Photodimerization on the PCBM Crystallization in Polymer: Fullerene Bulk Heterojunctions under Thermal Stress. *Journal of Polymer Science Part B: Polymer Physics*, **2013**. 51(16): p. 1209-1214.
60. A. Dzwilewski, T. Wågberg, and L. Edman, Photo-Induced and Resist-Free Imprint Patterning of Fullerene Materials for Use in Functional Electronics. *Journal of the American Chemical Society*, **2009**. 131(11): p. 4006-4011.
61. J. Wang, J. Enevold, and L. Edman, Photochemical Transformation of Fullerenes. *Advanced Functional Materials*, **2013**. 23(25): p. 3220-3225.
62. Z. Li, H. C. Wong, Z. Huang, H. Zhong, C. H. Tan, W. C. Tsoi, J. S. Kim, J. R. Durrant, and J. T. Cabral, Performance Enhancement of Fullerene-based Solar Cells by Light Processing. *Nature Communications*, **2013**. 4: p. 2227.
63. H. C. Wong, Z. Li, C. H. Tan, H. Zhong, Z. Huang, H. Bronstein, I. McCulloch, J. T. Cabral, and J. R. Durrant, Morphological Stability and Performance of Polymer–Fullerene Solar Cells under Thermal Stress: The Impact of Photoinduced PC<sub>60</sub>BM Oligomerization. *ACS Nano*, **2014**. 8(2): p. 1297-1308.
64. M. Grätzel, The Light and Shade of Perovskite Solar Cells. *Nature Materials*, **2014**. 13(9): p. 838-842.
65. T. Baikie, Y. Fang, J. M. Kadro, M. Schreyer, F. Wei, S. G. Mhaisalkar, M. Graetzel, and T. J. White, Synthesis and Crystal Chemistry of the Hybrid Perovskite CH<sub>3</sub>NH<sub>3</sub>PbI<sub>3</sub> for Solid-State Sensitised Solar Cell Applications. *Journal of Materials Chemistry A*, **2013**. 1(18): p. 5628-5641.
66. C. S. Ponseca, T. J. Savenije, M. Abdellah, K. Zheng, A. Yartsev, T. Pascher, T. Harlang, P. Chabera, T. Pullerits, A. Stepanov, J.-P. Wolf, and V. Sundström, Organometal Halide Perovskite Solar Cell Materials Rationalized: Ultrafast Charge Generation, High and Microsecond-Long Balanced Mobilities, and Slow Recombination. *Journal of the American Chemical Society*, **2014**. 136(14): p. 5189-5192.
67. C. Wehrenfennig, G. E. Eperon, M. B. Johnston, H. J. Snaith, and L. M. Herz, High Charge Carrier Mobilities and Lifetimes in Organolead Trihalide Perovskites. *Advanced Materials*, **2014**. 26(10): p. 1584-1589.
68. S. D. Stranks, G. E. Eperon, G. Grancini, C. Menelaou, M. J. P. Alcocer, T. Leijtens, L. M. Herz, A. Petrozza, and H. J. Snaith, Electron-Hole Diffusion Lengths Exceeding 1 Micrometer in an Organometal Trihalide Perovskite Absorber. *Science*, **2013**. 342(6156): p. 341-344.

- 
69. A. Kojima, K. Teshima, Y. Shirai, and T. Miyasaka, Organometal Halide Perovskites as Visible-Light Sensitizers for Photovoltaic Cells. *Journal of the American Chemical Society*, **2009**. *131*(17): p. 6050-6051.
  70. L. Kazmerski, Best Research Cell Efficiencies Chart. National Renewable Energy Laboratory (NREL). *Golden, CO*, **2014**.
  71. H.-S. Kim, C.-R. Lee, J.-H. Im, K.-B. Lee, T. Moehl, A. Marchioro, S.-J. Moon, R. Humphry-Baker, J.-H. Yum, J. E. Moser, M. Grätzel, and N.-G. Park, Lead Iodide Perovskite Sensitized All-Solid-State Submicron Thin Film Mesoscopic Solar Cell with Efficiency Exceeding 9%. *Scientific Reports*, **2012**. *2*: p. 591.
  72. M. M Lee., J. Teuscher, T. Miyasaka, T. N. Murakami, and H. J. Snaith, Efficient Hybrid Solar Cells Based on Meso-Superstructured Organometal Halide Perovskites. *Science*, **2012**. *338*(6107): p. 643-647.
  73. H. Zhou, Q. Chen, G. Li, S. Luo, T.-b. Song, H.-S. Duan, Z. Hong, J. You, Y. Liu, and Y. Yang, Interface Engineering of Highly Efficient Perovskite Solar Cells. *Science*, **2014**. *345*(6196): p. 542-546.
  74. J.-H. Im, I.-H. Jang, N. Pellet, M. Grätzel, and N.-G. Park, Growth of CH<sub>3</sub>NH<sub>3</sub>PbI<sub>3</sub> Cuboids with Controlled Size for High-Efficiency Perovskite Solar Cells. *Nature Nanotechnology*, **2014**. *9*(11): p. 927-932.
  75. G. Xing, N. Mathews, S. Sun, S. S. Lim, Y. M. Lam, M. Grätzel, S. Mhaisalkar, and T. C. Sum, Long-Range Balanced Electron- and Hole-Transport Lengths in Organic-Inorganic CH<sub>3</sub>NH<sub>3</sub>PbI<sub>3</sub>. *Science*, **2013**. *342*(6156): p. 344-347.
  76. J.-Y. Jeng, Y.-F. Chiang, M.-H. Lee, S.-R. Peng, T.-F. Guo, P. Chen, and T.-C. Wen, CH<sub>3</sub>NH<sub>3</sub>PbI<sub>3</sub> Perovskite/Fullerene Planar-Heterojunction Hybrid Solar Cells. *Advanced Materials*, **2013**. *25*(27): p. 3727-3732.
  77. S. Sun, T. Salim, N. Mathews, M. Duchamp, C. Boothroyd, G. Xing, T. C. Sum, and Y. M. Lam, The Origin of High Efficiency in Low-Temperature Solution-Processable Bilayer Organometal Halide Hybrid Solar Cells. *Energy & Environmental Science*, **2014**. *7*(1): p. 399-407.
  78. J. You, Z. Hong, Y. Yang, Q. Chen, M. Cai, T.-B. Song, C.-C. Chen, S. Lu, Y. Liu, H. Zhou, and Y. Yang, Low-Temperature Solution-Processed Perovskite Solar Cells with High Efficiency and Flexibility. *ACS Nano*, **2014**. *8*(2): p. 1674-1680.
  79. J. You, Y. Yang, Z. Hong, T.-B. Song, L. Meng, Y. Liu, C. Jiang, H. Zhou, W.-H. Chang, G. Li, and Y. Yang, Moisture Assisted Perovskite Film Growth for High Performance Solar Cells. *Applied Physics Letters*, **2014**. *105*(18): p. 183902.
  80. C. Bi, Q. Wang, Y. Shao, Y. Yuan, Z. Xiao, and J. Huang, Non-Wetting Surface-Driven High-Aspect-Ratio Crystalline Grain Growth for Efficient Hybrid Perovskite Solar Cells. *Nature Communications*, **2015**. *6*: p. 7747.

- 
81. J. H. Heo, H. J. Han, D. Kim, T. K. Ahn, and S. H. Im, Hysteresis-Less Inverted  $\text{CH}_3\text{NH}_3\text{PbI}_3$  Planar Perovskite Hybrid Solar Cells with 18.1% Power Conversion Efficiency. *Energy & Environmental Science*, **2015**. 8(5): p. 1602-1608.
  82. A. Dualeh, N. Tétreault, T. Moehl, P. Gao, M. K. Nazeeruddin, and M. Grätzel, Effect of Annealing Temperature on Film Morphology of Organic-Inorganic Hybrid Perovskite Solid-State Solar Cells. *Advanced Functional Materials*, **2014**. 24(21): p. 3250-3258.
  83. G. E. Eperon, V. M. Burlakov, P. Docampo, A. Goriely, and H. J. Snaith, Morphological Control for High Performance, Solution-Processed Planar Heterojunction Perovskite Solar Cells. *Advanced Functional Materials*, **2014**. 24(1): p. 151-157.
  84. K. W. Tan, D. T. Moore, M. Saliba, H. Sai, L. A. Estroff, T. Hanrath, H. J. Snaith and U. Wiesner, Thermally Induced Structural Evolution and Performance of Mesoporous Block Copolymer-Directed Alumina Perovskite Solar Cells. *ACS Nano*, **2015**. 8: p. 4730-4739.
  85. H.-L. Hsu, C.-P. Chen, J.-Y. Chang, Y.-Y. Yu, and Y.-K. Shen, Two-Step Thermal Annealing Improves the Morphology of Spin-Coated Films for Highly Efficient Perovskite Hybrid Photovoltaics. *Nanoscale*, **2014**. 6(17): p. 10281-10288.
  86. F. X. Xie, D. Zhang, H. Su, X. Ren, K. S. Wong, M. Grätzel and W. C. H. Choy, Vacuum-Assisted Thermal Annealing of  $\text{CH}_3\text{NH}_3\text{PbI}_3$  for Highly Stable and Efficient Perovskite Solar Cells. *ACS Nano*, **2015**. 9: p. 639-646.
  87. T.-B. Song, Q. Chen, H. Zhou, S. Luo, Y. Yang, J. You, and Y. Yang, Unraveling Film Transformations and Device Performance of Planar Perovskite Solar Cells. *Nano Energy*, **2015**. 12: p. 494-500.
  88. S. Guarnera, A. Abate, W. Zhang, J. M. Foster, G. Richardson, A. Petrozza, and H. J. Snaith, Improving the Long-Term Stability of Perovskite Solar Cells with a Porous  $\text{Al}_2\text{O}_3$  Buffer Layer. *The Journal of Physical Chemistry Letters*, **2015**. 6(3): p. 432-437.
  89. N. J. Jeon, J. H. Noh, Y. C. Kim, W. S. Yang, S. Ryu, and S. I. Seok, Solvent Engineering for High-Performance Inorganic-Organic Hybrid Perovskite Solar Cells. *Nature Materials*, **2014**. 13(9): p. 897-903.
  90. H. B. Kim, H. Choi, J. Jeong, S. Kim, B. Walker, S. Song, and J. Y. Kim, Mixed Solvents for the Optimization of Morphology in Solution-Processed, Inverted-Type Perovskite/Fullerene Hybrid Solar Cells. *Nanoscale*, **2014**. 6(12): p. 6679-6683.
  91. J. Burschka, N. Pellet, S. J. Moon, R. Humphry-Baker, P. Gao, M. K. Nazeeruddin, and M. Grätzel, Sequential Deposition as a Route to High-Performance Perovskite-Sensitized Solar Cells. *Nature*, **2013**. 499(7458): p. 316-319.

- 
92. M. Saliba, K. W. Tan, H. Sai, D. T. Moore, T. Scott, W. Zhang, L. A. Estroff, U. Wiesner, and H. J. Snaith, Influence of Thermal Processing Protocol upon the Crystallization and Photovoltaic Performance of Organic–Inorganic Lead Trihalide Perovskites. *The Journal Of Physical Chemistry C*, **2014**. *118*(30): p. 17171-17177.
  93. G. De Luca, E. Treossi, A. Liscio, J. M. Mativetsky, L. M. Scolaro, V. Palermo, and P. Samori, Solvent Vapour Annealing of Organic Thin Films: Controlling the Self-Assembly of Functional Systems Across Multiple Length Scales. *Journal of Materials Chemistry*, **2010**. *20*(13): p. 2493-2498.
  94. S. R. Raga, M.-C. Jung, M. V. Lee, M. R. Leyden, Y. Kato, and Y. Qi, The Influence of Air Annealing on High Efficiency Planar Structure Perovskite Solar Cells. *Chemistry of Materials*, **2015**. *27*: p. 1597-1603.
  95. S. Pathak, A. Sepe, A. Sadhanala, F. Deschler, A. Haghighirad, N. Sakai, K. C. Goedel, S. D. Stranks, N. Noel, M. Price, S. Hüttner, N. A. Hawkins, R. H. Friend, U. Steiner and H. J. Snaith, Atmospheric Influence upon Crystallization and Electronic Disorder and its Impact on the Photophysical Properties of Organic-Inorganic Perovskite Solar Cells. *ACS Nano*, **2015**. *9*: p. 2311-2320.
  96. E. Mosconi, J. M. Azpiroz, and F. De Angelis, Ab Initio Molecular Dynamics Simulations of Methylammonium Lead Iodide Perovskite Degradation by Water. *Chemistry of Materials*, **2015**. *27*: p. 4885-4892.
  97. H. Zhou, Q. Chen, G. Li, S. Luo, T. B. Song, H. S. Duan, Z. Hong, J. You, Y. Liu, and Y. Yang, Photovoltaics. Interface Engineering of Highly Efficient Perovskite Solar Cells. *Science*, **2014**. *345*(6196): p. 542-546.
  98. X. Song, W. Wang, P. Sun, W. Ma, and Z.-K. Chen, Additive to Regulate the Perovskite Crystal Film Growth in Planar Heterojunction Solar Cells. *Applied Physics Letters*, **2015**. *106*(3): p. 033901.
  99. P. W. Liang., C. Y. Liao, C. C. Chueh, F. Zuo, S. T. Williams, X. K. Xin, J. Lin, and A. K. Jen, Additive Enhanced Crystallization of Solution-Processed Perovskite for Highly Efficient Planar-Heterojunction Solar Cells. *Advanced Materials*, **2014**. *26*(22): p. 3748-3754.
  100. H. Yu, F. Wang, F. Xie, W. Li, J. Chen, and N. Zhao, The Role of Chlorine in the Formation Process of “CH<sub>3</sub>NH<sub>3</sub>PbI<sub>3-x</sub>Cl<sub>x</sub>” Perovskite. *Advanced Functional Materials*, **2014**. *24*: p. 7102-7108.
  101. E. L. Unger, A. R. Bowring, C. J. Tassone, V. L. Pool, A. Gold-Parker, R. Cheacharoen, K. H. Stone, E. T. Hoke, M. F. Toney, and M. D. McGehee, Chloride in Lead Chloride-Derived Organo-Metal Halides for Perovskite-Absorber Solar Cells. *Chemistry of Materials*, **2014**. *26*(24): p. 7158-7165.



- 
102. D. T. Moore, H. Sai, K. W. Tan, D. M. Smilgies, W. Zhang, H. J. Snaith, U. Wiesner, and L. A. Estroff, Crystallization Kinetics of Organic-Inorganic Trihalide Perovskites and the Role of the Lead Anion in Crystal Growth. *Journal of the American Chemical Society*, **2015**. 137(6): p. 2350-2358.
  103. J. Yang, B. D. Siempelkamp, D. Liu, and T. L. Kelly, Investigation of CH<sub>3</sub>NH<sub>3</sub>PbI<sub>3</sub> Degradation Rates and Mechanisms in Controlled Humidity Environments Using in Situ Techniques. *ACS Nano*, **2015**. 9(2): p. 1955-1963.
  104. J. A. Christians, P. A. Miranda Herrera, and P. V. Kamat, Transformation of the Excited State and Photovoltaic Efficiency of CH<sub>3</sub>NH<sub>3</sub>PbI<sub>3</sub> Perovskite upon Controlled Exposure to Humidified Air. *Journal of the American Chemical Society*, **2015**. 137(4): p. 1530-1538.
  105. G. Niu, W. Li, F. Meng, L. Wang, H. Dong, and Y. Qiu, Study on the Stability of CH<sub>3</sub>NH<sub>3</sub>PbI<sub>3</sub> Films and the Effect of Post-Modification by Aluminum Oxide in All-Solid-State Hybrid Solar Cells. *Journal of Materials Chemistry A*, **2014**. 2(3): p. 705-710.
  106. Y. Han, S. Meyer, Y. Dkhissi, K. Weber, J. M. Pringle, U. Bach, L. Spiccia, and Y.-B. Cheng, Degradation Observations of Encapsulated Planar CH<sub>3</sub>NH<sub>3</sub>PbI<sub>3</sub> Perovskite Solar Cells at High Temperatures and Humidity. *Journal of Materials Chemistry A*, **2015**. 3(15): p. 8139-8147.
  107. B. Hailegnaw, S. Kirmayer, E. Edri, G. Hodes, and D. Cahen, Rain on Methylammonium Lead Iodide Based Perovskites: Possible Environmental Effects of Perovskite Solar Cells. *The Journal of Physical Chemistry Letters*, **2015**. 6(9): p. 1543-1547.
  108. J. M. Frost, K. T. Butler, F. Brivio, C. H. Hendon, M. van Schilfgaarde, and A. Walsh, Atomistic Origins of High-Performance in Hybrid Halide Perovskite Solar Cells. *Nano Letters*, **2014**. 14(5): p. 2584-2590.
  109. Y. Li, X. Xu, C. Wang, C. Wang, F. Xie, J. Yang, and Y. Gao, Degradation by Exposure of Coevaporated CH<sub>3</sub>NH<sub>3</sub>PbI<sub>3</sub> Thin Films. *The Journal Of Physical Chemistry C*, **2015**. 119(42): p. 23996-24002.
  110. B. R. Vincent, K. N. Robertson, T. S. Cameron, O. Knop, Alkylammonium lead halides. Part 1. Isolated PbI<sub>6</sub><sup>4-</sup> ions in (CH<sub>3</sub>NH<sub>3</sub>)<sub>4</sub>PbI<sub>6</sub>·2H<sub>2</sub>O. *Canadian Journal of Chemistry*, **1987**. 65(5): p. 1042-1046.
  111. A. M. A. Leguy, Y. Hu, M. Campoy-Quiles, M. I. Alonso, O. J. Weber, P. Azarhoosh, M. van Schilfgaarde, M. T. Weller, T. Bein, J. Nelson, P. Docampo, and P. R. F. Barnes, Reversible Hydration of CH<sub>3</sub>NH<sub>3</sub>PbI<sub>3</sub> in Films, Single Crystals, and Solar Cells. *Chemistry of Materials*, **2015**. 27(9): p. 3397-3407.



- 
112. H.-S. Kim and N.-G. Park, Parameters Affecting I–V Hysteresis of CH<sub>3</sub>NH<sub>3</sub>PbI<sub>3</sub> Perovskite Solar Cells: Effects of Perovskite Crystal Size and Mesoporous TiO<sub>2</sub> Layer. *The Journal of Physical Chemistry Letters*, **2014**. 5(17): p. 2927-2934.
  113. P. Pistor, J. Borchert, W. Fränzel, R. Csuk, and R. Scheer, Monitoring the Phase Formation of Coevaporated Lead Halide Perovskite Thin Films by in Situ X-ray Diffraction. *The Journal of Physical Chemistry Letters*, **2014**. 5(19): p. 3308-3312.
  114. F. Huang, Y. Dkhissi, W. Huang, M. Xiao, I. Benesperi, S. Rubanov, Y. Zhu, X. Lin, L. Jiang, Y. Zhou, A. Gray-Weale, J. Etheridge, C. R. McNeill, R. A. Caruso, U. Bach, L. Spiccia, and Y.-B. Cheng, Gas-Assisted Preparation of Lead Iodide Perovskite Films Consisting of a Monolayer of Single Crystalline Grains for High Efficiency Planar Solar Cells. *Nano Energy*, **2014**. 10(0): p. 10-18.
  115. W. Nie, H. Tsai, R. Asadpour, J.-C. Blancon, A. J. Neukirch, G. Gupta, J. J. Crochet, M. Chhowalla, S. Tretiak, M. A. Alam, H.-L. Wang, and A. D. Mohite, High-Efficiency Solution-Processed Perovskite Solar Cells with Millimeter-Scale Grains. *Science*, **2015**. 347(6221): p. 522-525.
  116. Z. Zhou, Z. Wang, Y. Zhou, S. Pang, D. Wang, H. Xu, Z. Liu, N. P. Padture, and G. Cui, Methylamine-Gas-Induced Defect-Healing Behavior of CH<sub>3</sub>NH<sub>3</sub>PbI<sub>3</sub> Thin Films for Perovskite Solar Cells. *Angewandte Chemie International Edition*, **2015**. 127(33): p. 9841-9845.
  117. S.-H. Jin, B. Vijaya Kumar Naidu, H.-S. Jeon, S.-M. Park, J.-S. Park, S. Chul Kim, J. Wook Lee, and Y.-S. Gal, Optimization of Process Parameters for High-Efficiency Polymer Photovoltaic Devices Based on P3HT:PCBM System. *Solar Energy Materials and Solar Cells*, **2007**. 91(13): p. 1187-1193.
  118. Y. Bai, H. Yu, Z. Zhu, K. Jiang, T. Zhang, N. Zhao, S. Yang, and H. Yan, High Performance Inverted Structure Perovskite Solar Cells Based on a PCBM:Polystyrene Blend Electron Transport Layer. *Journal of Materials Chemistry A*, **2015**. 3(17): p. 9098-9102.
  119. L. Dou, Y. Yang, J. You, Z. Hong, W.-H. Chang, G. Li, and Y. Yang, Solution-Processed Hybrid Perovskite Photodetectors with High Detectivity. *Nature Communications*, **2014**. 5: p. 5404.
  120. E. Sengupta, Studies of Degradation of Organic Solar Cell Materials using Electrical Scanning Probe Microscopy *PhD Dissertation*, **2012**.
  121. G. Binnig, C. F. Quate, and C. Gerber, Atomic Force Microscope. *Physical Review Letters*, **1986**. 56(9): p. 930-933.
  122. R. García and R. Pérez, Dynamic Atomic Force Microscopy Methods. *Surface Science Reports*, **2002**. 47(6–8): p. 197-301.
  123. P. E. P. West, *Atomic Force Microscopy*. May 2010: Oxford Scholarship Online.

- 
124. D. Wang, Z. Liu, Z. Zhou, H. Zhu, Y. Zhou, C. Huang, Z. Wang, H. Xu, Y. Jin, B. Fan, S. Pang, and G. Cui, Reproducible One-Step Fabrication of Compact  $\text{MAPb}_{1-x}\text{Cl}_x$  Thin Films Derived from Mixed-Lead-Halide Precursors. *Chemistry of Materials*, **2014**. 26(24): p. 7145-7150.
  125. S. Wang, L. K. Ono, M. R. Leyden, Y. Kato, S. R. Raga, M. V. Lee, and Y. Qi, Smooth Perovskite Thin Films and Efficient Perovskite Solar Cells Prepared by the Hybrid Deposition Method. *Journal of Materials Chemistry A*, **2015**. 3(28): p. 14631-14641.
  126. W. Zhang, M. Saliba, D. T. Moore, S. K. Pathak, M. T. Hörlantner, T. Stergiopoulos, S. D. Stranks, G. E. Eperon, J. A. Alexander-Webber, A. Abate, A. Sadhanala, S. Yao, Y. Chen, R. H. Friend, L. A. Estroff, U. Wiesner, and H. J. Snaith, Ultrasooth Organic-Inorganic Perovskite Thin-Film Formation and Crystallization for Efficient Planar Heterojunction Solar Cells. *Nature Communications*, **2015**. 6: p. 6142.
  127. C.-J. Tong, W. Geng, Z.-K. Tang, C.-Y. Yam, X.-L. Fan, J. Liu, W.-M. Lau, and L.-M. Liu, Uncovering the Veil of the Degradation in Perovskite  $\text{CH}_3\text{NH}_3\text{PbI}_3$  upon Humidity Exposure: A First-Principles Study. *The Journal of Physical Chemistry Letters*, **2015**. 6(16): p. 3289-3295.
  128. R. K. Misra, S. Aharon, B. Li, D. Mogilyansky, I. Visoly-Fisher, L. Etgar, and E. A. Katz, Temperature- and Component-Dependent Degradation of Perovskite Photovoltaic Materials under Concentrated Sunlight. *The Journal of Physical Chemistry Letters*, **2015**. 6: p. 326-330.
  129. D. Attwood, Soft X-rays and Extreme Ultraviolet Radiation. *Cambridge University*, **1999**. ISBN 978-0-521-65214-8: p. 2.
  130. B. B. P. He, Uwe; Smith Kingsley L., Comparison Between Conventional and Two-Dimensional XRD. *International Centre for Diffraction Data*, **2003**. 46: p. 38-42.
  131. F. Zhu, L. Men, Y. Guo, Q. Zhu, U. Bhattacharjee, P. M. Goodwin, J. W. Petrich, E. A. Smith, and J. Vela, Shape Evolution and Single Particle Luminescence of Organometal Halide Perovskite Nanocrystals. *ACS Nano*, **2015**. 9(3): p. 2948-2959.
  132. X. Lou, R. W. Sinkeldam, W. van Houts, Y. Nicolas, P. G. A. Janssen, J. L. J. van Dongen, J. A. J. M. Vekemans, and E. W. Meijer, Double Cation Adduction in Matrix-Assisted Laser Desorption/Ionization Time-of-Flight Mass Spectrometry of Electron Deficient Anthraquinone Derivatives. *Journal of Mass Spectrometry*, **2007**. 42(3): p. 293-303.
  133. S. G. Kotsiris, Y. V. Vasil'ev, A. V. Streletskii, M. Han, L. P. Mark, O. V. Boltalina, N. Chronakis, M. Orfanopoulos, H. Hungerbühler, and T. Drewello, Application

- 
- and Evaluation of Solvent-Free Matrix-Assisted Laser Desorption/Ionization Mass Spectrometry for the Analysis of Derivatized Fullerenes. *European Journal of Mass Spectrometry (Chichester, Eng)*, **2006**. 12(6): p. 397-408.
134. T. Brown, N. L. Clipston, N. Simjee, H. Luftmann, H. Hungerbühler, and T. Drewello, Matrix-Assisted Laser Desorption/Ionization of Amphiphilic Fullerene Derivatives. *International Journal of Mass Spectrometry*, **2001**. 210–211: p. 249-263.
135. F. Matteocci, Y. Busby, J. J. Pireaux, G. Divitini, S. Cacovich, C. Ducati, and A. Di Carlo, Interface and Composition Analysis on Perovskite Solar Cells. *ACS Applied Materials & Interfaces*, **2015**. 7(47): p. 26176-26183.
136. [https://en.wikipedia.org/wiki/Spin\\_coating](https://en.wikipedia.org/wiki/Spin_coating).
137. L. E. Scriven. Physics and Applications of DIP Coating and Spin Coating. *MRS Proceedings*, **1998**. 121, 717. Doi:10.1557/PROC-121-717.
138. Z. Xiao, C. Bi, Y. Shao, Q. Dong, Q. Wang, Y. Yuan, C. Wang, Y. Gao, and J. Huang, Efficient, High Yield Perovskite Photovoltaic Devices Grown by Interdiffusion of Solution-Processed Precursor Stacking Layers. *Energy & Environmental Science*, **2014**. 7(8): p. 2619-2623.
139. M. Liu, M. B. Johnston, and H. J. Snaith, Efficient Planar Heterojunction Perovskite Solar Cells by Vapour Deposition. *Nature*, **2013**. 501(7467): p. 395-398.
140. Y. Zhou, M. Yang, W. Wu, A. L. Vasiliev, K. Zhu, and N. P. Padture, Room-Temperature Crystallization of Hybrid-Perovskite Thin Films via Solvent–Solvent Extraction for High-Performance Solar Cells. *Journal of Materials Chemistry A*, **2015**. 3: p. 8178-8184.
141. C. Gao, J. Liu, C. Liao, Q. Ye, Y. Zhang, X. He, X. Guo, J. Mei, and W. Lau, Formation of Organic-Inorganic Mixed Halide Perovskite Films by Thermal Evaporation of  $\text{PbCl}_2$  and  $\text{CH}_3\text{NH}_3\text{I}$  Compounds. *RSC Advances*, **2015**. 5(33): p. 26175-26180.
142. B.-w. Park, B. Philippe, T. Gustafsson, K. Sveinbjörnsson, A. Hagfeldt, E. M. J. Johansson, and G. Boschloo, Enhanced Crystallinity in Organic–Inorganic Lead Halide Perovskites on Mesoporous  $\text{TiO}_2$  via Disorder–Order Phase Transition. *Chemistry of Materials*, **2014**. 26(15): p. 4466-4471.
143. A. Ng, Z. Ren, Q. Shen, S. H. Cheung, H. C. Gokkaya, G. Bai, J. Wang, L. Yang, S. K. So, A. B. Djurisić, W. W.-f. Leung, J. Hao, W. K. Chan, and C. Surya, Efficiency Enhancement by Defect Engineering in Perovskite Photovoltaic Cells Prepared Using Evaporated  $\text{PbI}_2/\text{CH}_3\text{NH}_3\text{I}$  Multilayers. *Journal of Materials Chemistry A*, **2015**. 3(17): p. 9223-9231.

- 
144. B. Wang, K. Young Wong, X. Xiao, and T. Chen, Elucidating the Reaction Pathways in the Synthesis of Organolead Trihalide Perovskite for High-Performance Solar Cells. *Scientific Reports*, **2015**. 5: p. 10557.
  145. A. Dualeh, P. Gao, S. I. Seok, M. K. Nazeeruddin, and M. Grätzel, Thermal Behavior of Methylammonium Lead-Trihalide Perovskite Photovoltaic Light Harvesters. *Chemistry of Materials*, **2014**. 26(21): p. 6160-6164.
  146. I. Persson, K. Lyczko, D. Lundberg, L. Eriksson, and A. Placzek, Coordination Chemistry Study of Hydrated and Solvated Lead(II) Ions in Solution and Solid State. *Inorganic Chemistry*, **2011**. 50(3): p. 1058-1072.
  147. F. Hao, C. C. Stoumpos, Z. Liu, R. P. H. Chang, and M. G. Kanatzidis, Controllable Perovskite Crystallization at a Gas–Solid Interface for Hole Conductor-Free Solar Cells with Steady Power Conversion Efficiency over 10%. *Journal of the American Chemical Society*, **2014**. 136(46): p. 16411-16419.
  148. W. Kong, Z. Ye, Z. Qi, B. Zhang, M. Wang, A. Rahimi-Iman, and H. Wu, Characterization of an Abnormal Photoluminescence Behavior upon Crystal-Phase Transition of Perovskite  $\text{CH}_3\text{NH}_3\text{PbI}_3$ . *Physical Chemistry Chemical Physics*, **2015**. 17(25): p. 16405-16411.
  149. T. Supasai, N. Rujisamphan, K. Ullrich, A. Chemseddine, and T. Dittrich, Formation of a Passivating  $\text{CH}_3\text{NH}_3\text{PbI}_3/\text{PbI}_2$  Interface during Moderate Heating of  $\text{CH}_3\text{NH}_3\text{PbI}_3$  Layers. *Applied Physics Letters*, **2013**. 103(18): p. 183906.
  150. S. Miller, G. Fanchini, Y.-Y. Lin, C. Li, C.-W. Chen, W.-F. Su, and M. Chhowalla, Investigation of Nanoscale Morphological Changes in Organic Photovoltaics during Solvent Vapor Annealing. *Journal of Materials Chemistry*, **2008**. 18(3): p. 306-312.
  151. K. C. Dickey, J. E. Anthony, and Y. L. Loo, Improving Organic Thin-Film Transistor Performance through Solvent-Vapor Annealing of Solution-Processable Triethylsilylethynyl Anthradithiophene. *Advanced Materials*, **2006**. 18(13): p. 1721-1726.
  152. J. C. Conboy, E. J. C. Olson, D. M. Adams, J. Kerimo, A. Zaban, B. A. Gregg, and P. F. Barbara, Impact of Solvent Vapor Annealing on the Morphology and Photophysics of Molecular Semiconductor Thin Films. *The Journal of Physical Chemistry B*, **1998**. 102(23): p. 4516-4525.
  153. T. A. Bull, L. S. C. Pingree, S. A. Jenekhe, D. S. Ginger, and C. K. Luscombe, The Role of Mesoscopic PCBM Crystallites in Solvent Vapor Annealed Copolymer Solar Cells. *ACS Nano*, **2009**. 3(3): p. 627-636.
  154. Z. Xiao, Q. Dong, C. Bi, Y. Shao, Y. Yuan, and J. Huang, Solvent Annealing of Perovskite-Induced Crystal Growth for Photovoltaic-Device Efficiency Enhancement. *Advanced Materials*, **2014**. 26(37): p. 6503-6509.

- 
155. Q. Chen, H. Zhou, Z. Hong, S. Luo, H. S. Duan, H. H. Wang, Y. Liu, G. Li, and Y. Yang, Planar Heterojunction Perovskite Solar Cells via Vapor-Assisted Solution Process. *Journal of the American Chemical Society*, **2014**. 136(2): p. 622-625.
  156. F. Matsumoto, S. M. Vorpahl, J. Q. Banks, E. Sengupta, and D. S. Ginger, Photodecomposition and Morphology Evolution of Organometal Halide Perovskite Solar Cells. *The Journal Of Physical Chemistry C*, **2015**. 119(36): p. 20810-20816.
  157. X. Xu, C. Random, P. Efstathiou, and J. T. Irvine, A Red Metallic Oxide Photocatalyst. *Nature Materials*, **2012**. 11(7): p. 595-598.
  158. D.-X. Yuan, A. Gorka, M.-F. Xu, Z.-K. Wang, and L.-S. Liao, Inverted Planar NH<sub>2</sub>CH[Double Bond, Length as m-Dash]NH<sub>2</sub>PbI<sub>3</sub> Perovskite Solar Cells with 13.56% Efficiency via Low Temperature Processing. *Physical Chemistry Chemical Physics*, **2015**. 17(30): p. 19745-19750.
  159. Z. Ren, A. Ng, Q. Shen, H. C. Gokkaya, J. Wang, L. Yang, W.-K. Yiu, G. Bai, A. B. Djurišić, W. W.-f. Leung, J. Hao, W. K. Chan, and C. Surya, Thermal Assisted Oxygen Annealing for High Efficiency Planar CH<sub>3</sub>NH<sub>3</sub>PbI<sub>3</sub> Perovskite Solar Cells. *Scientific Reports*, **2014**. 4. 6752.
  160. Y. Zhao and K. Zhu, Charge Transport and Recombination in Perovskite (CH<sub>3</sub>NH<sub>3</sub>)PbI<sub>3</sub> Sensitized TiO<sub>2</sub> Solar Cells. *The Journal of Physical Chemistry Letters*, **2013**. 4(17): p. 2880-2884.
  161. Y. H. Lee, J. Luo, R. Humphry-Baker, P. Gao, M. Grätzel, and M. K. Nazeeruddin, Unraveling the Reasons for Efficiency Loss in Perovskite Solar Cells. *Advanced Functional Materials*, **2015**. 25: p. 3925-3933.
  162. Y. Shimokawa, T. Kajiyama, K. Sakai, and M. Doi, Measurement of the Skin Layer in the Drying Process of a Polymer Solution. *Physical Review E*, **2011**. 84(5): p. 051803.
  163. C. H. Seager, Grain Boundaries in Polycrystalline Silicon. *Annual Review of Materials Science*, **1985**. 15: p. 271-302.
  164. H. C. Card and E. S. Yang, Electronic Processes at Grain Boundaries in Polycrystalline Semiconductors under Optical Illumination. *IEEE Transactions on Electron Devices*, **1977**. ED-24, p: 397-402.
  165. D. W. de Quilettes, S. M. Vorpahl, S. D. Stranks, H. Nagaoka, G. E. Eperon, M. E. Ziffer, H. J. Snaith, and D. S. Ginger, Impact of Microstructure on Local Carrier Lifetime in Perovskite Solar Cells. *Science*, **2015**. 348(6235): p. 683-686.
  166. Y. Matsuo, A. Ozu, N. Obata, N. Fukuda, H. Tanaka, and E. Nakamura, Deterioration of Bulk Heterojunction Organic Photovoltaic Devices by a Minute Amount of Oxidized Fullerene. *Chemical Communications*, **2012**. 48(32): p. 3878-3880.

- 
167. I. E. Brumboiu, L. Ericsson, R. Hansson, E. Moons, O. Eriksson, and B. Brena, The influence of Oxygen Adsorption on the NEXAFS and Core-Level XPS Spectra of the C<sub>60</sub> Derivative PCBM. *The Journal of Chemical Physics*, **2015**. 142(5): p. 054306.
  168. K. M. Creegan, J. L. Robbins, W. K. Robbins, J. M. Millar, R. D. Sherwood, P. J. Tindall, D. M. Cox, J. P. McCauley, and D. R. Jones, Synthesis and Characterization of C<sub>60</sub>O, the First Fullerene Epoxide. *Journal of the American Chemical Society*, **1992**. 114(3): p. 1103-1105.
  169. N. Curry, B. Doust, and D. Jelski, A Computational Study of the Combinatorial Addition of Oxygen to Buckminsterfullerene. *Journal of Cluster Science*, **2001**. 12(2): p. 385-390.
  170. J. C. Hummelen, J. Knol, and L. Sánchez. *Stability Issues of Conjugated Polymer/Fullerene Solar Cells from a Chemical Viewpoint*. EPRINTS-BOOK-TITLE. University of Groningen, Stratingh Institute for Chemistry, **2001**.
  171. Zhou, L., H. Deng, Q. Deng, L. Zheng, and Y. Cao, Analysis of Three Different Types of Fullerene Derivatives by Laser Desorption/Ionization Time-of-Flight Mass Spectrometry with New Matrices. *Rapid Communications in Mass Spectrometry*, **2005**. 19(23): p. 3523-3530.
  172. T. Heumueller, W. R. Mateker, A. Distler, U. F. Fritze, R. Cheacharoen, W. H. Nguyen, M. Biele, M. Salvador, M. von Delius, H.-J. Egelhaaf, M. D. McGehee, and C. J. Brabec, Morphological and Electrical Control of Fullerene Dimerization Determines Organic Photovoltaic Stability. *Energy & Environmental Science*, **2016**. 9(1): p. 247-256.
  173. P. C. Ekund, A. M. Rao, P. Zhou, Y. Wang, J. M. Holden, *Photochemical transformation of C<sub>60</sub> and C<sub>70</sub> films*, *Thin Solid Films*, **1995**, 257: p. 185-203.

---

# Acknowledgement

During the three-year of PhD study, I met numerous people who enriched my experience of learning and working at MPIP. I would like to take this opportunity to express my acknowledgements to these people for their contributions:

First of all, I would like to thank [REDACTED] who gave me the unique opportunity to work in his research group. I really appreciate his continuous and kindly encouragement and support during my study. I'm really grateful to him for all the fruitful and inspiring discussions in my research topics. What I have learnt from him are not only his strict attitude and enthusiasm in scientific career but also his patience to persons.

One of the most important persons during my three-year PhD study at MPIP was my project leader [REDACTED]. He was also my project supervisor. I would like to thank him who provided me an excellent environment to develop my scientific skills and guided me to think about my projects in wide perspective. We had lots of fruitful discussions and I got many constructive suggestions from him. I really have learnt a lot from Rüdiger not only about scientific projects but also the way of thinking. He always could explain/arrange things in an easily understandable way, which is very important and necessary in writing papers, preparing posters and presentations. His patient and valuable guidance and constant support inspired me a lot. I also received many valuable advices on choosing a future job, raising children. As an old Chinese saying said "the best teacher is not only a wise mentor but also a nice friend", Rüdiger is exactly this kind of mentor that I have the luck the work with for more than three years.

I would like to express my thanks to **China Scholarship Council (CSC)** for the scholarship and the opportunity to study in Germany.

I would like to thank all of the working partners for the research collaborations: [REDACTED] [REDACTED] for showing me how to make perovskite solutions/films and the following useful discussions; [REDACTED] [REDACTED] who gave me lots of useful suggestions and discussion for my perovskite solar cell project; [REDACTED] and [REDACTED] for in-situ X-ray diffraction experiments and the following discussions; [REDACTED] for the corrections and suggestion on my perovskite publication; [REDACTED] and [REDACTED] for providing me solar simulator allowing me do photo-degradations. [REDACTED] showed me the procedures to do photo-degradation of PCBM thin



---

films and the nice discussions on PCBM degradation project; [REDACTED] for the discussions on the PCBM photo-degradation; [REDACTED] for the help and discussions on MALDI-TOF MS experiments; [REDACTED] for the corrections and suggestions on the experimental method part of MALDI-TOF MS; [REDACTED] for the suggestions on PCBM film preparation and results discussions. [REDACTED] and [REDACTED] for the help with my German abstract in the thesis.

I also would like to express my special thanks to [REDACTED] who made a SFM introduction to me at the beginning of my PhD study and offered endless help whenever I met problems during SFM measurements; [REDACTED] for the Scanning Electron Microscopy (SEM); Helma Burg for providing supports in SFM labs; [REDACTED] for the ex-situ X-ray diffraction measurements; [REDACTED] for providing technical support on glovebox and spin-coater.

Also special thanks to all my current and former fantastic office mates, [REDACTED] [REDACTED] [REDACTED] and the other friends in **AK Butt**. I really enjoyed a lot with them especially at the beginning of my PhD study, they helped me a lot on oral English and how to deal with the PhD studies.

I would like to thank my parent [REDACTED] and [REDACTED]. They gave me a lot of freedom and endless supports in my life. They never forced me to do anything but always behave as listeners and gave me nice suggestion. I also would like to thank [REDACTED] and [REDACTED] who always positively encouraged me during my studies and in my life.

Finally, I want to thank my husband [REDACTED] who gave me lots of help and support in my study and private life. Also a special thanks to my daughter [REDACTED], she came to me as a surprise and brings a lot of happiness to my life.



---

# Curriculum Vitae

[REDACTED]

Date of Birth: February 19<sup>th</sup>, 1986

Place of Birth: Henan, China

Nationality: Chinese

## Dissertation

10/2012 – 02/2016

PhD thesis “Crystallization and degradation studies in organic & perovskite solar materials” at Max Planck Institute for Polymer Research in the group of [REDACTED] with project leader [REDACTED]

## Study

09/2009 - 07/2012

Study at Renmin University of China (RUC), Beijing, China. Degree obtained: “M. Sc. Chemistry”

Master Thesis under the supervision of [REDACTED], Chemistry department

Title: “Structure and charge transport dynamics of polymer photovoltaic devices”.

09/2005 – 07/2009

Study at Zhengzhou University (ZZU), Zhengzhou, China. Degree obtained: “B. Sc. Chemistry”

Bachelor thesis under the supervision of [REDACTED], Chemistry department

---

## List of Publications:

- **Dan Li**, Simon A. Bretschneider, Victor W. Bergmann, Ilka M. Hermes, Julian Mars, Alexander Klasen, Hao Lu, Wolfgang Tremel, Markus Mezger, Hans-Jürgen Butt, Stefan A. L. Weber, Rüdiger Berger, *Humidity-induced grain boundaries in MAPbI<sub>3</sub> perovskite films*, J. Phys. Chem. C, **2016**, *120*, 6363-6368.
- Ilka M. Hermes, Simon A. Bretschneider, Victor W. Bergmann, **Dan Li**, Alexander Klasen, Julian Mars, Wolfgang Tremel, Frédéric Laquai, Hans-Jürgen Butt, Markus Mezger, Rüdiger Berger, Brian J. Rodriguez, Stefan A. L. Weber, *Ferroic domains in μm-sized methylammonium lead halide grains*, J. Phys. Chem. C, **2016**, *120*, 5724-5731.
- Victor W. Bergmann, Yunlong Guo, Hideyuki Tanaka, Ilka M. Hermes, **Dan Li**, Simon A. Bretschneider, Eiichi Nakamura, Rüdiger Berger, Stefan A. L. Weber, *Local time-dependent charging in a perovskite solar cell*, **2016**, submitted.
- Victor W. Bergmann, Stefan A. L. Weber, F. Javier Ramos, Mohammad Khaja Nazeeruddin, Michael Grätzel, **Dan Li**, Anna L. Domanski, Ingo Lieberwirth, Shahzada Ahmad, Rüdiger Berger, *Real-space observation of unbalanced charge distribution inside a perovskite-sensitized solar cell*, Nat. Comm., **2014**, doi: 10.1038/ncomms6001.
- Cunbin An, Mengmeng Li, Tomasz Marszalek, **Dan Li**, Rüdiger Berger, Wojciech Pisula, Martin Baumgarten, *Thiadizoloquinoxaline-based low-bandgap conjugated polymers as ambipolar semiconductor for organic field effect transistors*, Chem. Mater., **2014**, *26*, 5923-5929.
- Antigoni Theodoratou, Ulrich Jonas, Benoit Loppinet, Thomas Geue, René Stangenberg, **Dan Li**, Rüdiger Berger, Dimitris Vlassopoulos, *Photoswitching the mechanical properties in Langmuir layers of semifluorinated alkyl-azobenzenes at the air-water interface*, Phy. Chem. Chem. Phys., **2015**, *17*, 28844-22852.
- Antigoni Theodoratou, Ulrich Jonas, Benoit Loppinet, Thomas Geue, René Stangenberg, Rabea Keller, **Dan Li**, Rüdiger Berger, Jan Vermant, Dimitris Vlassopoulos, *Semifluorinated alkanes at the air-water interface: tailoring structure and rheology at the molecular scale*, Langmuir, **2016**, *32*, 3139-3151.

## Poster Presentations and Courses attended:

- European Materials Research Society (E-MRS) spring meeting 2015 in Lille, France (May, 2015)
- 15th conference of the International Association of Colloid and Interface Scientists (IACIS) 2015 in Mainz, Germany (May, 2015)

- 
- Summer school on “Charge and spin-transport in non-metallic systems and confined geometries” in Mainz, Germany (August, 2014)
  - Summer school on “Investigating the solid-liquid interface” in Mainz, Germany (September, 2015)